COPERNICUS SPACE COMPONENT SENTINEL OPTICAL IMAGING

MISSION PERFORMANCE CLUSTER SERVICE

Data Quality Report

Sentinel-3 OLCI

December 2022

Ref.: OMPC.ACR.DQR.03.12-2022
Issue: 1.0
Date: 13/01/2023
Contract: 4000136252/21/I-BG

Customer:	ESA	**Document Ref.:**	OMPC.ACR.DQR.03.12-2022
Contract No.:	4000136252/21/I-BG	**Date:**	13/01/2023
		Issue:	1.0

Project:	COPERNICUS SPACE COMPONENT SENTINEL OPTICAL IMAGING MISSION PERFORMANCE CLUSTER SERVICE		
Title:	Data Quality Report - OLCI		
Author(s):	OLCI ESL team		
Approved by:	L. Bourg, OPT-MPC OLCI ESL Coordinator S. Clerc, OPT-MPC Optical ESL Coordinator	**Authorized by**	C. Hénocq, OPT-MPC S3 Technical Manager
Distribution:	ESA, EUMETSAT, published in Sentinel Online		
Accepted by ESA	S. Dransfeld, ESA TO		
Filename	OMPC.ACR.DQR.03.12-2022 - i1r0 - OLCI DQR December 2022.docx		

Changes Log

Version	Date	Changes
1.0	13/01/2023	First version

List of Changes

Version	Section	Answers to RID	Changes

Table of content

List of Figures

List of Tables

1 Processing Baseline Version

1.1 Sentinel3-A

IPF	IPF / Processing Baseline version	Date of deployment
OL1	06.13 / OL__L1_.003.00.00 (with uncertainties activated)	23/08/2022
OL2 LAND	06.16 / OL__L2L.002.10.01	23/08/2022
SY2	06.23 / SYN_L2_.002.16.00	23/08/2022
SY2_VGS	06.11 / SYN_L2V.002.08.00	23/08/2022
SY2_AOD	01.06 / AOD_NTC.002.06.01	23/08/2022

1.2 Sentinel3-B

IPF	IPF / Processing Baseline version	Date of deployment
OL1	06.13 / OL__L1_.003.00.00 (with uncertainties activated)	31/08/2022
OL2 Land	06.16 / OL__L2L.002.10.01	05/09/2022
SY2	06.23 / SYN_L2_.002.16.00	09/09/2022
SY2_VGS	06.11 / SYN_L2V.002.08.00	09/09/2022
SY2_AOD	01.06 / AOD_NTC.002.06.01	09/09/2022

2 Instrument monitoring

2.1 CCD temperatures

2.1.1 OLCI-A

The long-term monitoring of the CCD temperatures is based on Radiometric Calibration Annotations (see Figure 1). Variations are very small (0.09 C peak-to-peak) and no trend can be identified. Data from current reporting period (rightmost data points) do not show any specificity.

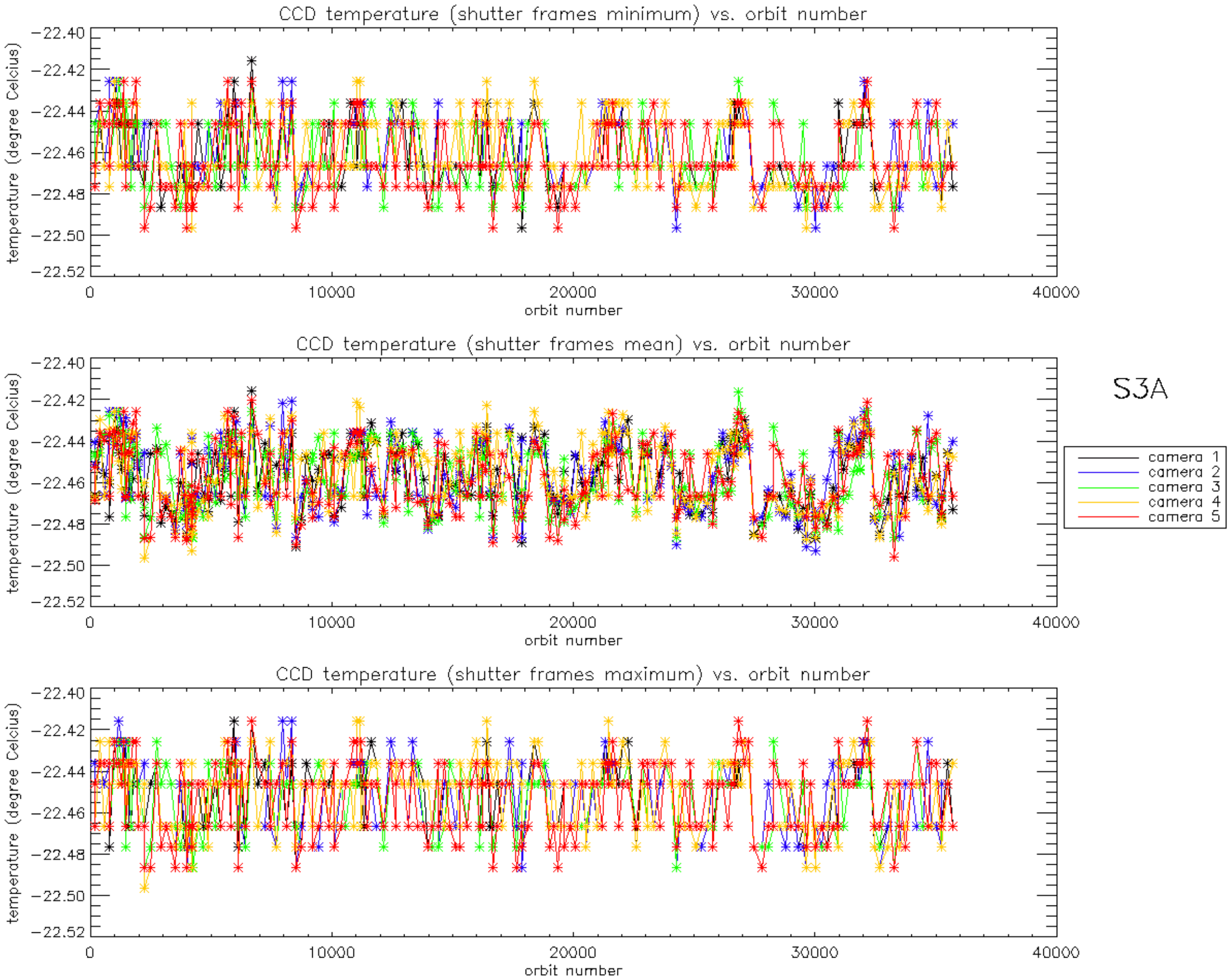

Figure 1: long term monitoring of OLCI-A CCD temperatures using minimum value (top), time averaged values (middle), and maximum value (bottom) provided in the annotations of the Radiometric Calibration Level 1 products, for the shutter frames, all radiometric calibrations so far except the first one (absolute orbit 183) for which the instrument was not yet thermally stable.

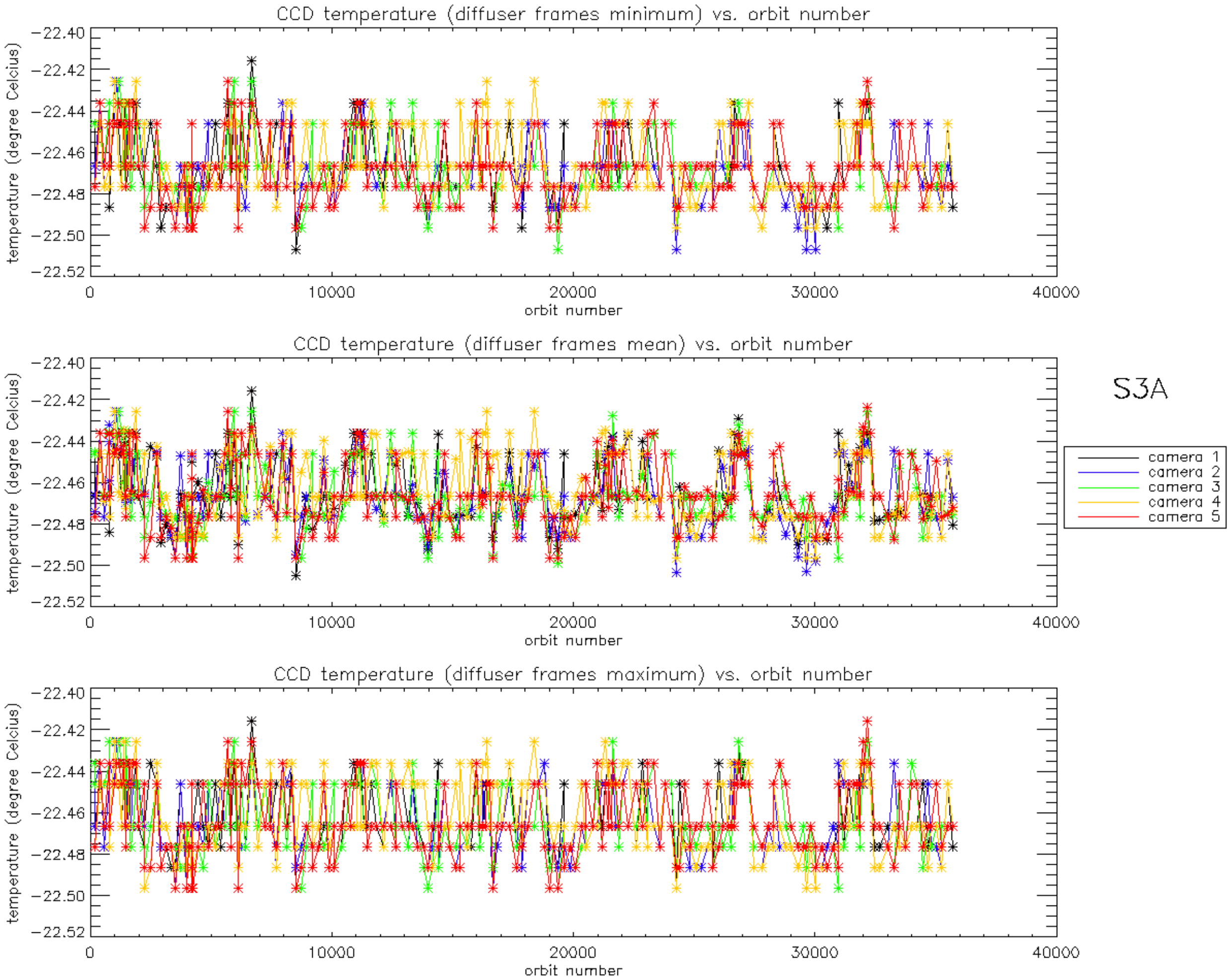

Figure 2: Same as Figure 1 for diffuser frames.

2.1.2 OLCI-B

As for OLCI-A, the variations of CCD temperature are very small (0.08 C peak-to-peak) and no trend can be identified. Data from current reporting period (rightmost data points) do not show any specificity.

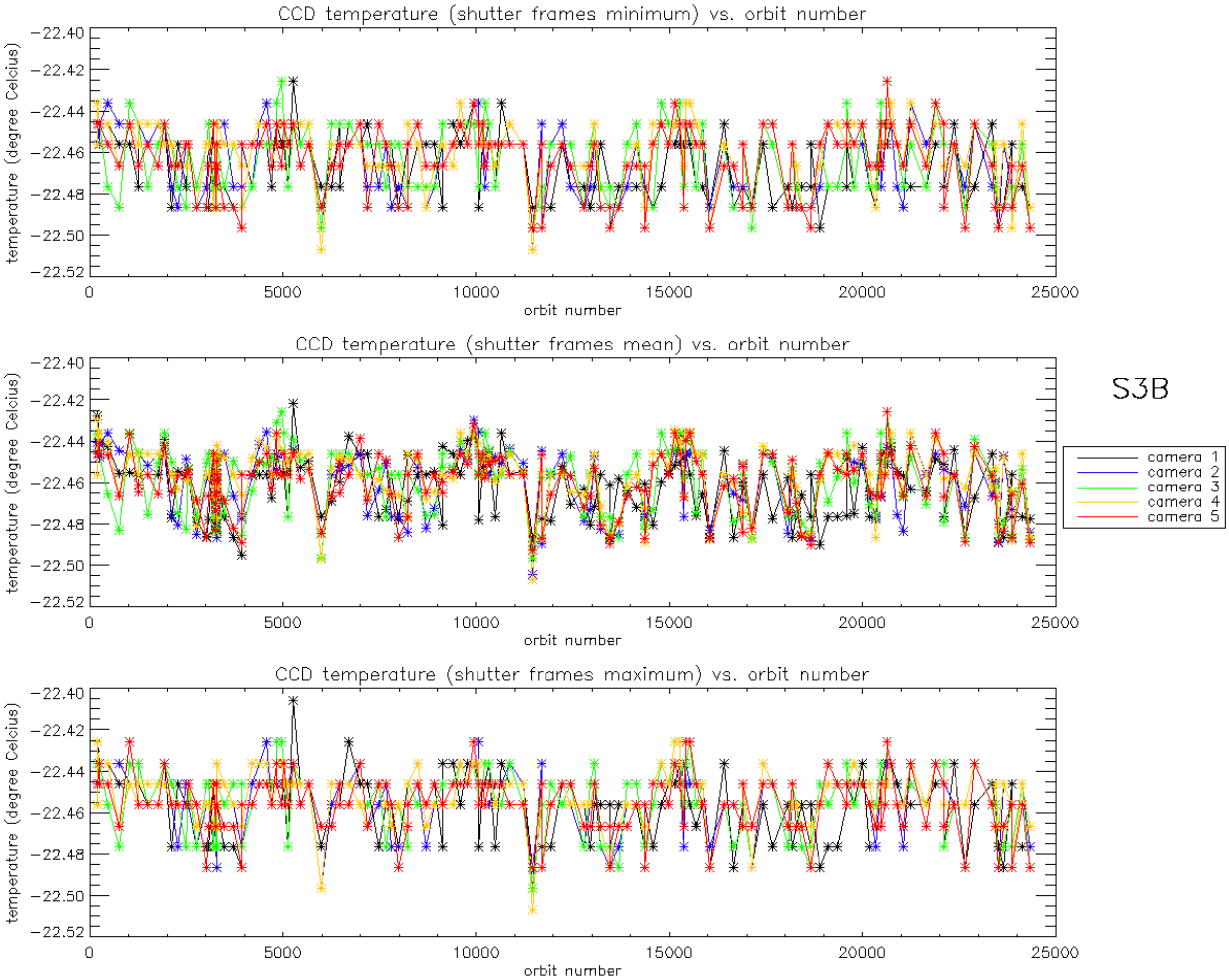

Figure 3: long term monitoring of OLCI-B CCD temperatures using minimum value (top), time averaged values (middle), and maximum value (bottom) provided in the annotations of the Radiometric Calibration Level 1 products, for the Shutter frames, all radiometric calibrations so far except the first one (absolute orbit 167) for which the instrument was not yet thermally stable.

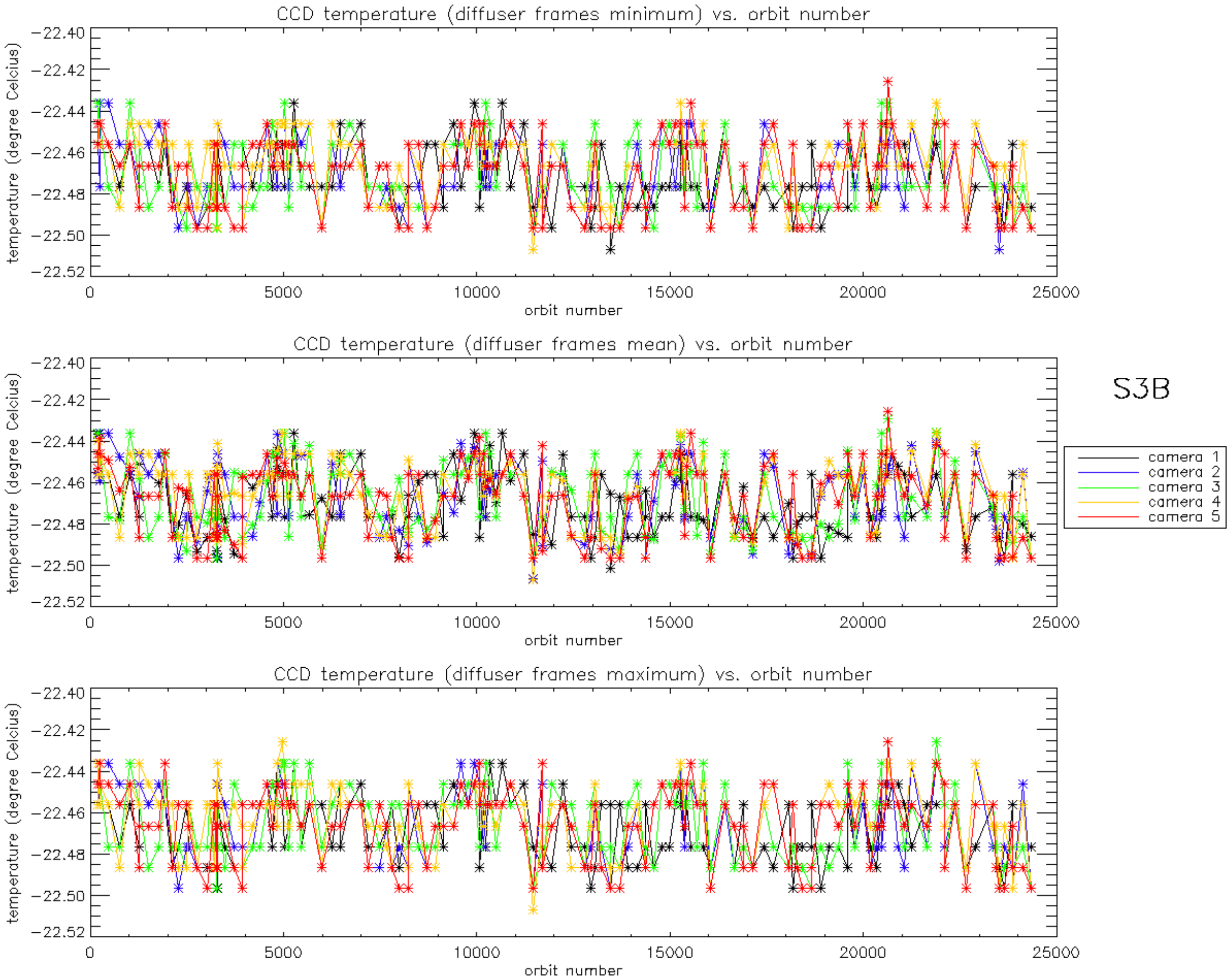

Figure 4: same as Figure 3 for diffuser frames.

2.2 Radiometric Calibration

For OLCI-A, two Radiometric Calibration sequences have been acquired during the reported period:

- S01 sequence (diffuser 1) on 11/12/2022 02:57 to 02:59 (absolute orbit 35496)
- S01 sequence (diffuser 1) on 26/12/2022 08:12 to 08:14 (absolute orbit 35713)

For OLCI-B, two Radiometric Calibration sequences have been acquired during the reported period:

- S01 sequence (diffuser 1) on 12/12/2022 13:39 to 13:41 (absolute orbit 24123)
- S01 sequence (diffuser 1) on 27/12/2022 10:28 to 10:30 (absolute orbit 24335)

The acquired Sun azimuth angles are presented on Figure 5 for OLCI-A and Figure 6 for OLCI-B, on top of the nominal values without Yaw Manoeuvre (i.e. with nominal Yaw Steering control of the satellite).

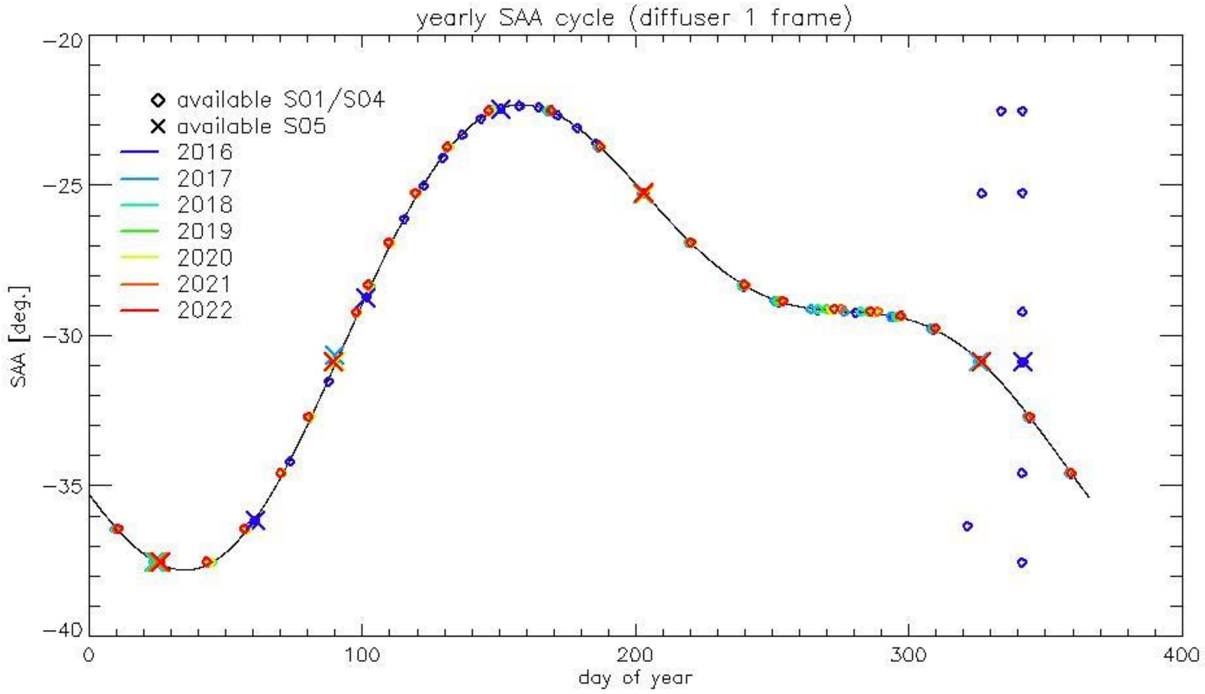

Figure 5: Sun azimuth angles during acquired OLCI-A Radiometric Calibrations (diffuser frame) on top of nominal yearly cycle (black curve). Diffuser 1 with diamonds, diffuser 2 with crosses. Different colours correspond to different years of acquisition (see the legend inside the figure).

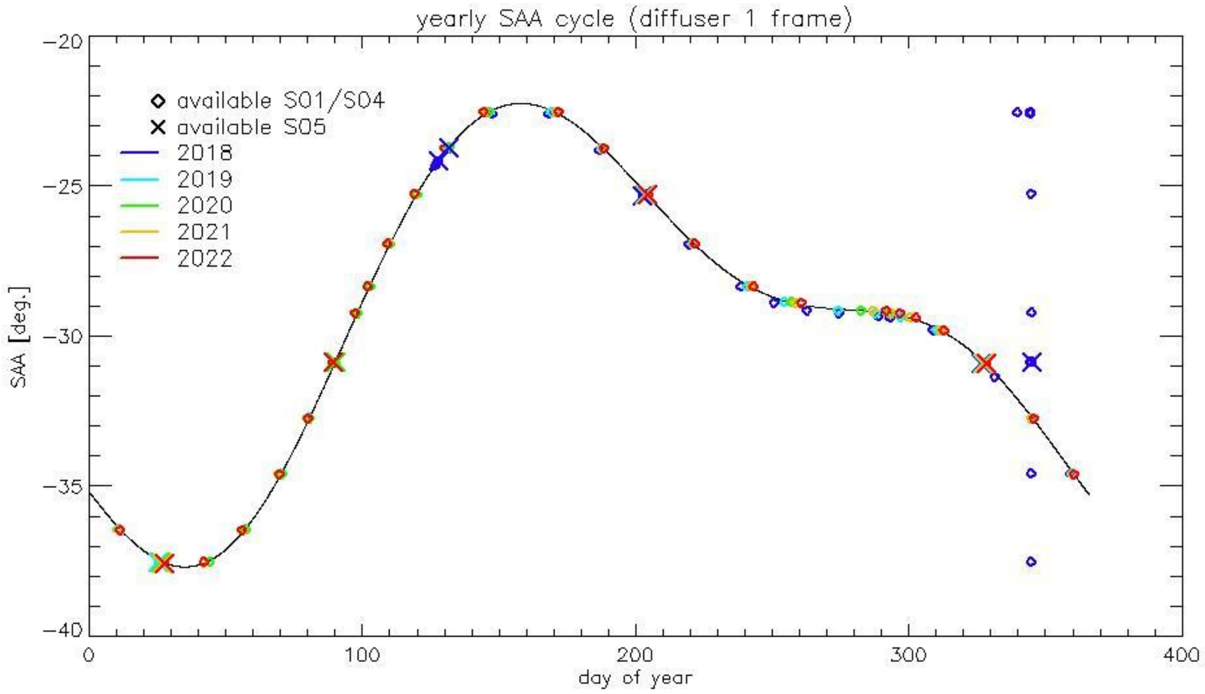

Figure 6: same as Figure 5 for OLCI-B.

Sun Zenith Angles as a function of Sun Azimuth Angles are presented in Figure 7 for OLCI-A and Figure 8 for OLCI-B.

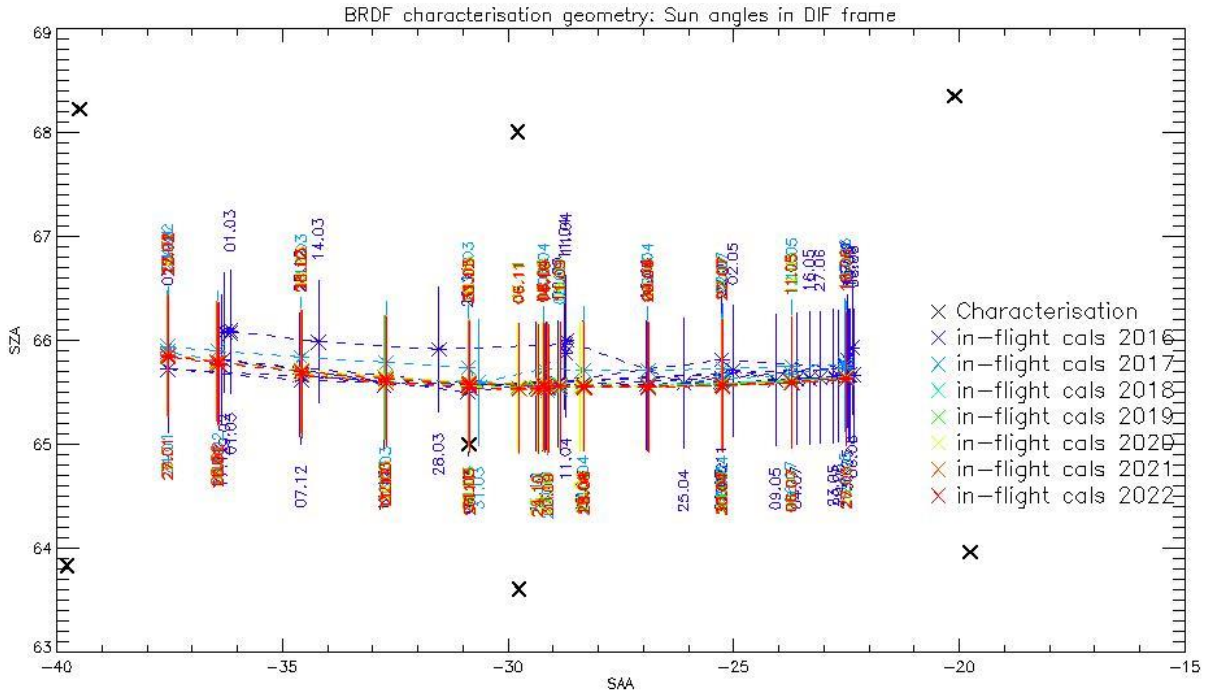

Figure 7: OLCI-A Sun geometry during radiometric Calibrations on top of characterization ones (diffuser frame)

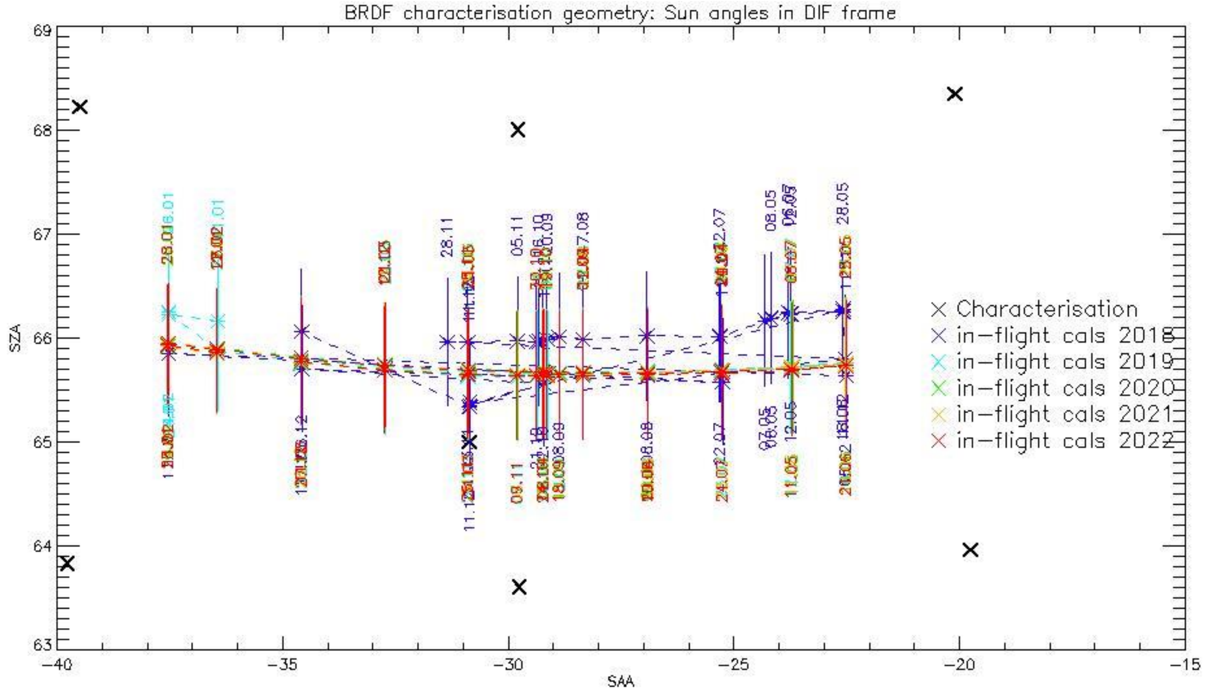

Figure 8: same as Figure 7 for OLCI-B

2.2.1 Dark Offsets [OLCI-L1B-CV-230]

<u>Note about the High Energy Particles:</u>

The filtering of High Energy Particle (HEP) events from radiometric calibration data has been implemented (for shutter frames only) in a post processor, allowing generating Dark Offset and Dark Current tables computed on filtered data. The post-processor starts from IPF intermediate data (corrected counts), applies the HEP detection and filtering and finally computes the Dark Offset and Dark Current tables the same way as IPF. An example of the impact of HEP filtering is given in Figure 9.

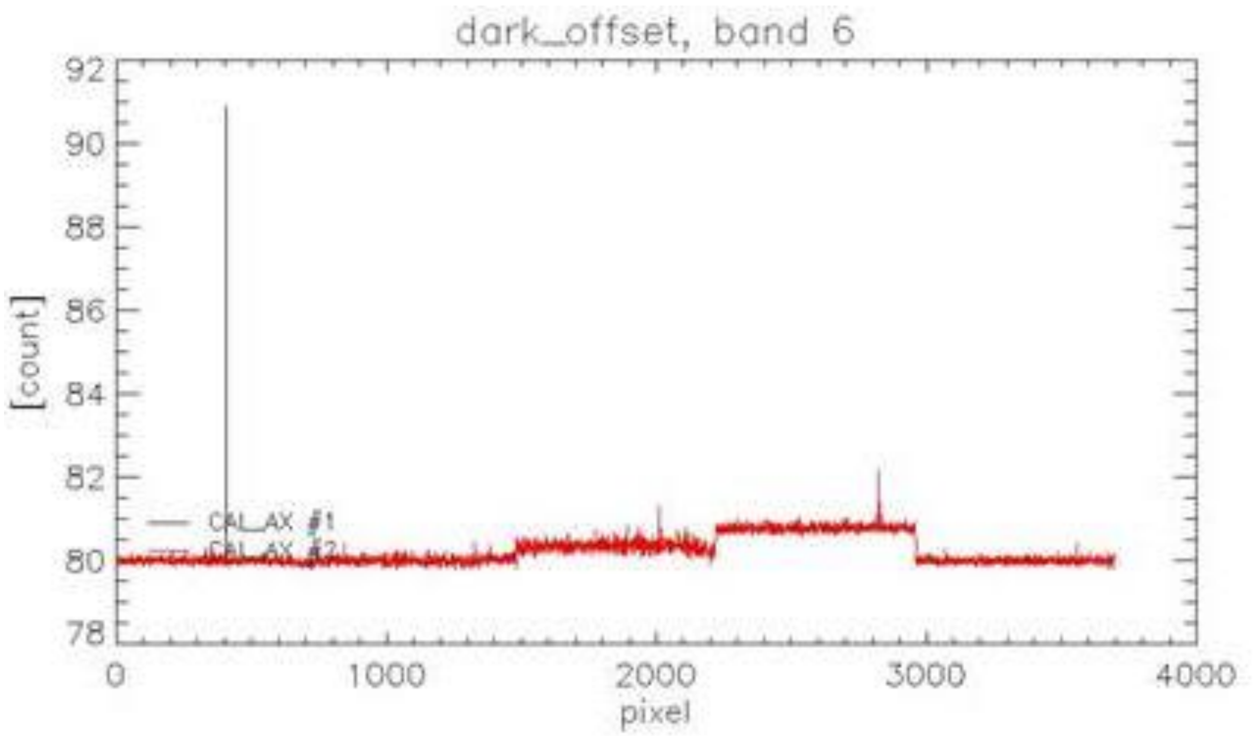

Figure 9: Dark Offset table for band Oa06 with (red) and without (black) HEP filtering (Radiometric Calibration of 22 July 2017). The strong HEP event near pixel 400 has been detected and removed by the HEP filtering.

All results presented below in this section have been obtained using the HEP filtered Dark Offset and Dark Current tables.

2.2.1.2 OLCI-A

Dark offsets

Dark offsets are continuously affected by the global offset induced by the Periodic Noise on the OCL (Offset Control Loop) convergence. Current reporting period calibrations are affected the same way as others. The amplitude of the shift varies with band and camera from virtually nothing (e.g. camera 2, band 0a1) to up to 5 counts (Oa21, camera 3). The Periodic Noise itself comes on top of the global shift with its known signature: high frequency oscillations with a rapid damp. This effect remains more or less stable with time in terms of amplitude, frequency and decay length, but its phase varies with time, introducing the global offset mentioned above.

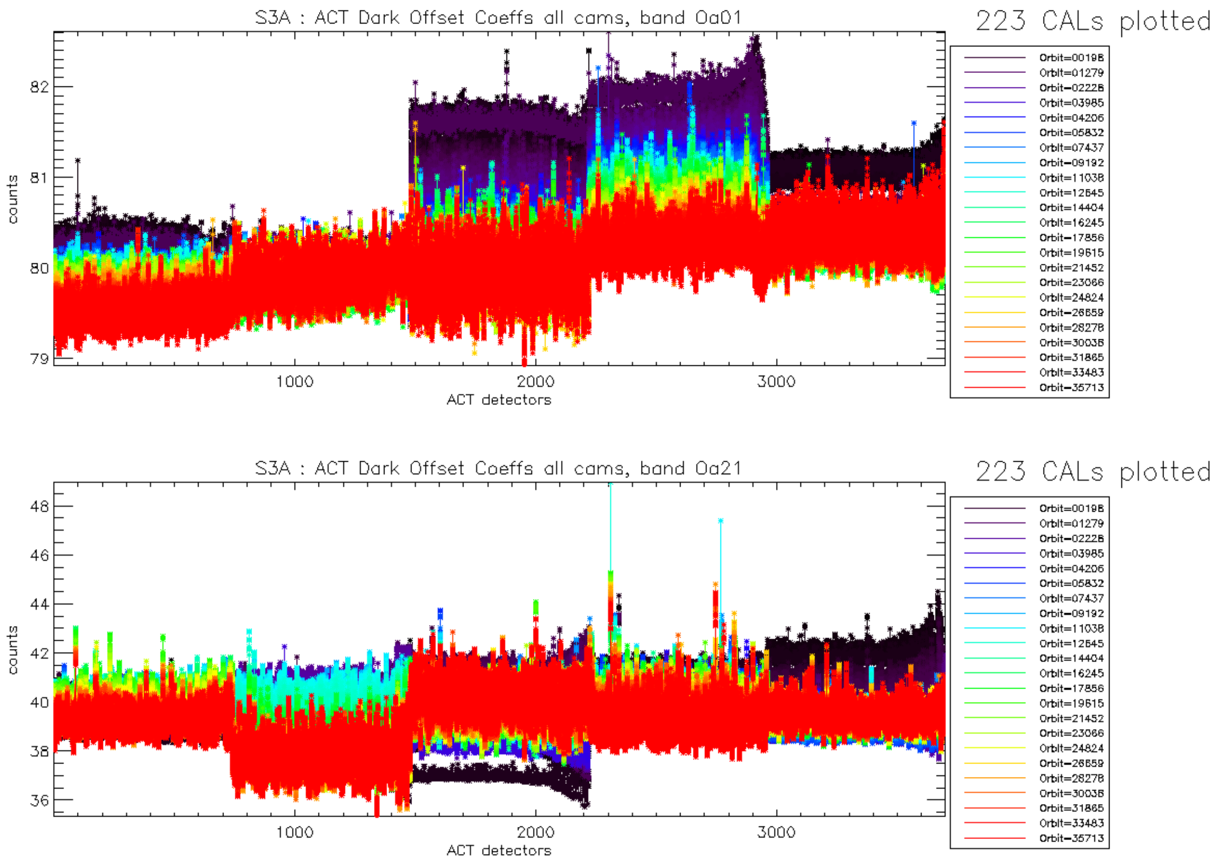

Figure 10: OLCI-A Dark Offset for band Oa1 (top) and Oa21 (bottom), all radiometric calibrations so far except the first one (orbit 183) for which the instrument was not thermally stable yet.

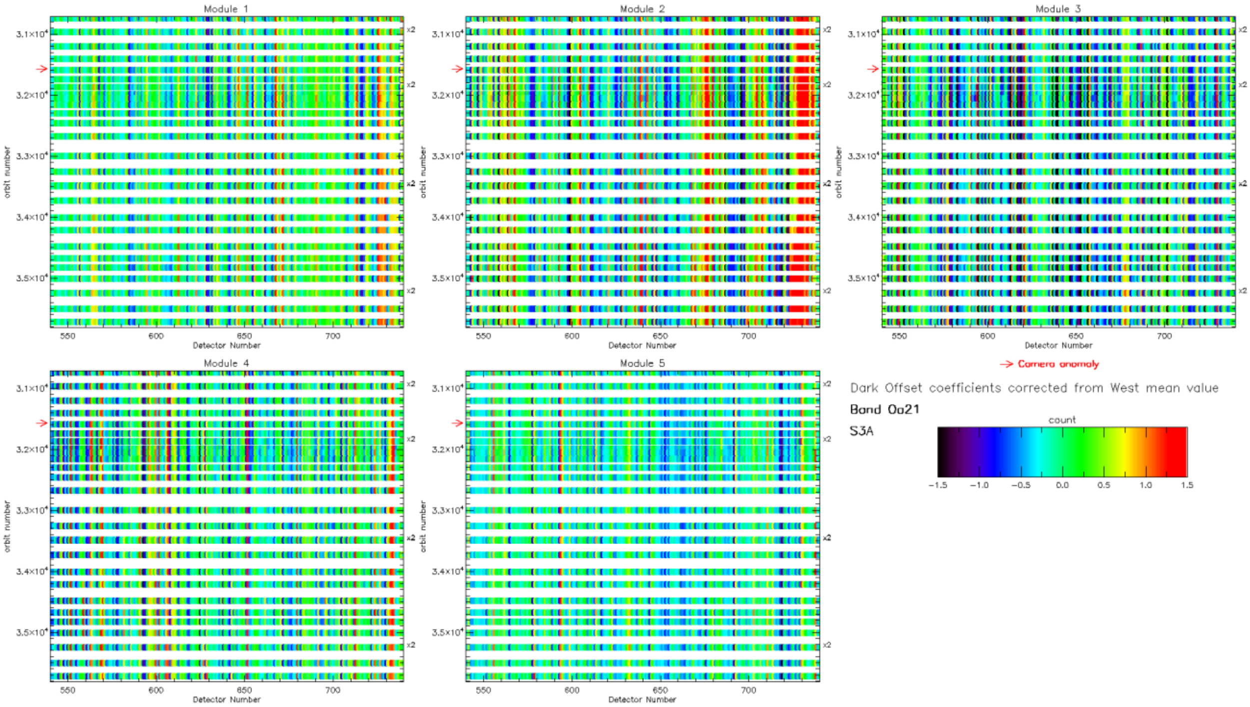

Figure 11: map of OLCI-A periodic noise for the 5 cameras, for band Oa21. X-axis is detector number (East part, from 540 to 740, where the periodic noise occurs), Y-axis is the orbit number. Y-axis range is focused on the most recent 5000 orbits. The counts have been corrected from the West detectors mean value (not affected by periodic noise) in order to remove mean level gaps and consequently to have a better visualisation of the long term evolution of the periodic noise structure. At the beginning of the mission the periodic noise for band Oa21 had strong amplitude in camera 2, 3 and 5 compared to camera 1 and 4. However PN evolved through the

mission and these discrepancies between cameras have been reduced. At the time of this Cyclic Report Camera 2 still shows a slightly higher PN than other cameras.

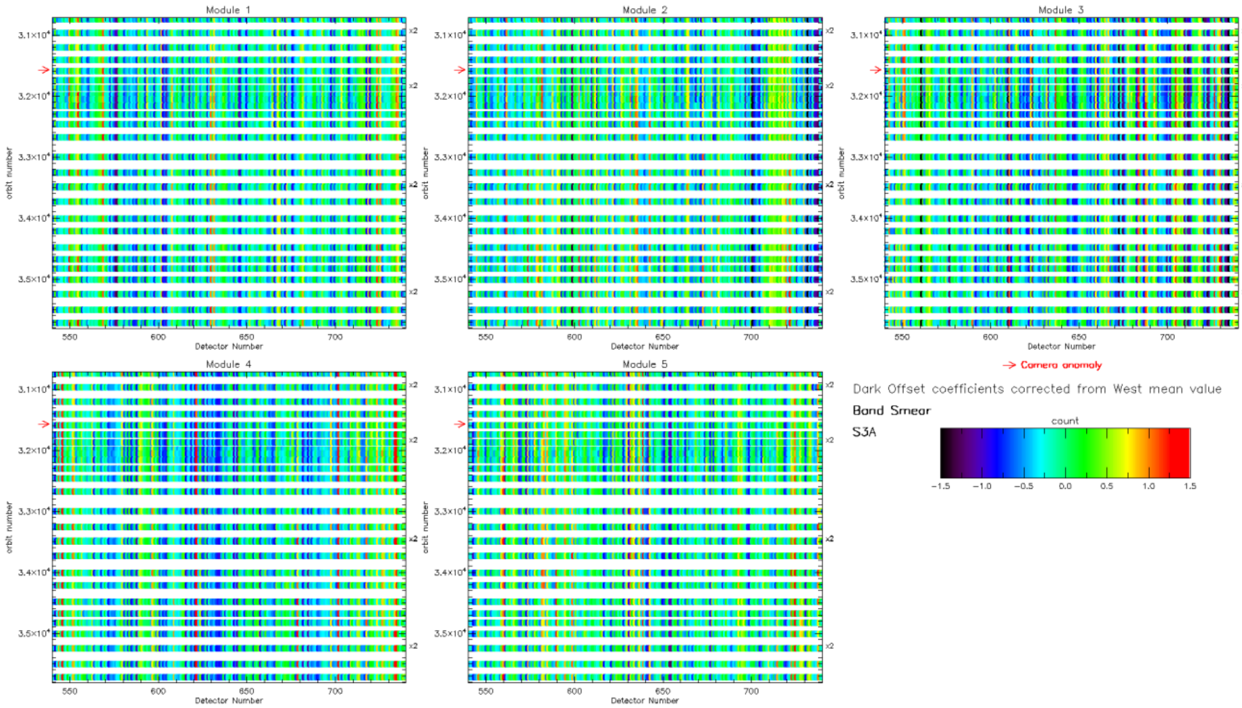

Figure 12: same as Figure 11 for smear band.

Figure 11 and Figure 12 show the so-called 'map of periodic noise' in the 5 cameras, for respectively band 21 and smear band. These maps have been computed from the dark offsets after removal of the mean level of the WEST detectors (not impacted by PN) in order to remove mean level gaps from one CAL to the other and consequently to highlight the shape of the PN. Maps are focused on the last 200 EAST detectors where PN occurs and on a time range covering only the last 5000 orbits in order to better visualize the CALs of the current reporting period.

Figure 11 and Figure 12 show that at this stage of the mission the PN is very stable in all cameras. There is no special behaviour noticed during the reporting period.

<u>Dark Currents</u>

Dark Currents (Figure 13) are not affected by the global offset of the Dark Offsets, thanks to the clamping to the average blind pixels value. However, the oscillations of Periodic Noise remain visible. There is no significant evolution of this parameter during the current reporting period except the small regular increase (almost linear), for all detectors, since the beginning of the mission (see Figure 14).

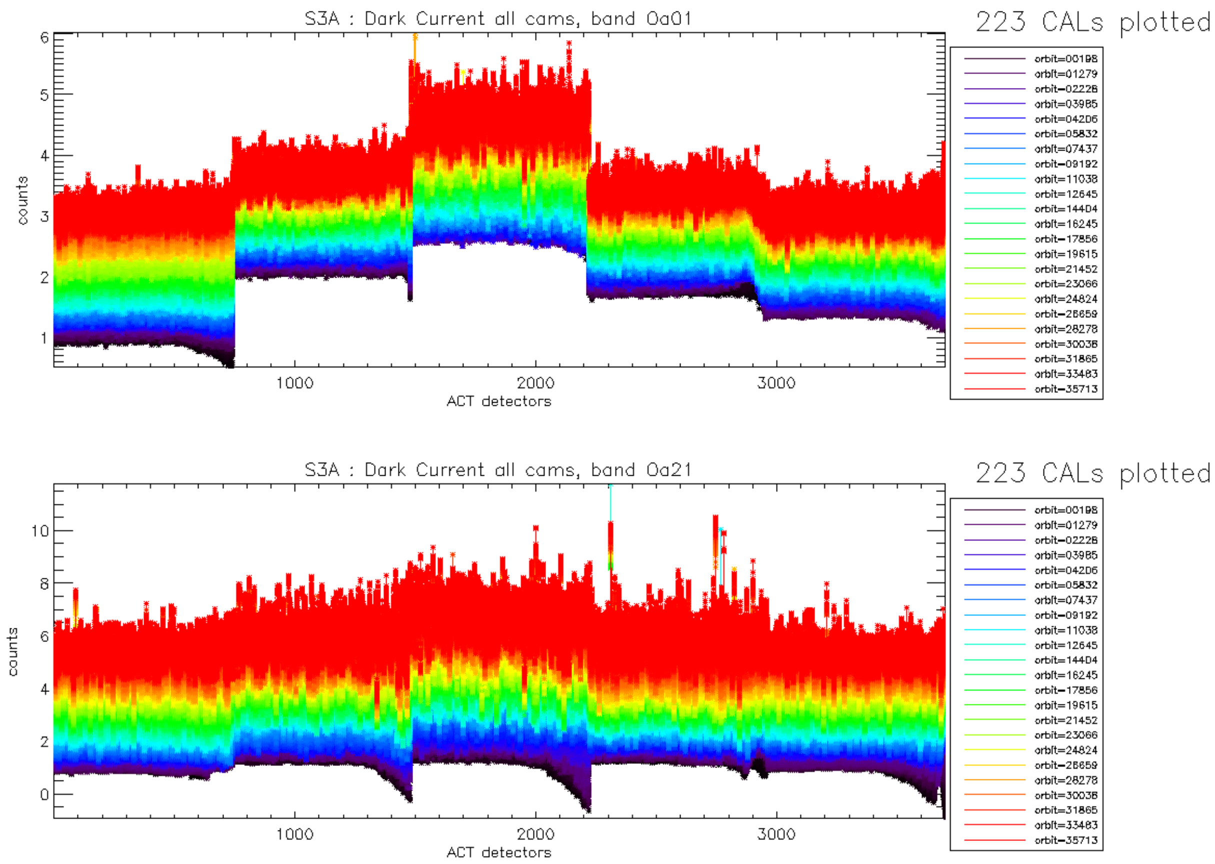

Figure 13: OLCI-A Dark Current for band Oa1 (top) and Oa21 (bottom), all radiometric calibrations so far except the first one (orbit 183) for which the instrument was not thermally stable yet.

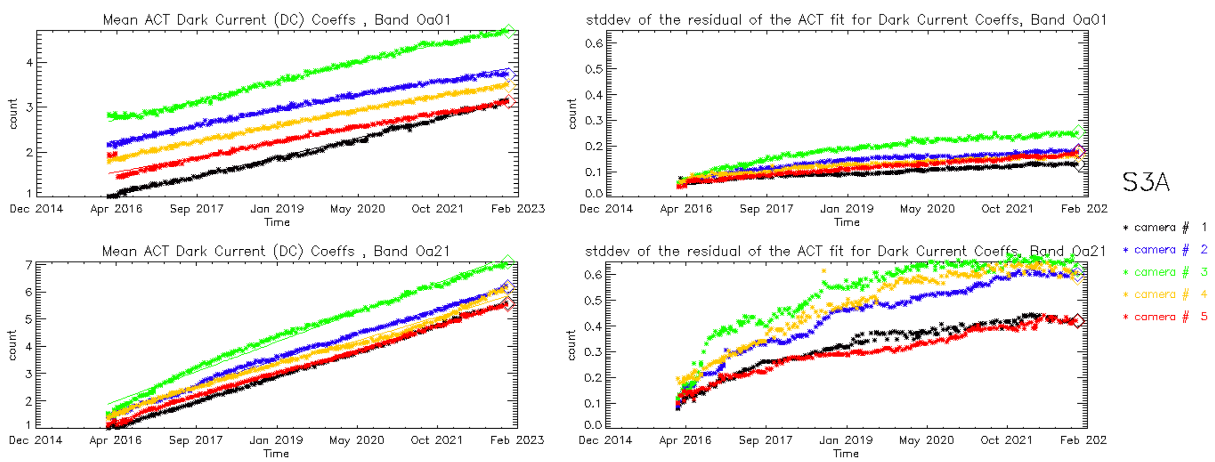

Figure 14: left column: ACT mean on 400 first detectors of OLCI-A Dark Current coefficients for spectral band Oa01 (top) and Oa21 (bottom). Right column: same as left column but for Standard deviation instead of mean. We see an increase of the DC level as a function of time especially for band Oa21.

A possible explanation of the regular increase of DC could be the increase of the number of hot pixels which is more important in Oa21 because this band is made of more CCD lines than band Oa01 and thus receives more cosmic rays impacts. It is known that cosmic rays degrade the structure of the CCD, generating more and more hot pixels at long term scales. Indeed, when computing the time slopes of the spatially averaged Dark Current as a function of band, i.e. the slopes of curves in left plots of Figure 14, one can see that Oa21 is by far the most affected, followed by the smear band (Figure 15, left); when plotting these slopes against total band width (in CCD rows, regardless of the number of micro-bands), the correlation between the slope values and the width becomes clear (Figure 15, right).

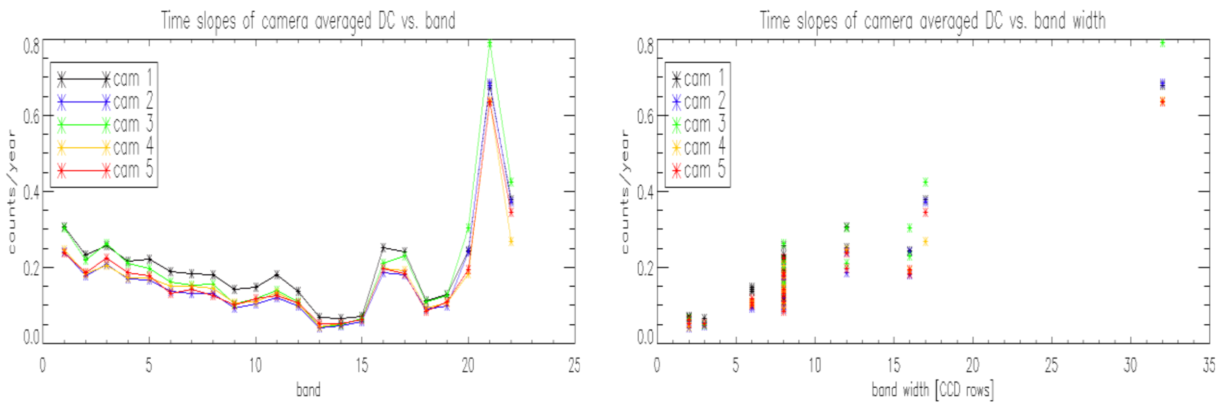

Figure 15: OLCI-A Dark current increase rates with time (in counts per year) vs. band (left) and vs. band width (right)

2.2.1.3 OLCI-B

<u>Dark Offsets</u>

Dark offsets for OLCI-B show a similar behaviour than for OLCI-A: mean level gaps between different orbits, induced by the presence of a pseudo periodic noise on the east edge of the cameras with a drifting phase.

Evolution of OLCI-B Dark Offset coefficients for band Oa01 and Oa21 are represented in Figure 16.

The periodic noise maps are shown for band Oa21 and smear band respectively in Figure 17 and Figure 18. As it happened for OLCI-A after a few thousands of orbits, the strong periodic noise phase and amplitude drift, present at the very beginning of the mission is now showing a clear stabilization.

Despite this overall stabilization, small evolutions are still noticeable in some bands/camera, like for example camera 1 in band Oa21 (upper left map in Figure 17) or in camera 1 band smear (upper left map in Figure 18).

Globally, OLCI-B PN is slightly less stabilized than OLCI-A PN.

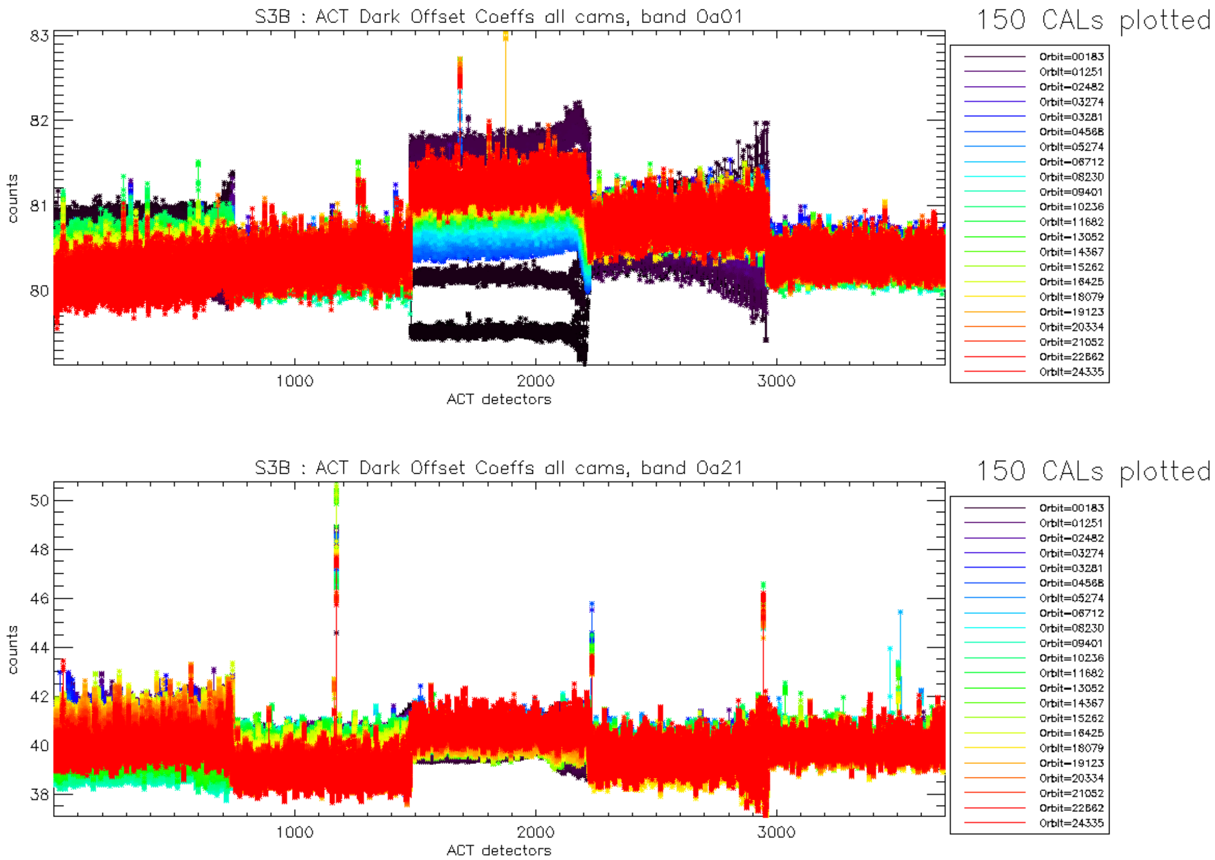

Figure 16: OLCI-B Dark Offset for band Oa1 (top) and Oa21 (bottom), all radiometric calibrations so far except the first one (orbit 167) for which the instrument was not thermally stable yet.

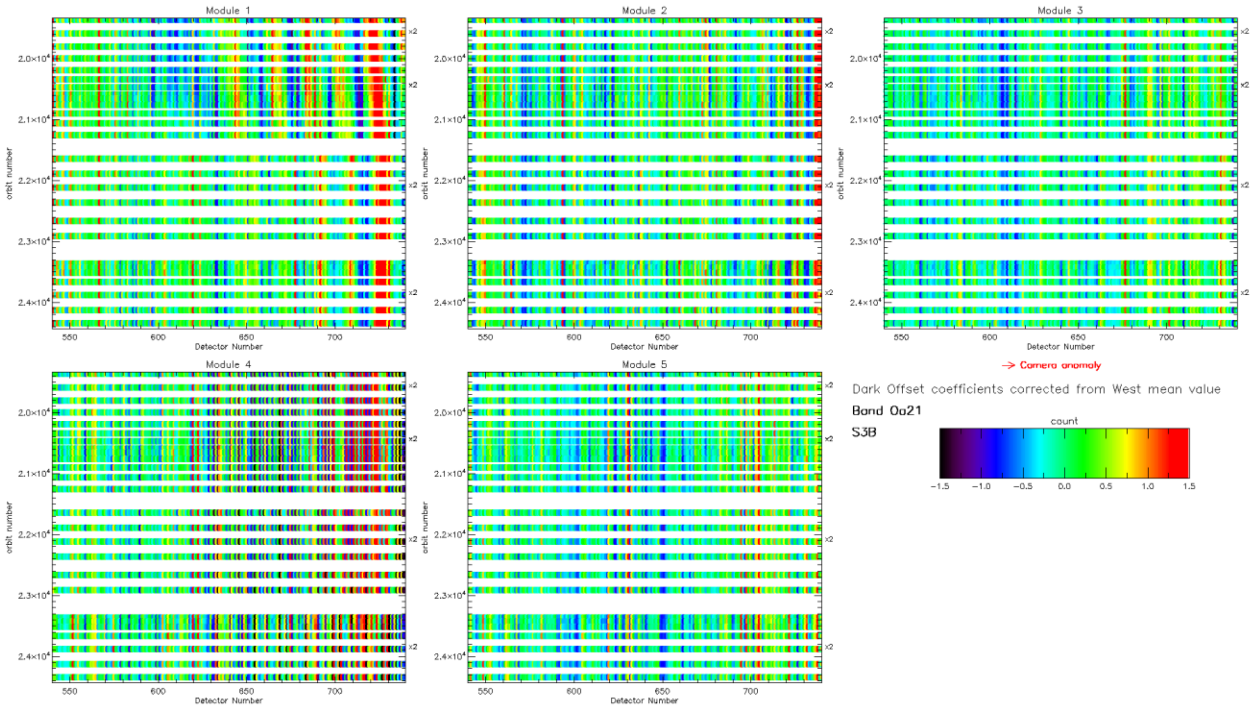

Figure 17: OLCI-B map of periodic noise for the 5 cameras, for band Oa21. X-axis is detector number (East part, from 540 to 740, where the periodic noise occurs), Y-axis is the orbit number. The counts have been corrected from the West detectors mean value (not affected by periodic noise) in order to remove mean level gaps and consequently to have a better visualisation of the long term evolution of the periodic noise structure.

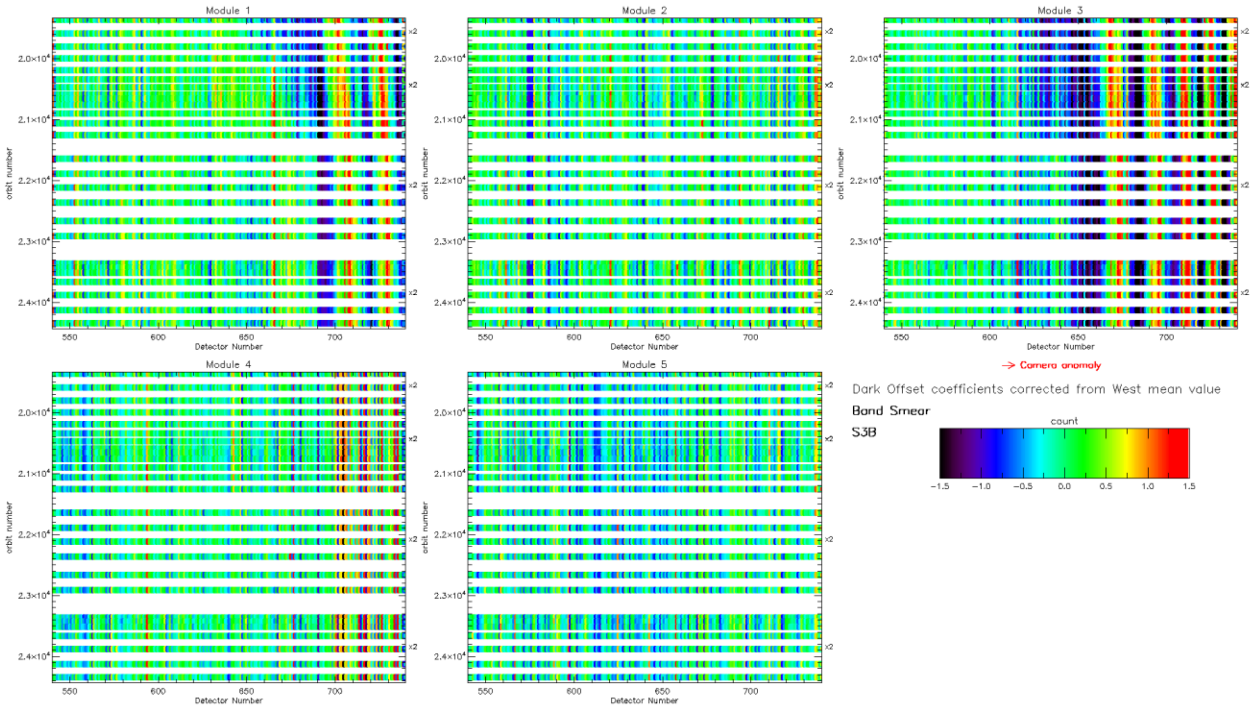

Figure 18: same as Figure 17 for smear band.

<u>Dark Currents</u>

As for OLCI-A there is no significant evolution of the Dark Current coefficients (Figure 19) during the current reporting period except the small regular increase (almost linear), for all detectors, since the beginning of the mission (see Figure 20) probably due to an increase of hot pixels (see Figure 21).

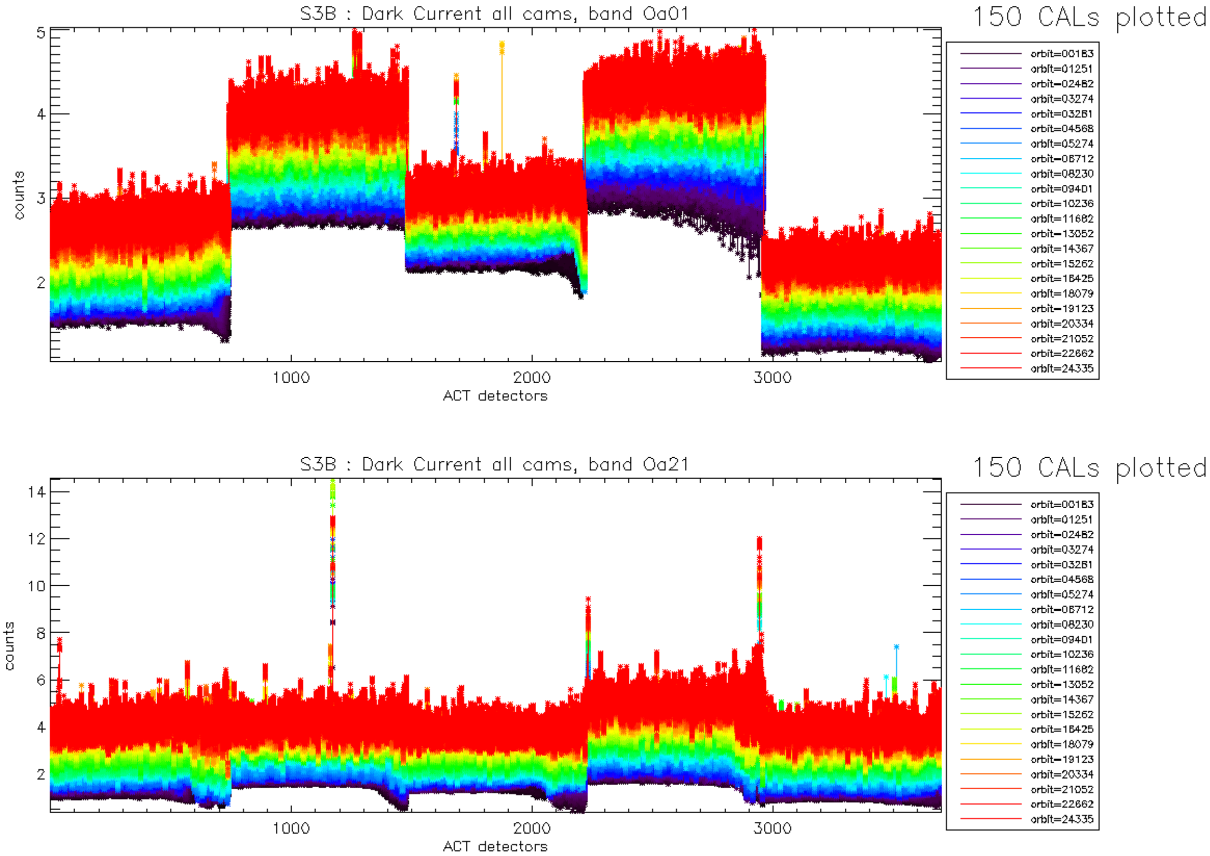

Figure 19: OLCI-B Dark Current for band Oa1 (top) and Oa21 (bottom), all radiometric calibrations so far except the first one (orbit 167) for which the instrument was not thermally stable yet.

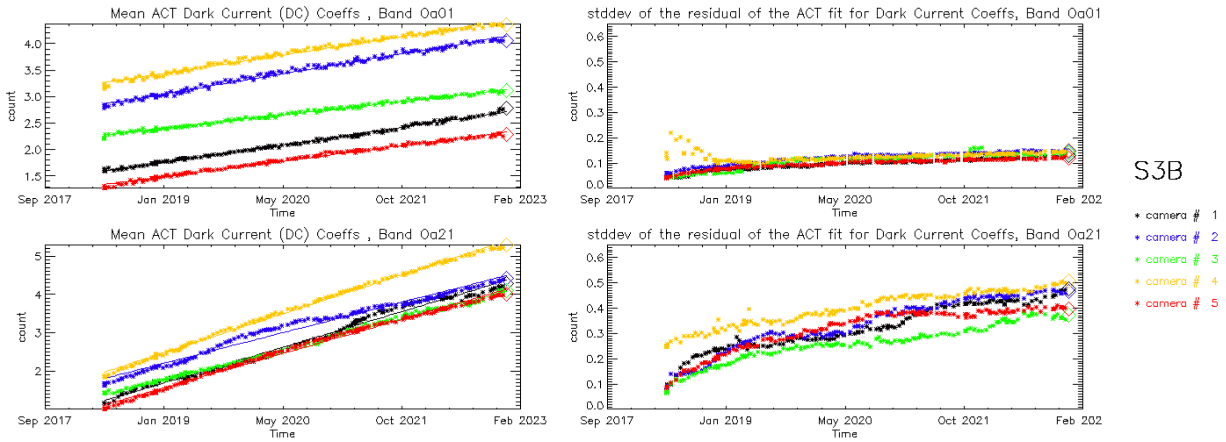

Figure 20: left column: ACT mean on 400 first detectors of OLCI-B Dark Current coefficients for spectral band Oa01 (top) and Oa21 (bottom). Right column: same as left column but for Standard deviation instead of mean. We see an increase of the DC level as a function of time especially for band Oa21.

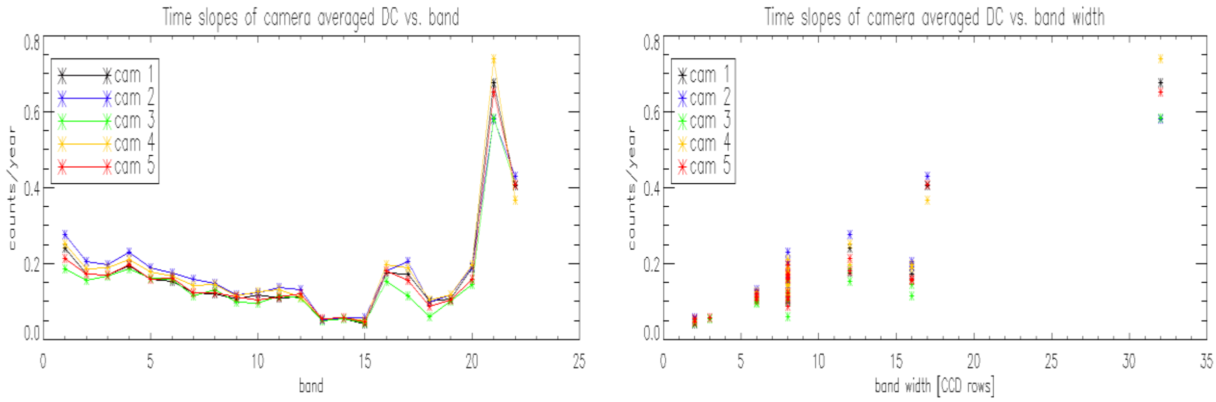

Figure 21: OLCI-B Dark Current increase rates with time (in counts per year) vs. band (left) and vs. band width (right)

2.2.3 Instrument response and degradation modelling [OLCI-L1B-CV-250]

2.2.3.1 Instrument response monitoring

2.2.3.1.1 OLCI-A

Figure 22 shows the gain coefficients of every pixel for two OLCI-A channels, Oa1 (400 nm) and Oa21 (1020 nm), highlighting the significant evolution of the instrument response since early mission.

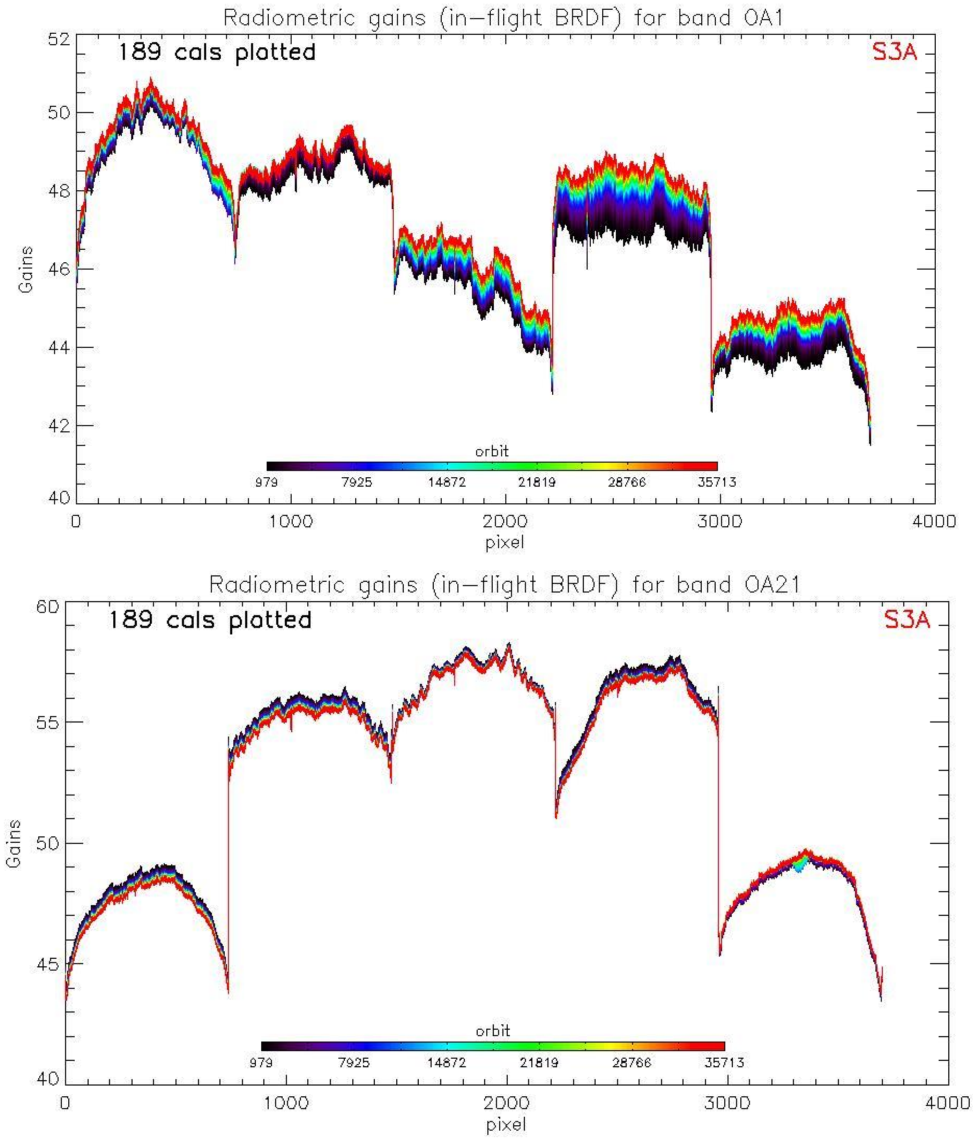

Figure 22: OLCI-A Gain Coefficients for band Oa1 (top) and Oa21 (bottom), derived using the in-flight BRDF model. The dataset is made of all diffuser 1 radiometric calibrations since orbit 979.

Figure 23 displays a summary of the time evolution of the cross-track average of the gains (in-flight BRDF, taking into account the diffuser ageing), for each module, relative to a given reference calibration (the 25/04/2016, change of OLCI channel settings). It shows that, if a significant evolution occurred during the early mission, the trends tend in general to stabilize, with some exceptions (e.g. band 1 of camera 1 and 4, bands 2 & 3 of camera 5).

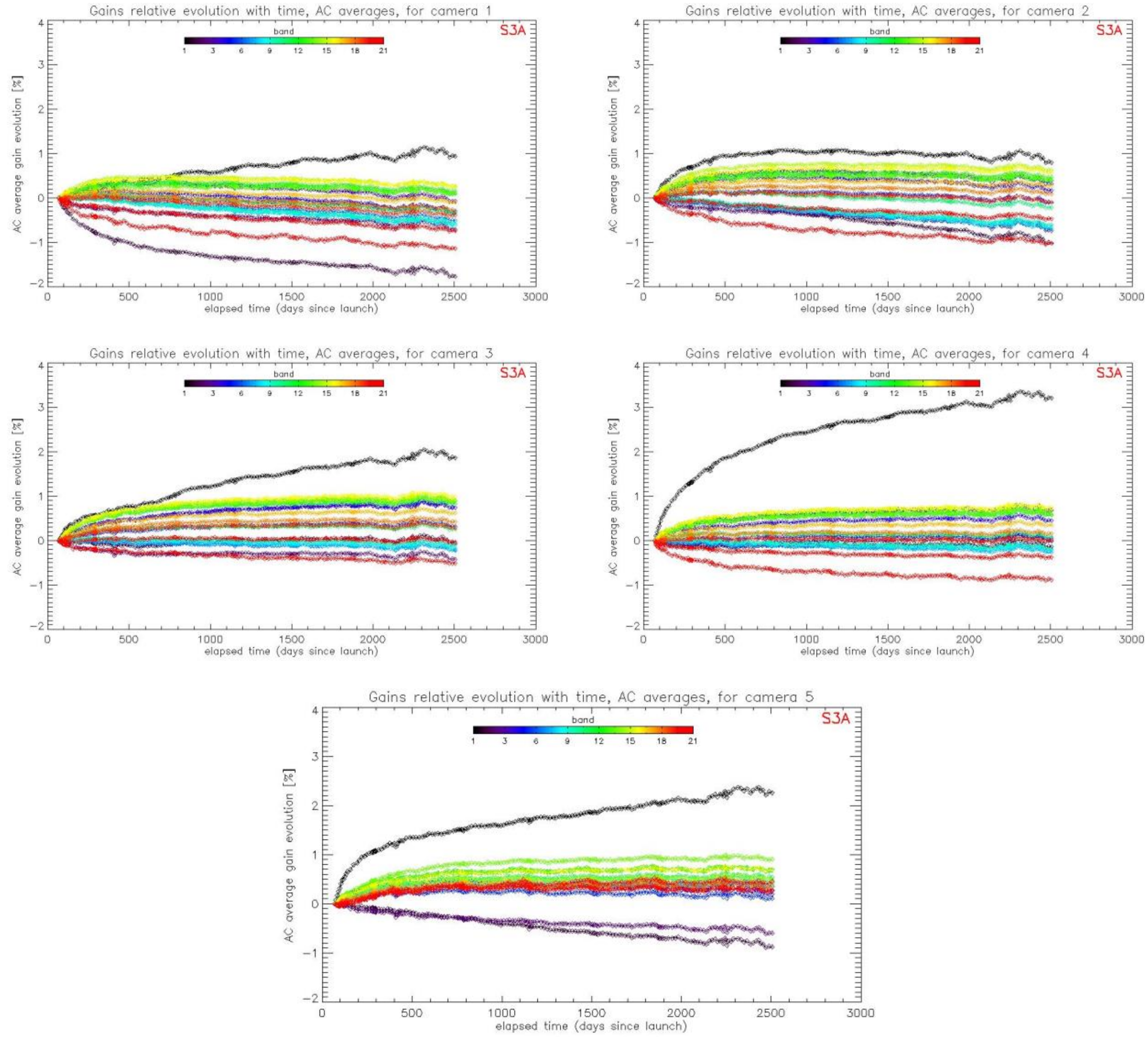

Figure 23: camera averaged gain relative evolution with respect to calibration of 25/04/2016 (change of OLCI channel settings), as a function of elapsed time since the beginning of the mission; one curve for each band (see colour code on plots), one plot for each module. The diffuser ageing is taken into account.

2.2.3.1.2 OLCI-B

Figure 24 shows the gain coefficients of every pixel for two OLCI-B channels, Oa1 (400 nm) and Oa21 (1020 nm), highlighting the significant evolution of the instrument response since early mission.

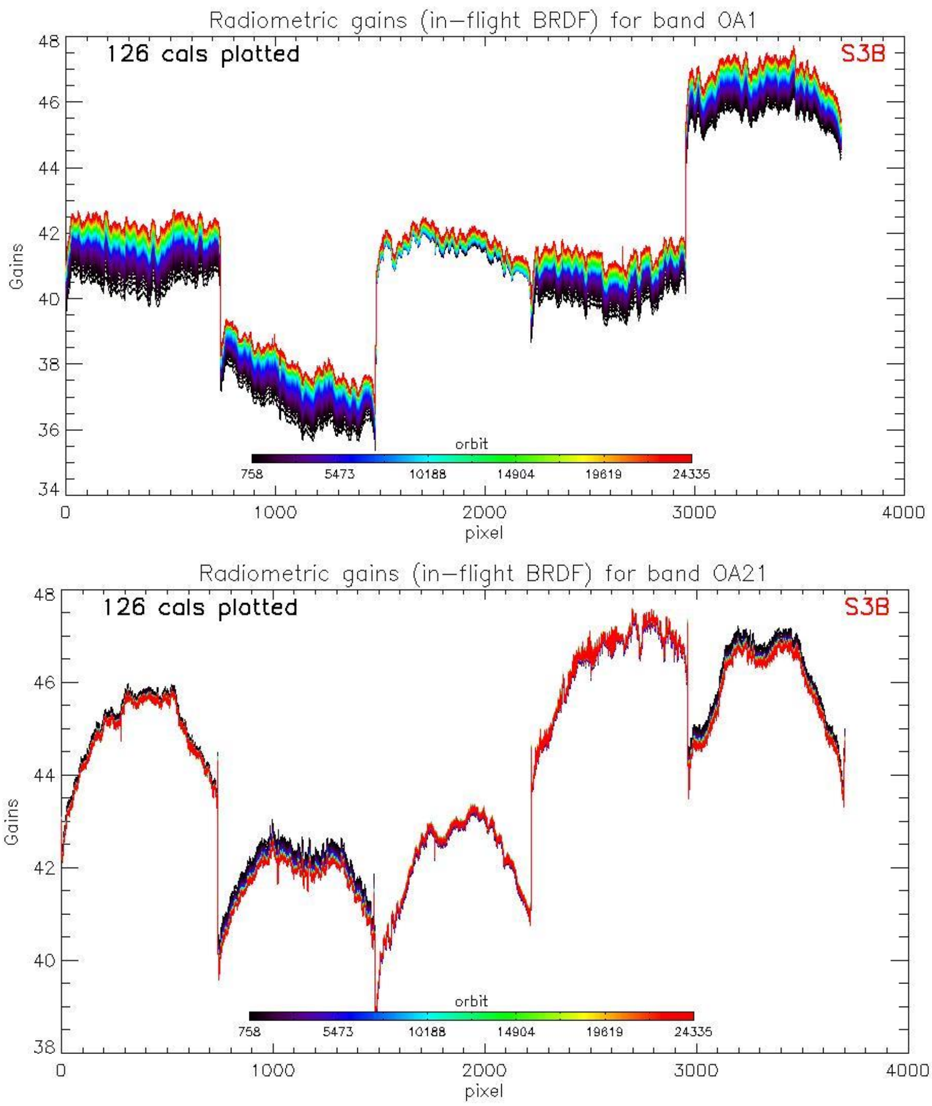

Figure 24: OLCI-B Gain Coefficients for band Oa1 (top) and Oa21 (bottom), derived using the in-flight BRDF model. The dataset is made of all diffuser 1 radiometric calibrations since orbit 758.

Figure 25 displays a summary of the time evolution of the cross-track average of the gains (in-flight BRDF, taking into account diffuser ageing), for each module, relative to a given reference calibration (first calibration after channel programming change: 18/06/2018). It shows that, if a significant evolution occurred during the early mission, the trends tend to stabilize. The large amount of points near elapsed time = 220 days is due to the yaw manoeuvre campaign. The slight discontinuity near "day 920 since launch" is due to the upgrade of the Ageing model.

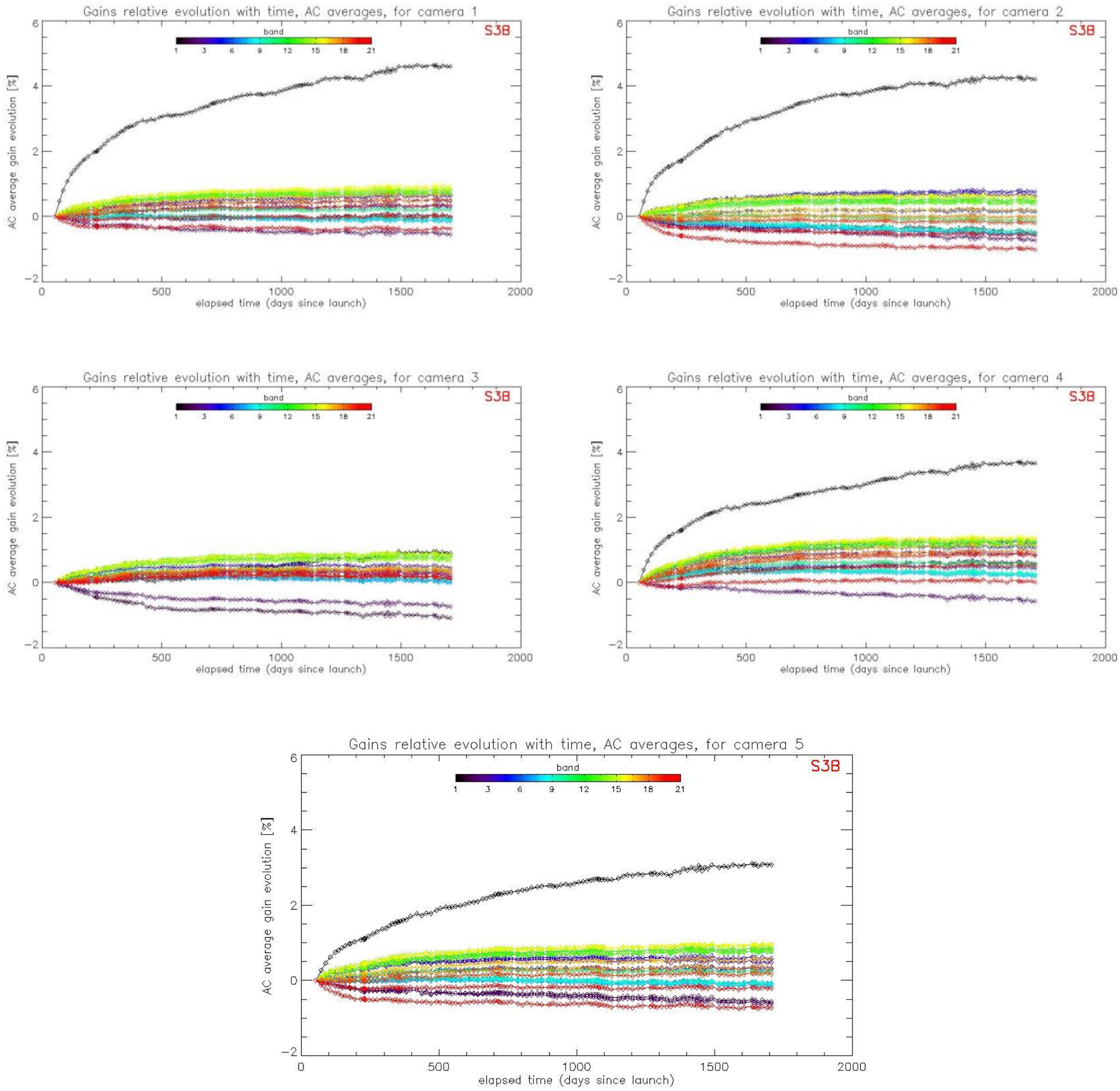

Figure 25: OLCI-B camera averaged gain relative evolution with respect to first calibration after channel programming change (18/06/2018), as a function of elapsed time since the beginning of the mission; one curve for each band (see colour code on plots), one plot for each module. The diffuser ageing is taken into account.

2.2.3.2 Instrument evolution modelling

2.2.3.2.1 OLCI-A

A new OLCI-A Radiometric Gain Model has been put in operations at PDGS the 19/07/2022 (Processing Baseline 3.09). This model has been derived on the basis of a more recent (compared to the previous model) Radiometric Calibration dataset, going from 23/10/2018 to 30/04/2022. It includes the correction of the diffuser ageing for the six bluest bands (Oa1 to Oa6) for which it is clearly measurable. The model performance over the complete dataset (including the 15 calibrations in extrapolation over about 8 months) remains better than about 0.1% for all bands at the exception of Oa01 which shows the presence of a strong peak near orbit 33000 reaching about 0.16%. This peak is also present for other bands but with a smaller amplitude. The presence of this peak makes it difficult to assess if any small drift of the model with respect to the most recent data is already visible or not. The previous model, trained on a Radiometric Dataset limited to 03/10/2021, shows a clear drift of the model with respect to most recent data (Figure 27), that motivated the change. Comparison of the two figures shows the improvement brought by the updated model over almost all the mission. Performance shown on Figure 26 adopts, as for OLCI-B, the multiple model approach, i.e. different models (three for OLCI-A since PB, three for OLCI-B since PB 1.57) are used to cover the whole mission (red dashed line on Figure 26), each model being fitted on a partial dataset (green dashed line on Figure 26) whose coverage is optimised to provide best performance.

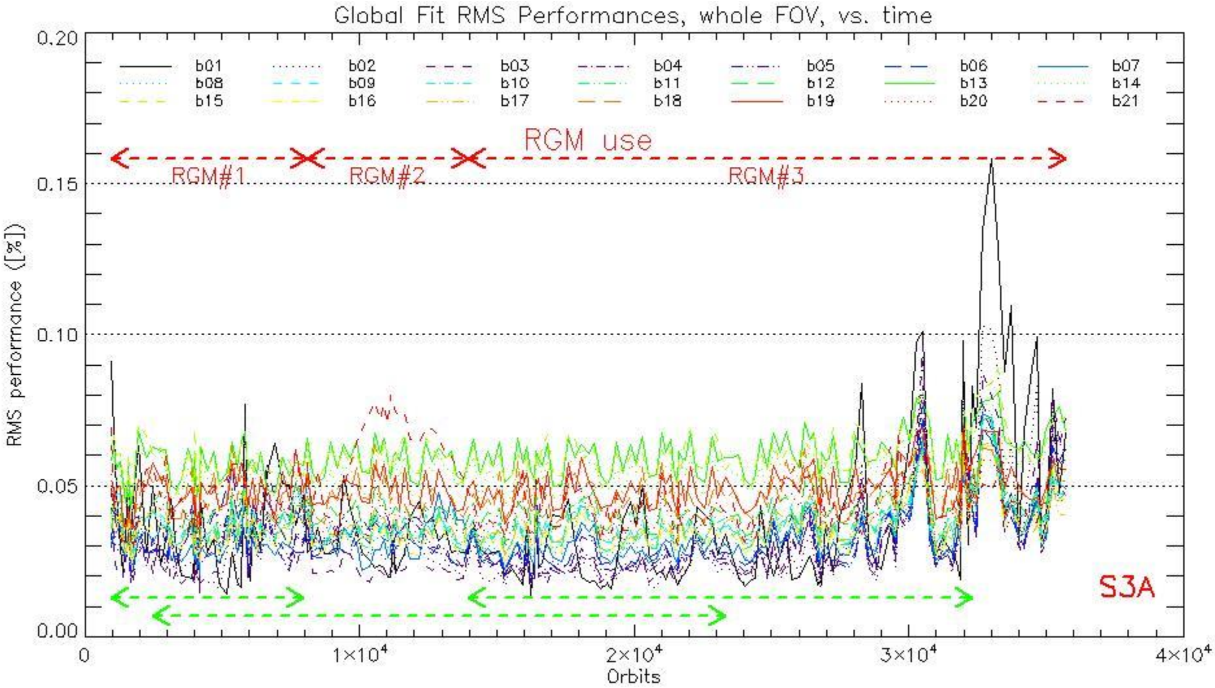

Figure 26: RMS performance of the OLCI-A Gain Model of the current processing baseline as a function of orbit.

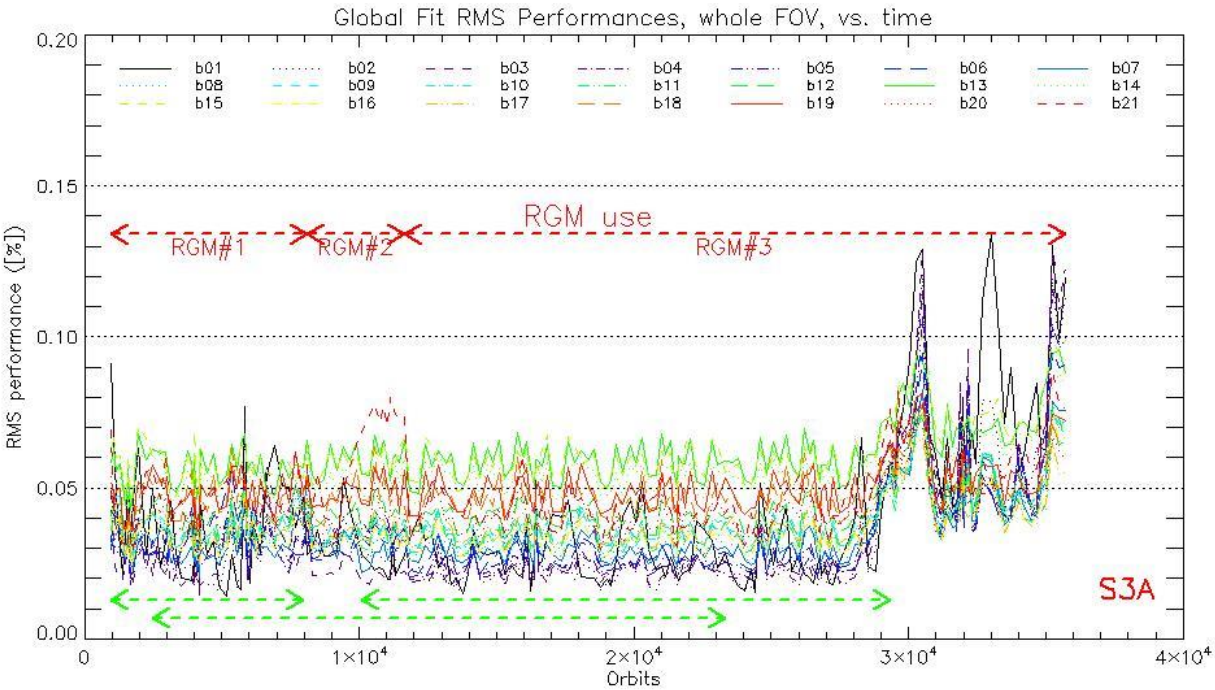

Figure 27: RMS performance of the OLCI-A Gain Model of the previous Processing Baseline as a function of orbit.

The overall instrument evolution since channel programming change (25/04/2016) is shown on Figure 28.

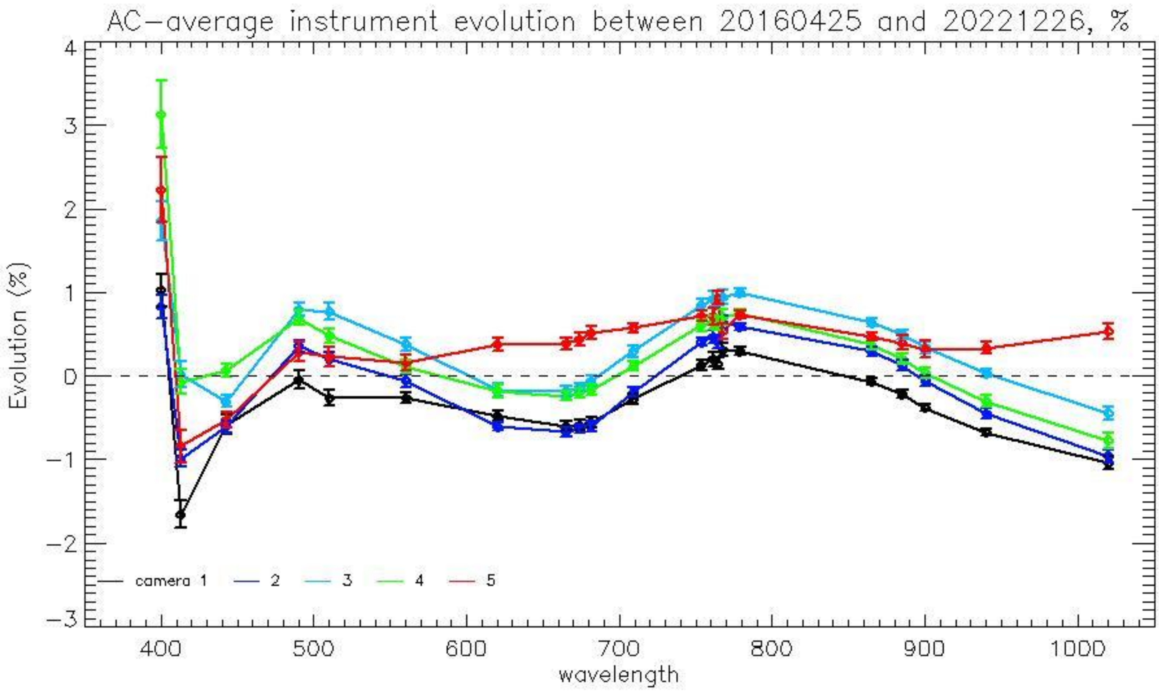

Figure 28: OLCI-A Camera-averaged instrument evolution since channel programming change (25/04/2016) and up to the most recent calibration (26/12/2022) versus wavelength.

The overall per camera performance, as a function of wavelength, and at each orbit is shown on Figure 29 as the average and standard deviation of the model over data ratio.

Finally, Figure 30 to Figure 32 show the detail of the model performance, with across-track plots of the model over data ratios at each orbit, one plot for each channel.

Comparisons of Figure 30 to Figure 32 with their counterparts in DQR of July 2022 clearly demonstrate the improvement brought by the new model whatever the level of detail.

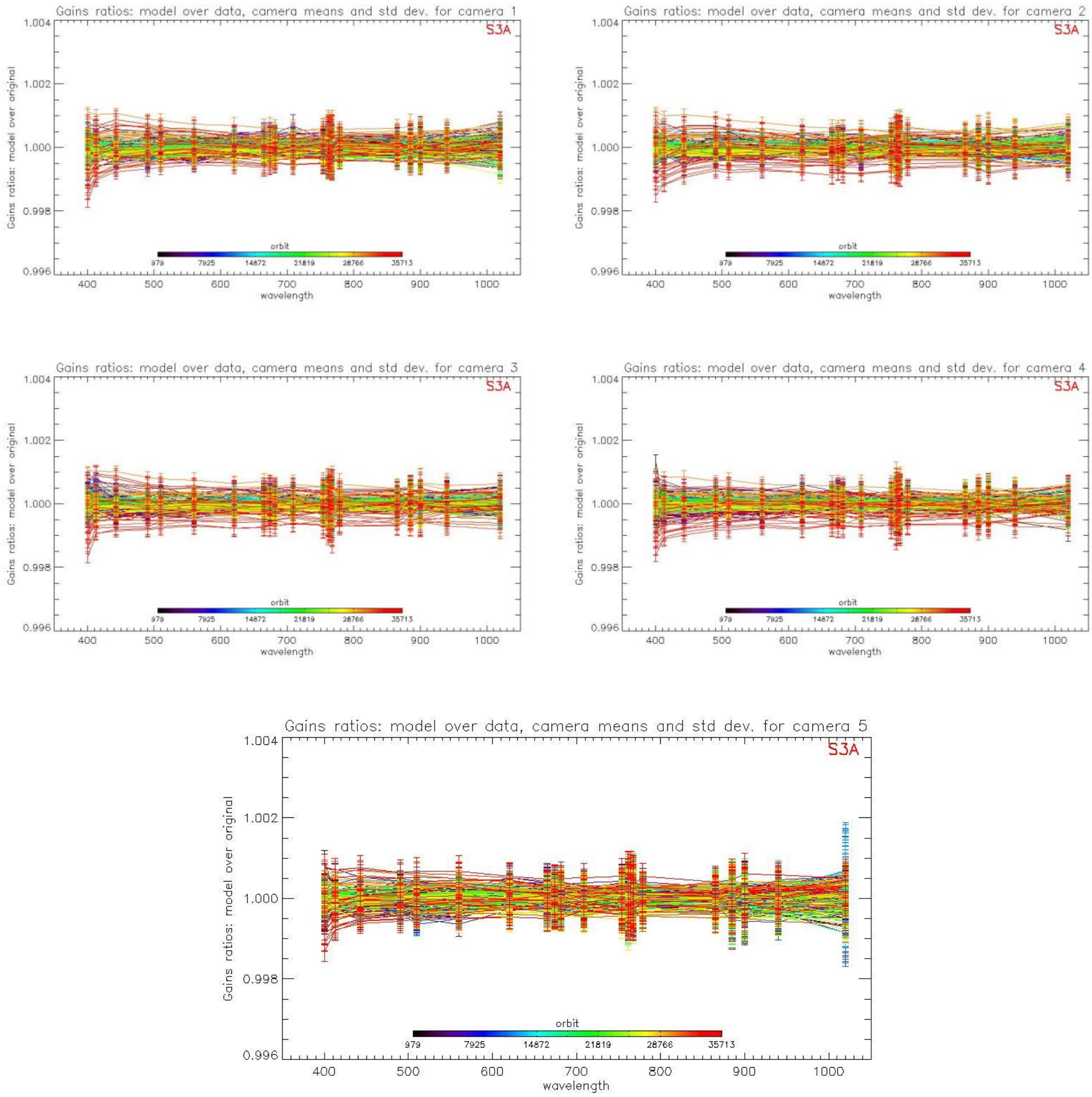

Figure 29: For the 5 cameras: OLCI-A Evolution model performance, as camera-average and standard deviation of ratio of Model over Data vs. wavelength, for each orbit of the test dataset, including 15 calibrations in extrapolation, with a colour code for each calibration from blue (oldest) to red (most recent).

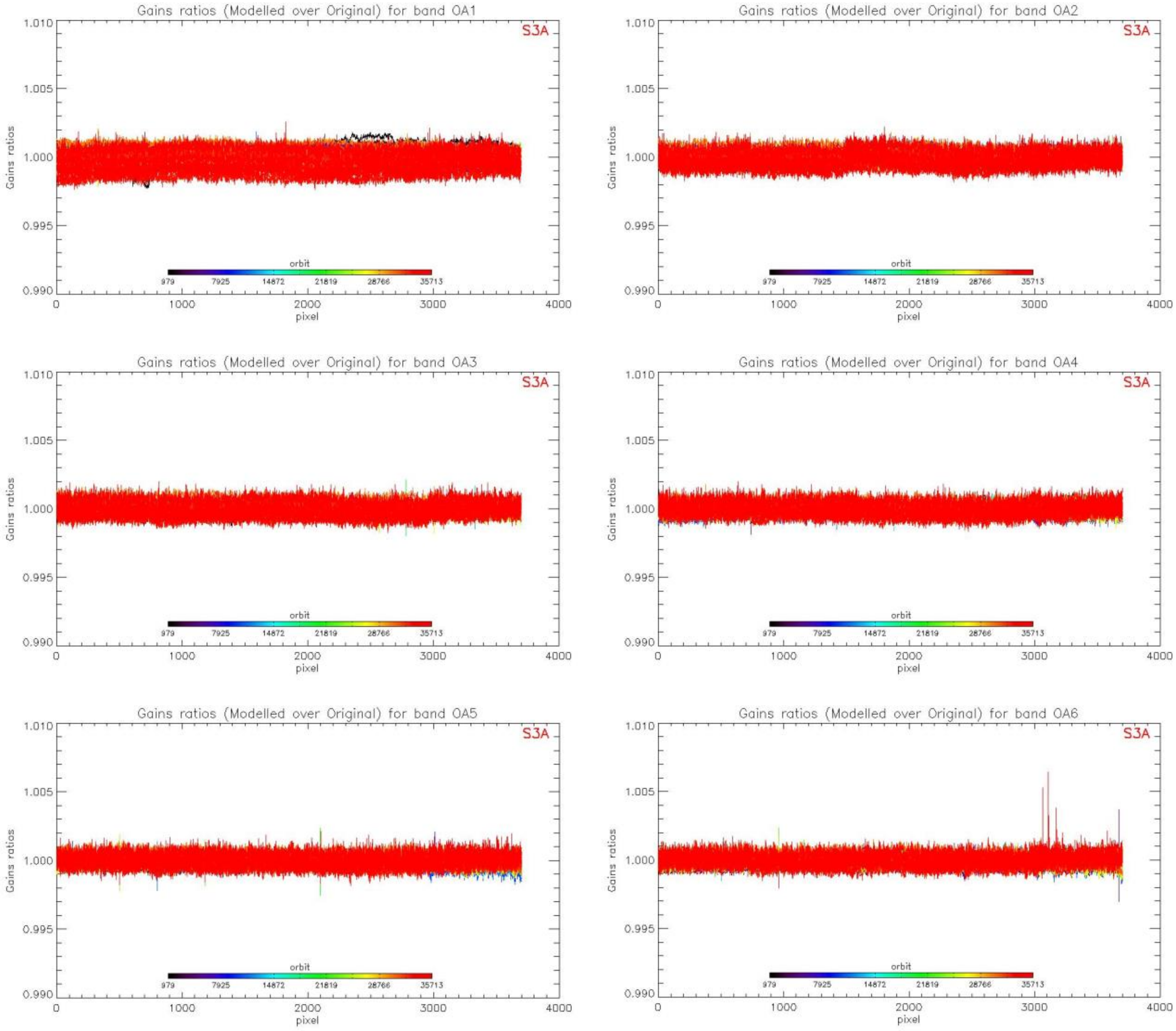

Figure 30: OLCI-A evolution model performance, as ratio of Model over Data vs. pixels, all cameras side by side, over the whole current calibration dataset (since instrument programming update), including 15 calibrations in extrapolation, channels Oa1 to Oa6.

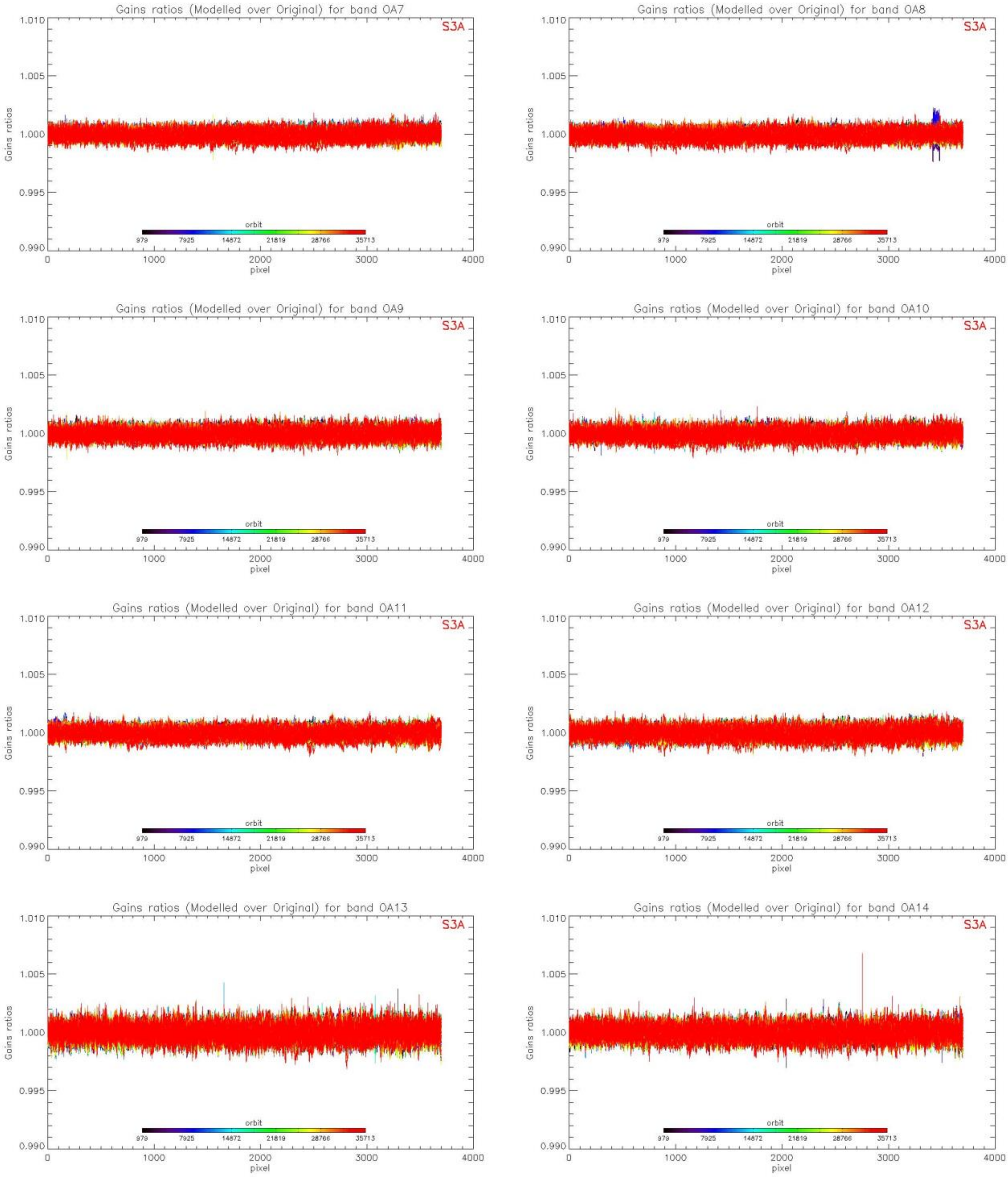

Figure 31: same as Figure 30 for channels Oa7 to Oa14.

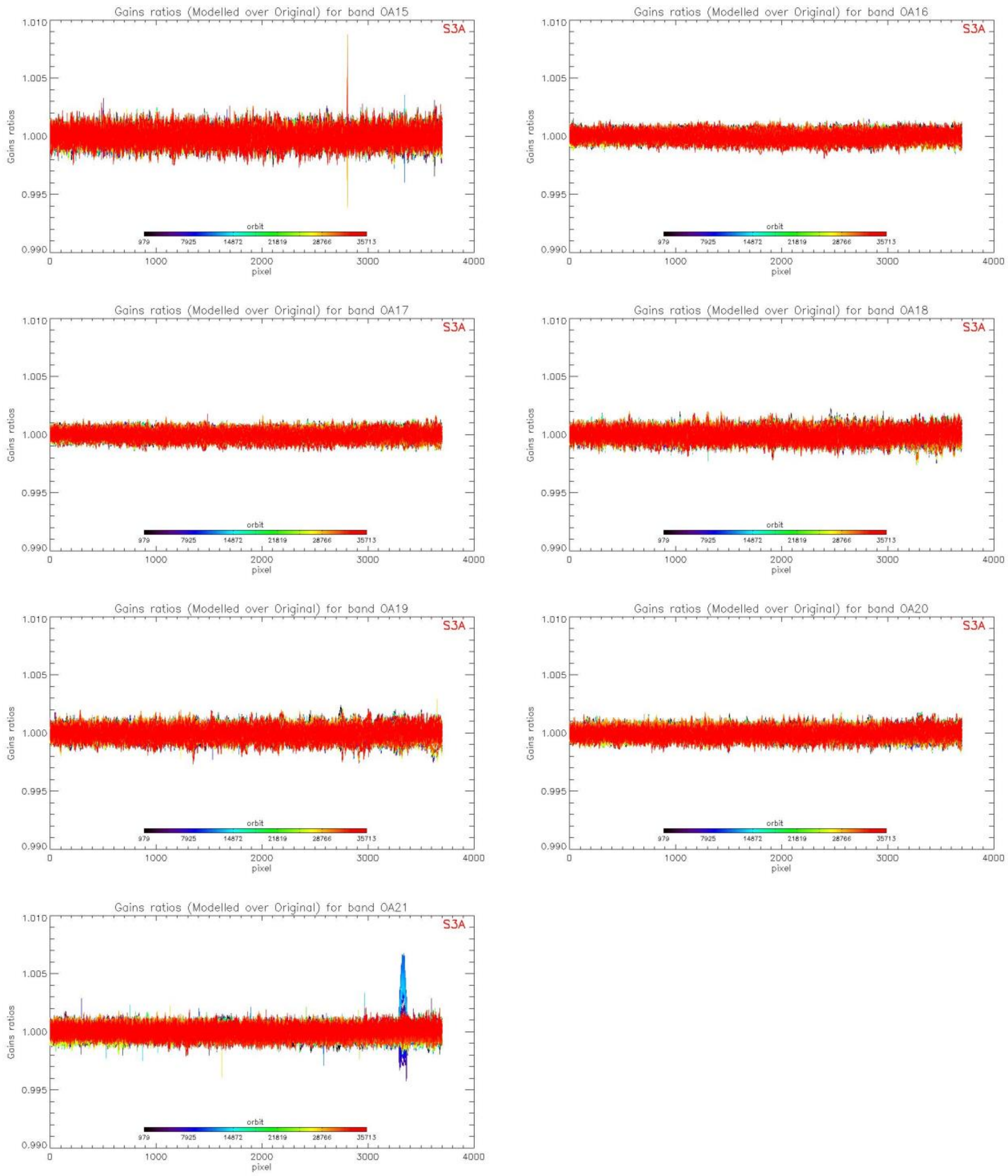

Figure 32: same as Figure 30 for channels Oa15 to Oa21.

2.2.3.2.2 OLCI-B

A new OLCI-B Radiometric Gain Model, has been put in operations at PDGS on 19/07/2022 (Processing Baseline 3.09). This model has been derived on the basis of an extended Radiometric Calibration dataset (from 13/04/2019 to 29/04/2022). It includes the correction of the diffuser ageing for the five bluest bands (Oa1 to Oa5) for which it is clearly measurable. The model performance over the complete dataset (including 15 calibrations in extrapolation over about 8 months) is illustrated in Figure 33. It remains better than 0.12% when averaged over the whole field of view for all bands. A slight drift of the model with respect to the most recent data seems to appear for all bands and a new Radiometric Gain Model has been trained on an extended data set. The previous model, trained on a Radiometric Dataset limited to 16/09/2021, shows a pronounced drift of the model with respect to most recent data, especially for band Oa01 (Figure 34). Comparison of the two figures shows the improvement brought by the updated Model over all the mission.

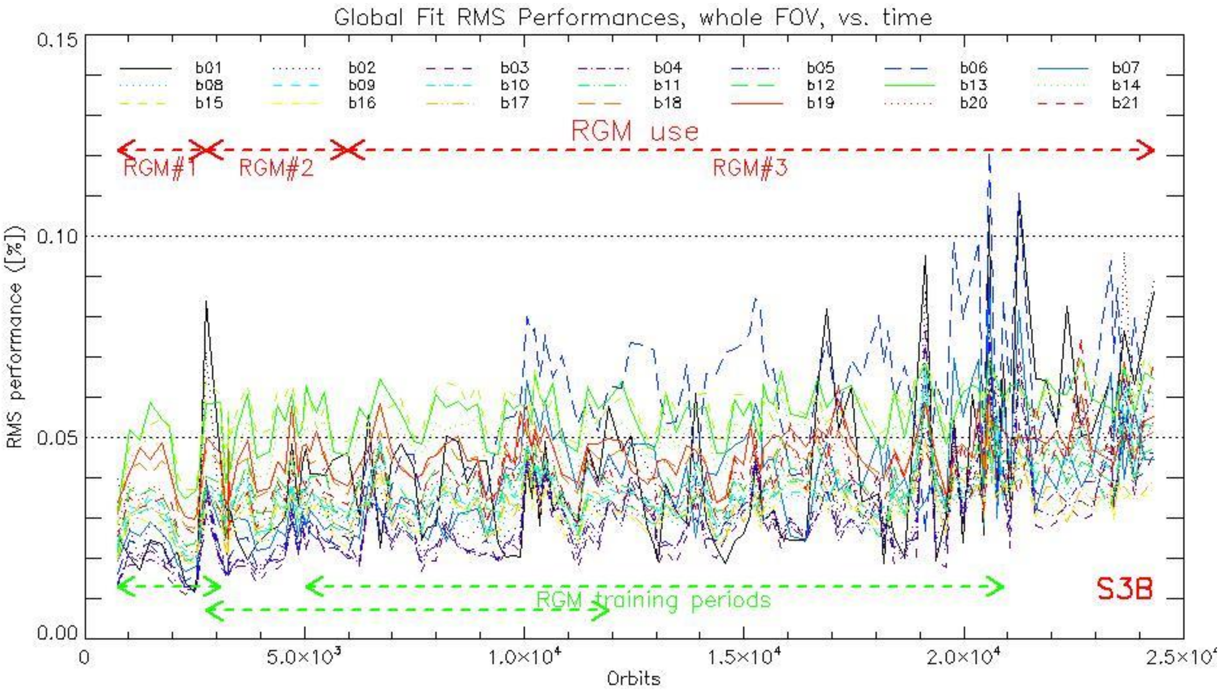

Figure 33: RMS performance of the OLCI-B Gain Model of the current processing baseline as a function of orbit.

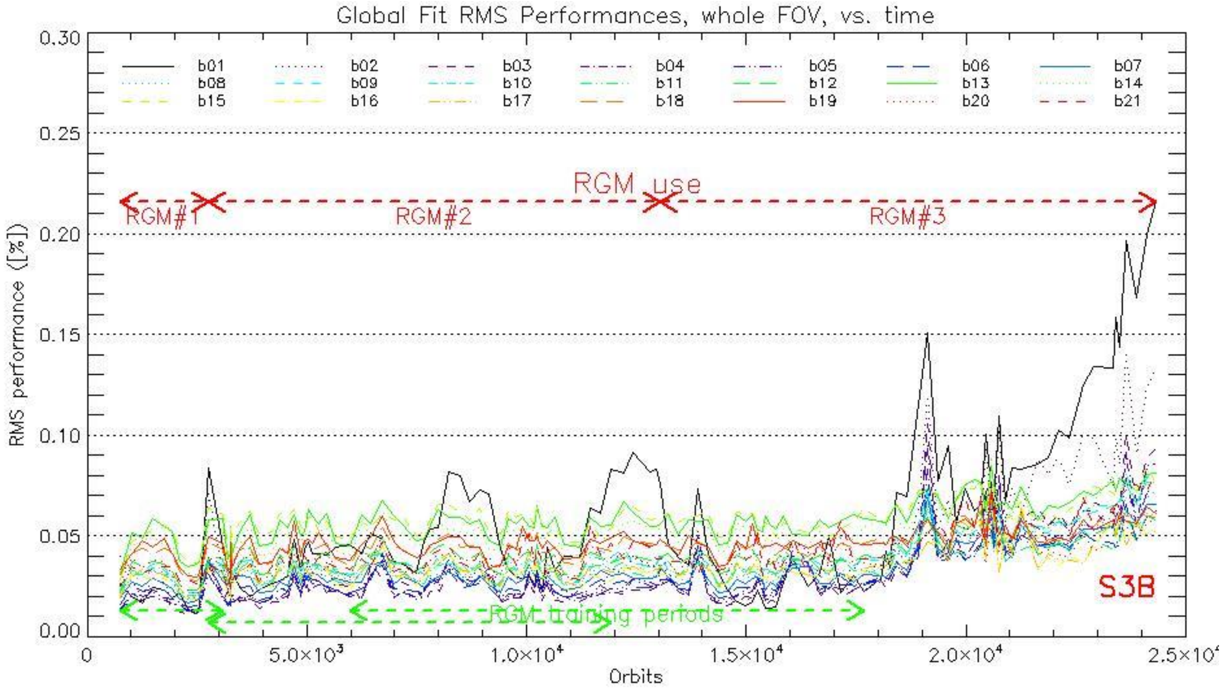

Figure 34: RMS performance of the OLCI-B Gain Model of the previous processing baseline as a function of orbit (please note the different vertical scale with respect to Figure 33).

The overall instrument evolution since channel programming change (18/06/2018) is shown on Figure 35.

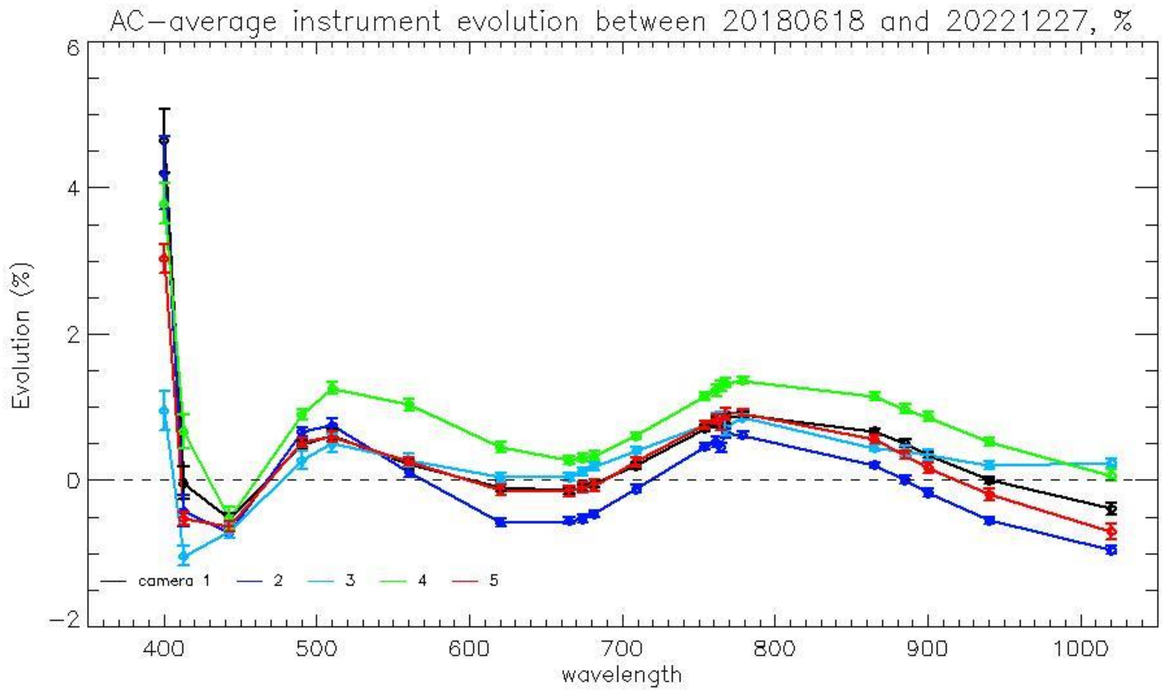

Figure 35: OLCI-B Camera-averaged instrument evolution since channel programming change (18/06/2018) and up to most recent calibration (27/12/2022) versus wavelength.

The overall per camera performance, as a function of wavelength, and at each orbit is shown on Figure 36 as the average and standard deviation of the model over data ratio.

Finally, Figure 37 to Figure 39 show the detail of the model performance, with across-track plots of the model over data ratios at each orbit, one plot for each channel.

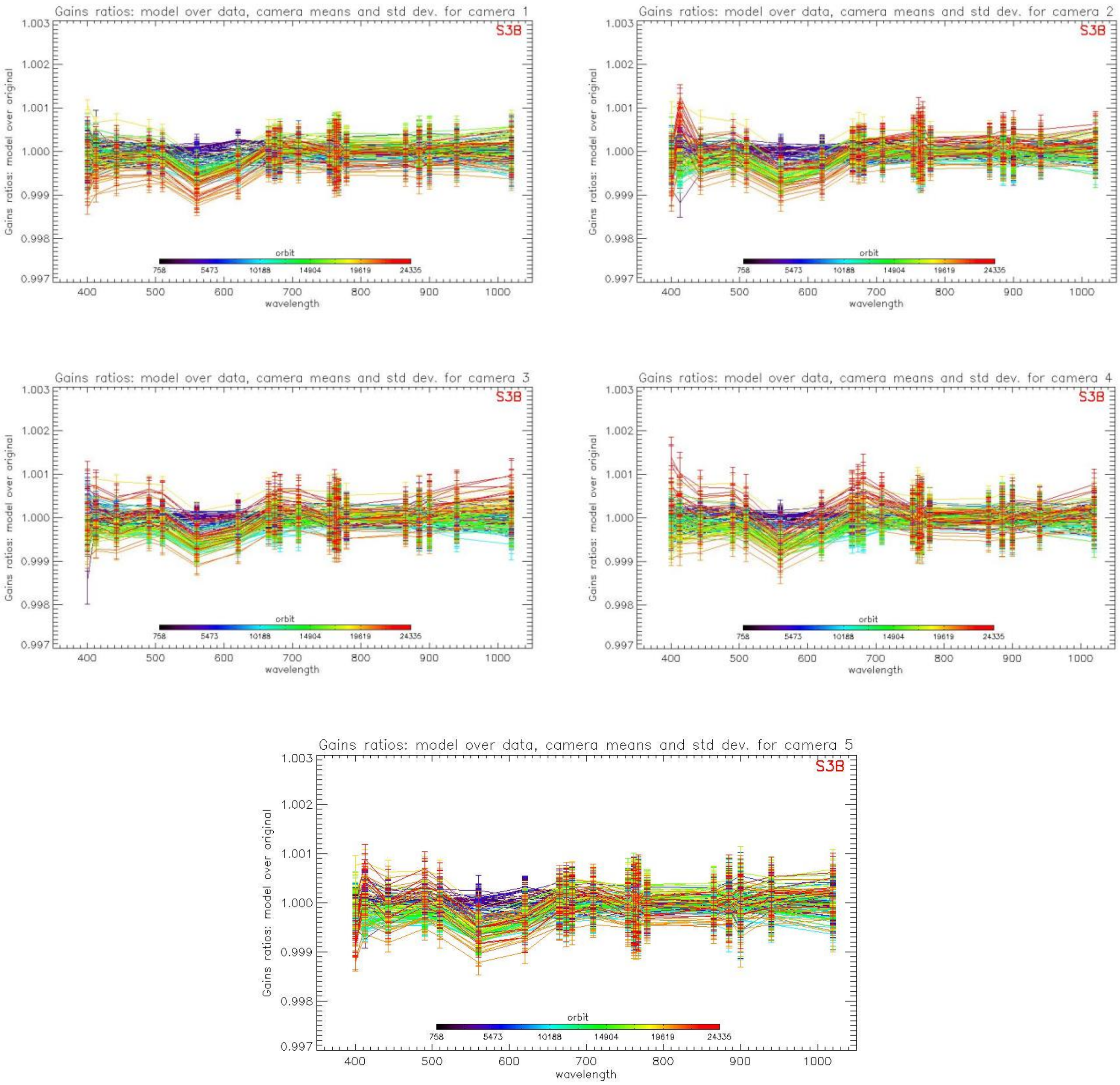

Figure 36: For the 5 cameras: OLCI-B Evolution model performance, as camera-average and standard deviation of ratio of Model over Data vs. wavelength, for each orbit of the test dataset, including 15 calibrations in extrapolation, with a colour code for each calibration from blue (oldest) to red (most recent).

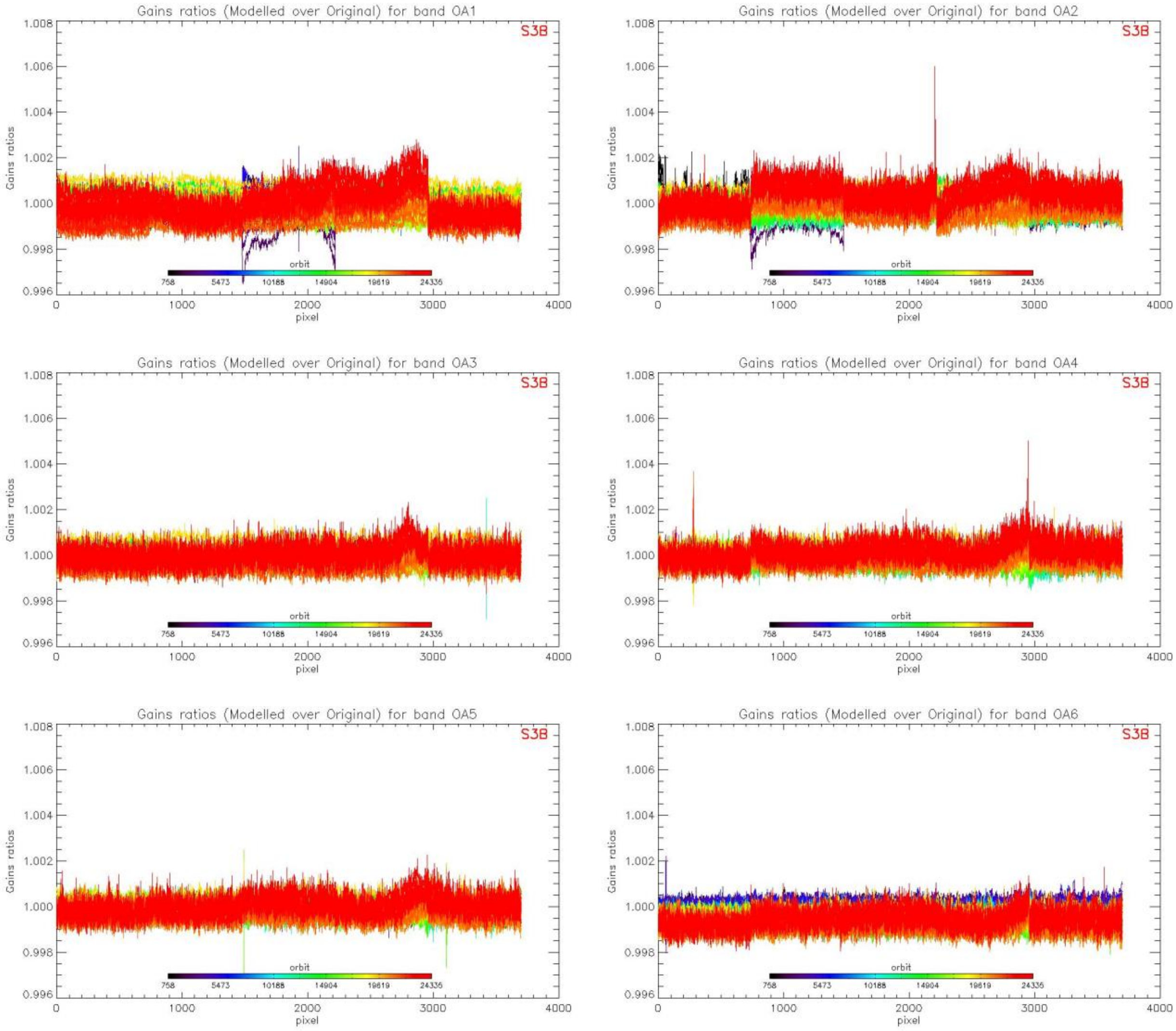

Figure 37: OLCI-B evolution model performance, as ratio of Model over Data vs. pixels, all cameras side by side, over the whole current calibration dataset (since instrument programming update), including 15 calibrations in extrapolation, channels Oa1 to Oa6.

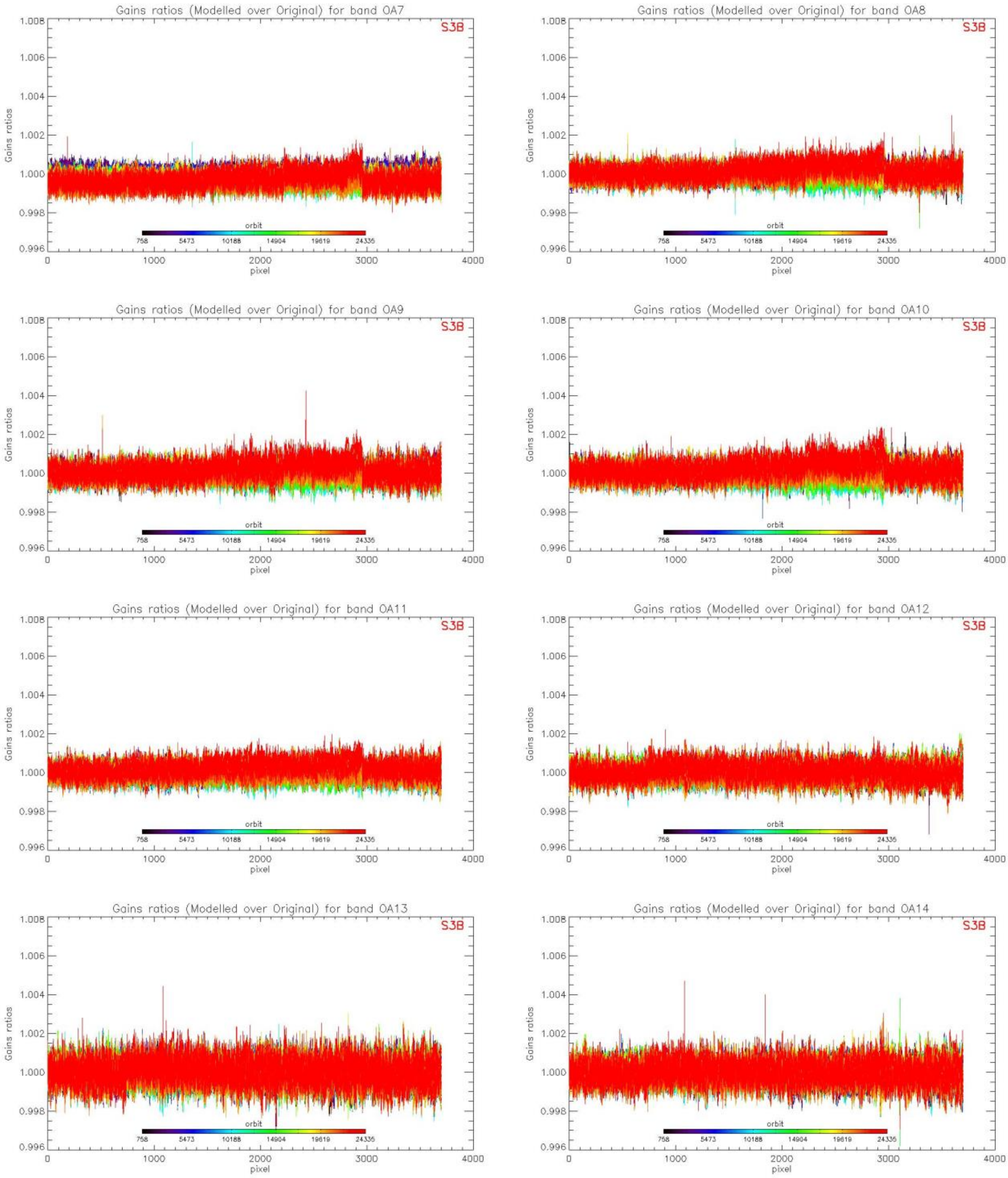

Figure 38: same as Figure 37 for channels Oa7 to Oa14.

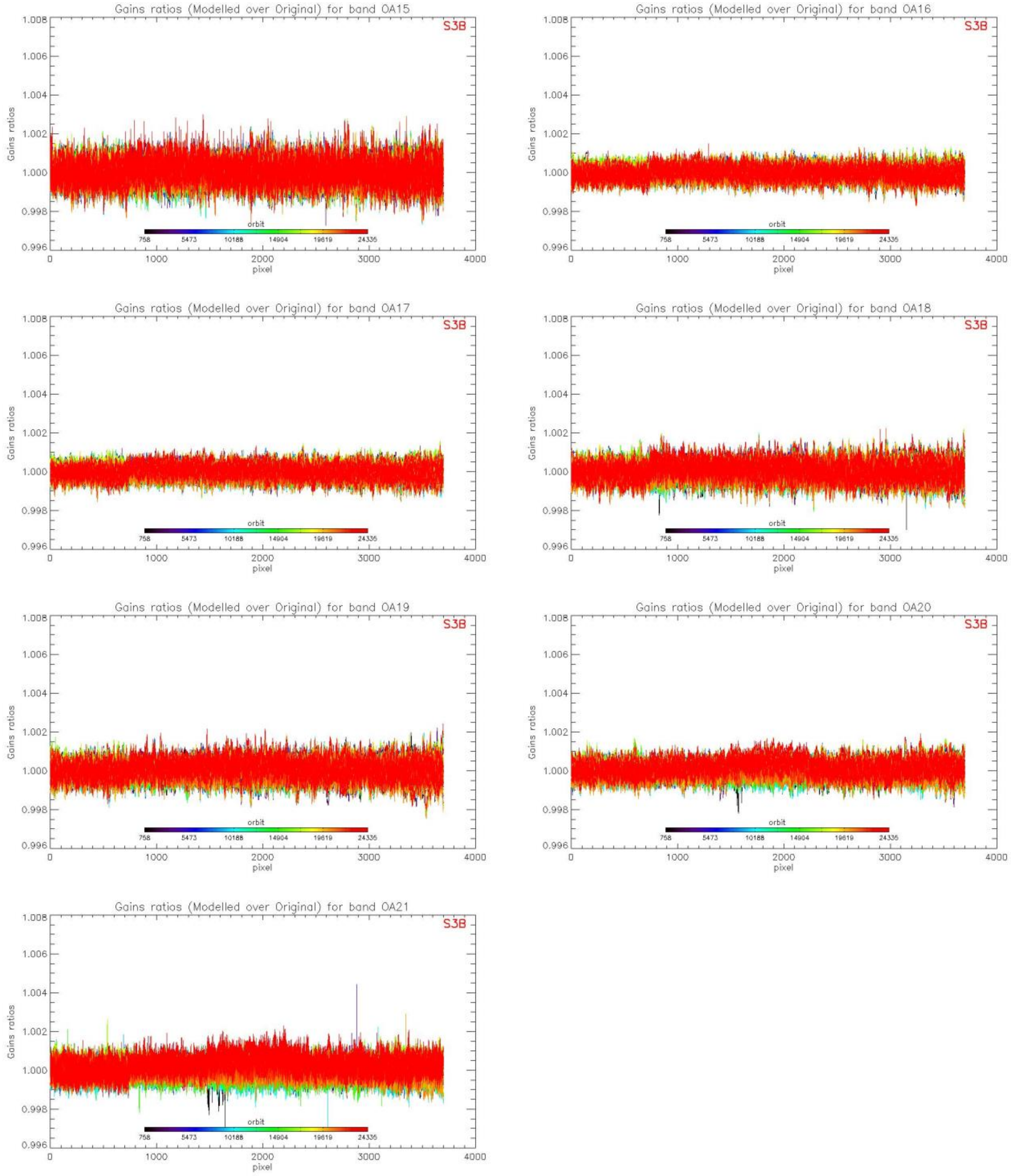

Figure 39: same as for channels Oa15 to Oa21.

2.2.4 Ageing of nominal diffuser [OLCI-L1B-CV-240]

2.2.4.1 OLCI-A

There has been no calibration sequence S05 (reference diffuser) for OLCI-A during the current reported period.

Consequently, the last ageing results presented in November 2022 DQR stay valid.

2.2.4.2 OLCI-B

There has been no calibration sequence S05 (reference diffuser) for OLCI-B during the current reported period.

Consequently, the last ageing results presented in November 2022 DQR stay valid.

2.2.5 Updating of calibration ADF [OLCI-L1B-CV-260]

2.2.5.1 OLCI-A

No CAL_AX ADF has been delivered to PDGS during the report period for OLCI-A.

2.2.5.2 OLCI-B

No CAL_AX ADF has been delivered to PDGS during the report period for OLCI-B.

2.3 Spectral Calibration [OLCI-L1B-CV-400]

2.3.1 OLCI-A

There has been no S02+S03 nor S09 Spectral Calibration for OLCI-A in the reporting period.

Consequently, the last results, presented in October 2022 DQR, stay valid.

2.3.2 OLCI-B

There has been no S02+S03 nor S09 Spectral Calibration for OLCI-B in the reporting period.

Consequently, the last results, presented in October 2022 DQR, stay valid.

2.4 Signal to Noise assessment [OLCI-L1B-CV-620]

2.4.1 SNR from Radiometric calibration data

2.4.1.1 OLCI-A

SNR computed for all calibration data (S01, S04 and S05 sequences) as a function of band number is presented in Figure 40.

SNR computed for all calibration data as a function of orbit number for band Oa01 (the less stable band) is presented in Figure 41.

There is no significant evolution of this parameter during the current reporting period and the ESA requirement is fulfilled for all bands.

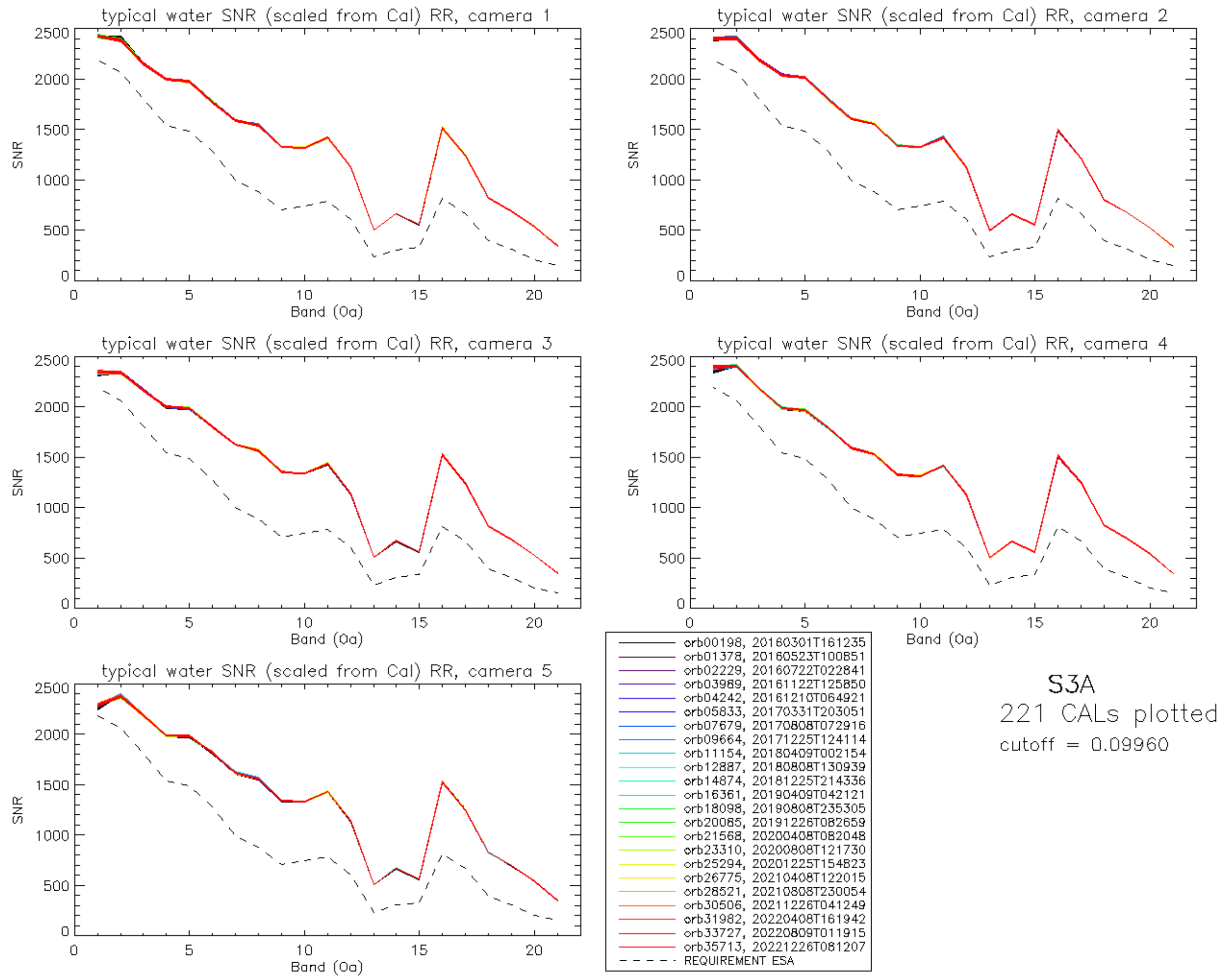

Figure 40: OLCI-A Signal to Noise ratio as a function of the spectral band for the 5 cameras. These results have been computed from radiometric calibration data. All calibrations except first one (orbit 183) are presents with the colours corresponding to the orbit number (see legend). The SNR is very stable with time: the curves for all orbits are almost superimposed. The dashed curve is the ESA requirement.

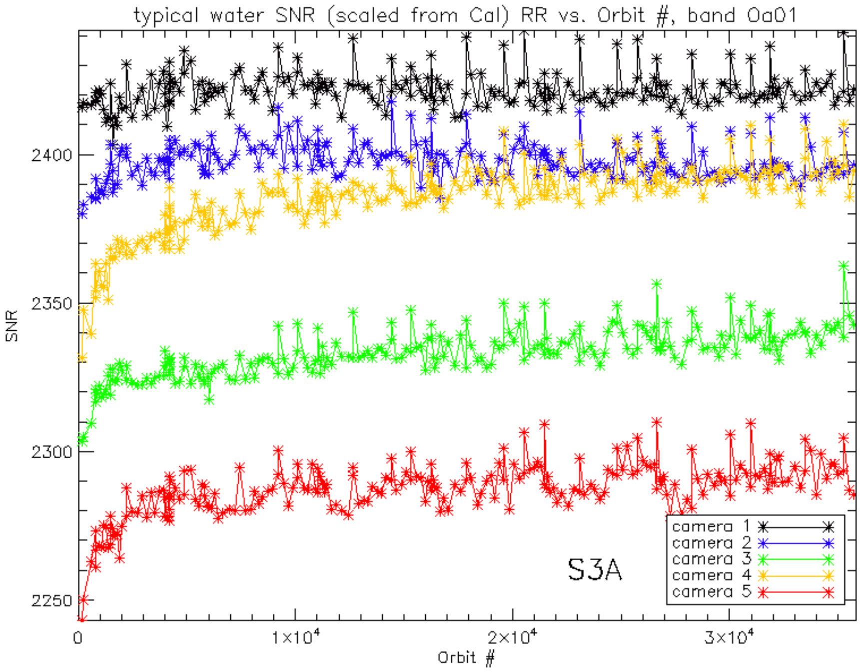

Figure 41: long-term stability of the SNR estimates from Calibration data, example of channel Oa1.

The mission averaged SNR figures are provided in Table 1 below, together with their radiance reference level. According to the OLCI SNR requirements, these figures are valid at these radiance levels and at Reduced Resolution (RR, 1.2 km). They can be scaled to other radiance levels assuming shot noise (CCD sensor noise) is the dominating term, i.e. radiometric noise can be considered Gaussian with its standard deviation varying as the square root of the signal; in other words: $SNR(L) = SNR(L_{ref}) \cdot \sqrt{\frac{L}{L_{ref}}}$. Following the same assumption, values at Full Resolution (300m) can be derived from RR ones as 4 times smaller.

Table 1: OLCI-A SNR figures as derived from Radiometric Calibration data. Figures are given for each camera (time average and standard deviation), and for the whole instrument. The requirement and its reference radiance level are recalled (in mW.sr^{-1}.m^{-2}.nm^{-1}).

	L_{ref}	SNR	C1		C2		C3		C4		C5		All	
nm	LU	RQT	avg	*std*	avg	*std*	avg	*std*	avg	*std*	avg	*std*	avg	*std*
400.000	63.0	2188	2421	6.1	2398	6.2	2333	8.1	2384	12.0	2287	9.1	2365	6.9
412.000	74.1	2061	2386	9.4	2403	7.4	2339	5.0	2401	5.0	2379	9.2	2382	5.8
442.000	65.6	1811	2157	6.0	2196	6.1	2163	5.0	2185	4.1	2193	5.9	2179	4.2
490.000	51.2	1541	1999	4.8	2036	4.7	1998	4.3	1984	4.3	1988	4.3	2001	3.1
510.000	44.4	1488	1979	5.3	2014	4.9	1986	4.5	1967	4.3	1985	4.2	1986	3.4
560.000	31.5	1280	1775	4.6	1802	4.1	1803	4.7	1794	3.8	1819	3.3	1799	3.0
620.000	21.1	997	1591	4.1	1608	4.3	1624	3.1	1593	3.2	1615	3.4	1606	2.6
665.000	16.4	883	1545	4.2	1557	4.5	1566	3.9	1533	3.5	1561	3.6	1552	3.0
674.000	15.7	707	1328	3.4	1336	3.7	1350	2.8	1323	3.3	1343	3.4	1336	2.4
681.000	15.1	745	1319	3.5	1325	3.3	1338	2.6	1314	2.5	1334	3.3	1326	2.1
709.000	12.7	785	1420	4.1	1420	4.0	1435	3.3	1414	3.5	1431	3.0	1424	2.7
754.000	10.3	605	1127	3.0	1121	2.8	1136	3.1	1125	2.5	1139	2.7	1130	2.2
761.000	6.1	232	502	1.1	498	1.1	505	1.1	501	1.1	508	1.3	503	0.8
764.000	7.1	305	663	1.5	658	1.5	668	2.0	662	1.5	670	2.0	664	1.3
768.000	7.6	330	558	1.4	554	1.3	563	1.3	557	1.3	564	1.3	559	1.0
779.000	9.2	812	1516	4.6	1498	4.4	1527	5.1	1512	4.9	1527	4.8	1516	4.0
865.000	6.2	666	1243	3.5	1213	3.4	1239	3.8	1247	3.5	1250	2.8	1239	2.7
885.000	6.0	395	823	1.7	801	1.6	814	1.9	824	1.5	831	1.6	819	1.1

	L_{ref}	SNR	C1		C2		C3		C4		C5		All	
900.000	4.7	308	691	1.6	673	1.3	683	1.6	693	1.5	698	1.4	688	1.0
940.000	2.4	203	534	1.2	522	1.2	525	1.0	539	1.1	542	1.3	532	0.7
1020.000	3.9	152	345	0.9	337	0.8	348	0.7	345	0.8	351	0.8	345	0.5

2.4.1.2 OLCI-B

SNR computed for all OLCI-B calibration data (S01, S04 (but not the dark-only S04) and S05 sequences) as a function of band number is presented in Figure 42.

SNR computed for all OLCI-B calibration data as a function of orbit number for band Oa01 (the less stable band) is presented in Figure 43.

As for OLCI-A the SNR is very stable in time. There is no significant evolution of this parameter during the current reporting and the ESA requirement is fulfilled for all bands.

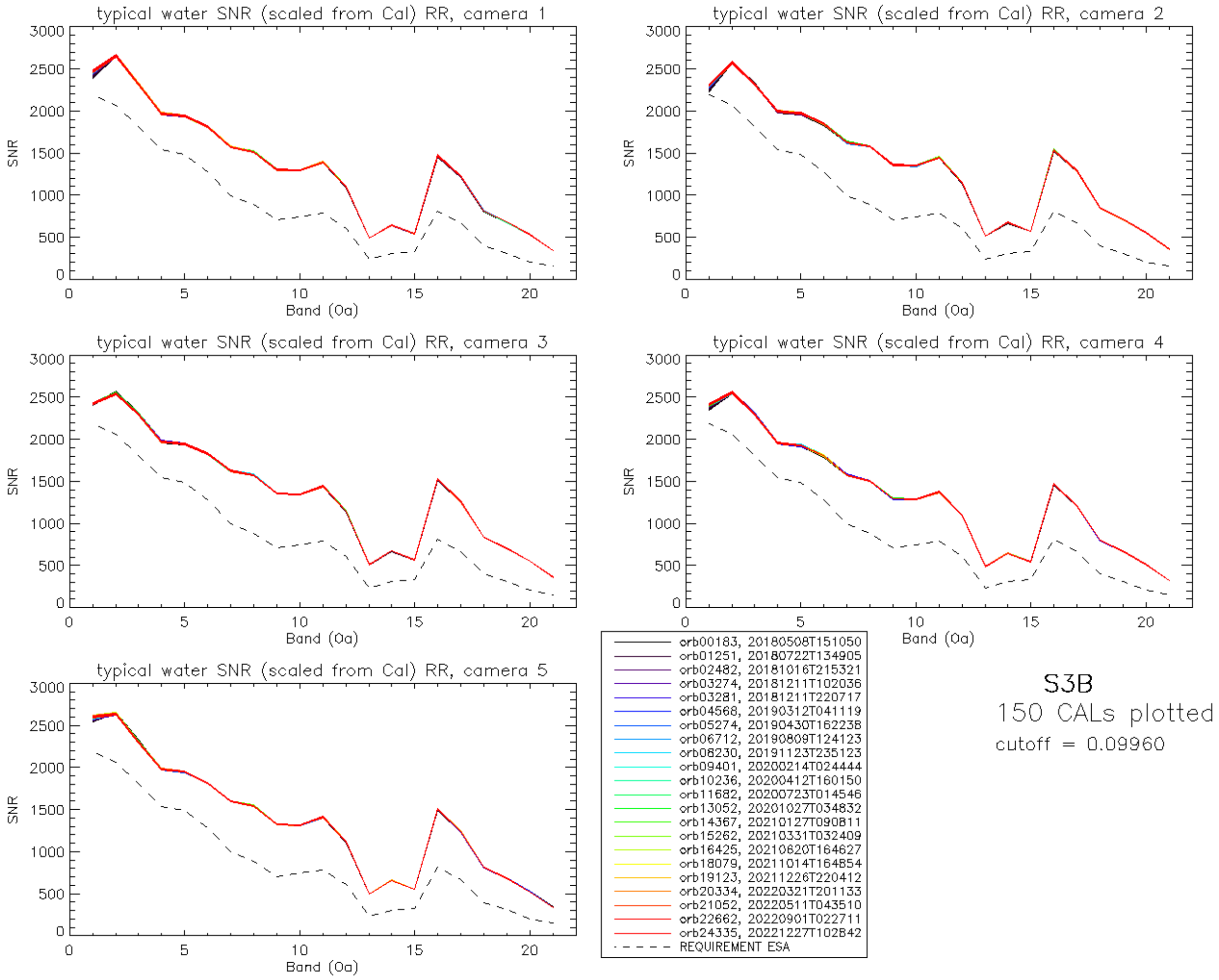

Figure 42: OLCI-B Signal to Noise ratio as a function of the spectral band for the 5 cameras. These results have been computed from radiometric calibration data. All calibrations except first one (orbit 167) are presents with the colours corresponding to the orbit number (see legend). The SNR is very stable with time: the curves for all orbits are almost superimposed. The dashed curve is the ESA requirement.

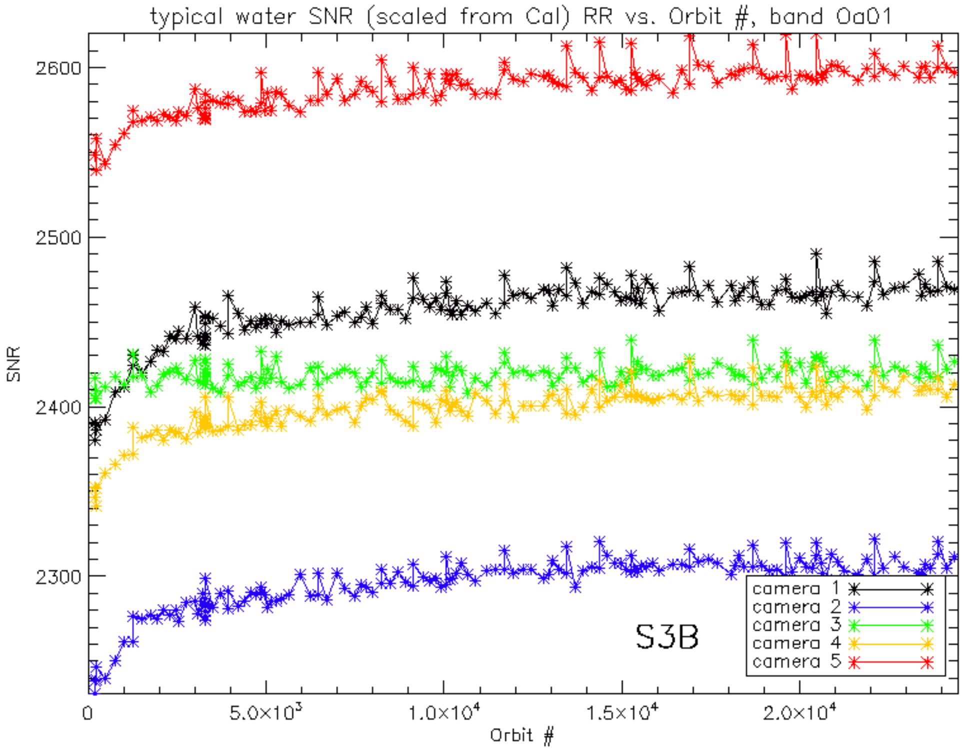

Figure 43: long-term stability of the OLCI-B SNR estimates from Calibration data, example of channel Oa1.

Table 2: OLCI-B SNR figures as derived from Radiometric Calibration data. Figures are given for each camera (time average and standard deviation), and for the whole instrument. The requirement and its reference radiance level are recalled (in mW.sr^{-1}.m^{-2}.nm^{-1}).

	L_{ref}	SNR	C1		C2		C3		C4		C5		All	
nm	LU	RQT	avg	*std*	avg	*std*	avg	*std*	avg	*std*	avg	*std*	avg	*std*
400.000	63.0	2188	2456	18.7	2296	16.5	2419	6.4	2399	13.9	2587	14.1	2431	13.0
412.000	74.1	2061	2654	7.0	2569	6.4	2543	8.5	2550	6.2	2637	7.6	2591	5.6
442.000	65.6	1811	2324	6.6	2316	6.1	2299	6.7	2302	7.0	2308	6.6	2310	5.6
490.000	51.2	1541	1966	4.9	1990	5.6	1971	5.2	1952	4.7	1979	4.5	1972	3.9
510.000	44.4	1488	1939	4.8	1968	6.0	1943	4.9	1924	5.0	1952	4.8	1945	4.0
560.000	31.5	1280	1813	4.7	1848	4.9	1829	4.6	1804	4.6	1817	4.0	1822	3.6
620.000	21.1	997	1572	4.3	1626	4.6	1624	3.8	1576	3.7	1601	3.5	1600	2.9
665.000	16.4	883	1513	4.2	1578	3.8	1573	3.7	1501	3.0	1546	3.7	1542	2.8
674.000	15.7	707	1300	3.9	1358	3.5	1353	3.2	1292	2.6	1328	2.9	1326	2.3
681.000	15.1	745	1293	3.5	1347	3.2	1343	2.9	1285	2.7	1316	2.9	1317	2.1
709.000	12.7	785	1390	3.9	1447	4.0	1443	4.0	1373	2.9	1412	3.6	1413	2.9
754.000	10.3	605	1096	3.6	1143	3.6	1142	3.3	1089	2.8	1116	3.2	1117	2.8
761.000	6.1	232	488	1.2	509	1.2	509	1.4	485	1.1	498	1.4	498	1.0
764.000	7.1	305	643	1.6	672	2.0	672	1.8	641	1.8	658	1.8	657	1.5
768.000	7.6	330	541	1.4	568	1.4	564	1.3	541	1.4	555	1.5	554	1.0
779.000	9.2	812	1467	4.2	1535	4.6	1527	5.3	1467	3.9	1507	4.2	1501	3.8
865.000	6.2	666	1221	3.5	1287	3.7	1258	3.6	1206	3.6	1238	2.9	1242	2.8
885.000	6.0	395	808	2.2	847	1.8	834	2.0	799	1.7	815	2.0	821	1.5
900.000	4.7	308	679	1.4	714	1.9	704	1.7	670	1.5	683	1.5	690	1.2
940.000	2.4	203	527	1.2	549	1.5	551	1.3	510	1.1	522	1.3	532	0.9
1020.000	3.9	152	336	0.8	358	1.2	358	0.8	318	0.7	338	0.9	342	0.6

2.5 Geometric Calibration/Validation

2.5.1 OLCI-A

OLCI-A georeferencing performance is compliant since the introduction of MPC Geometric Calibration, put in production on the 14th of March 2018. It has however significantly improved after its last full revision of GCMs (Geometric Calibration Models, or platform to instrument alignment quaternions) and IPPVMs (Instrument Pixels Pointing Vectors) both derived using the GeoCal Tool and put in production on 30/07/2019.

The following figures (Figure 44 to Figure 49) show time series of the overall RMS performance (requirement criterion) and of the across-track and along-track biases for each camera. New plots (Figure 50 and Figure 51) introduce monitoring of the performance homogeneity within the field of view: georeferencing errors in each direction at camera transitions (difference between last pixel of camera N and first pixel of camera N+1) and within a given camera (maximum bias minus minimum inside each camera). The performance improvement since the 30/07/2019 is significant on most figures: the global RMS value decreases form around 0.35 to about 0.2 (Figure 44), the across-track biases decrease significantly for all cameras (Figure 45 to Figure 49), the along-track bias reduces for at least camera 3 (Figure 47) and the field of view homogeneity improves drastically (Figure 50 and Figure 51, but also reduction of the dispersion – distance between the ± 1 sigma lines – in Figure 45 to Figure 49).

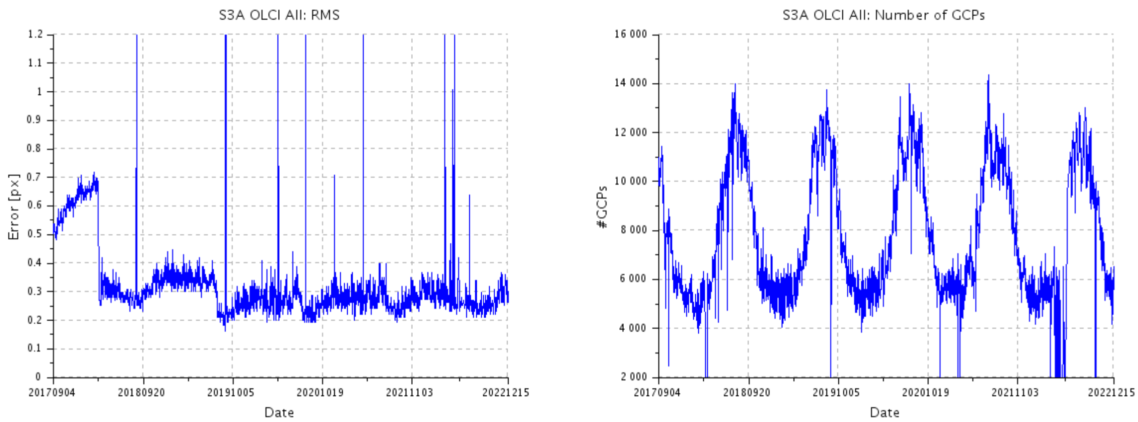

Figure 44: overall OLCI-A georeferencing RMS performance time series (left) and number of validated control points corresponding to the performance time series (right) over the whole monitoring period

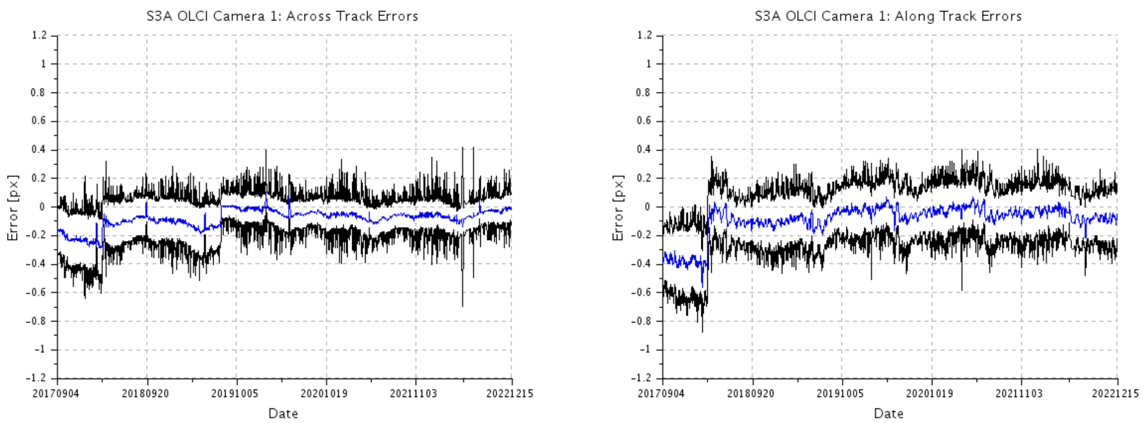

Figure 45: across-track (left) and along-track (right) OLCI-A georeferencing biases time series for Camera 1. Blue line is the average, black lines are average plus and minus 1 sigma.

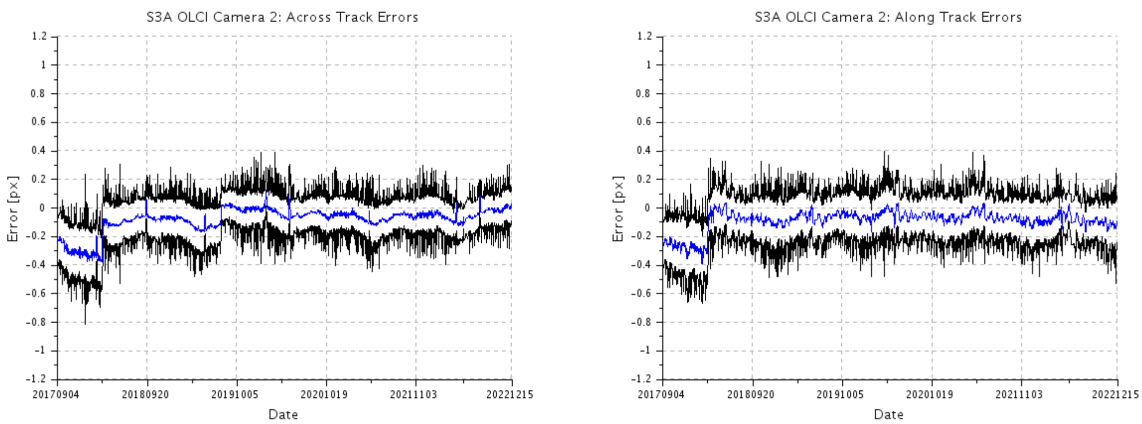

Figure 46: same as Figure 45 for Camera 2.

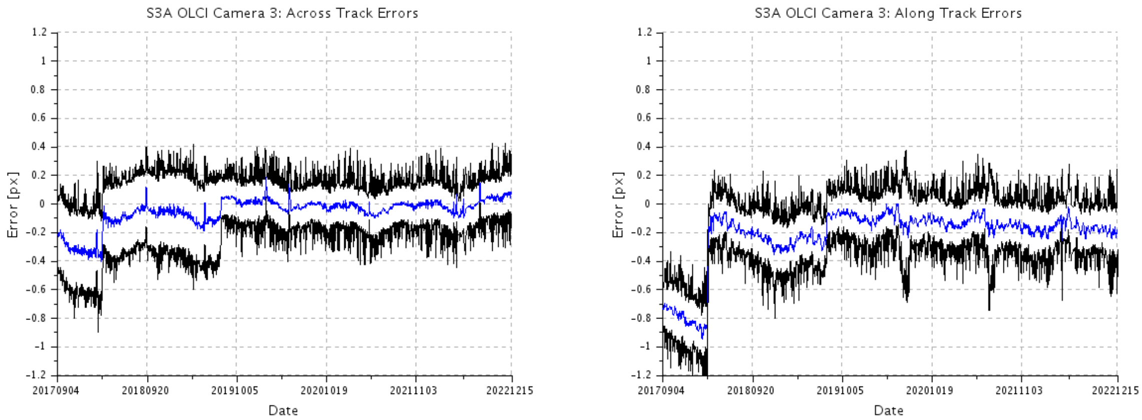

Figure 47: same as Figure 45 for Camera 3.

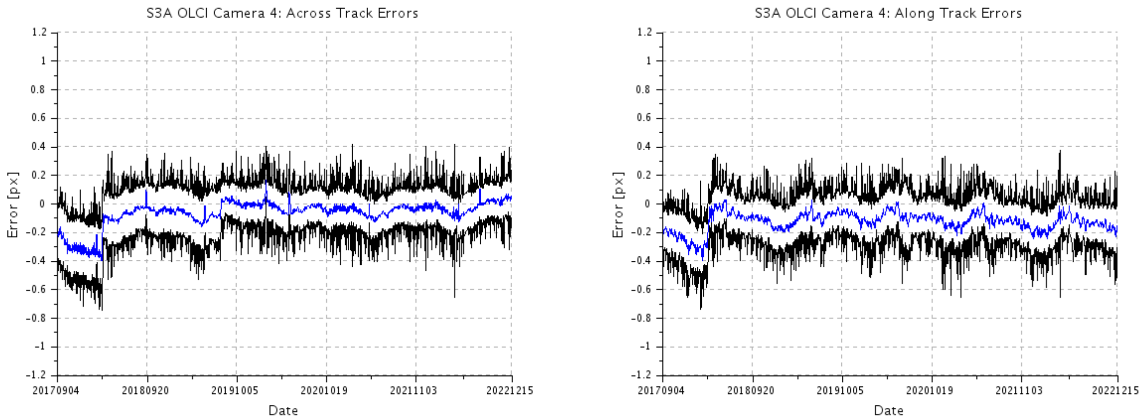

Figure 48: same as Figure 45 for Camera 4.

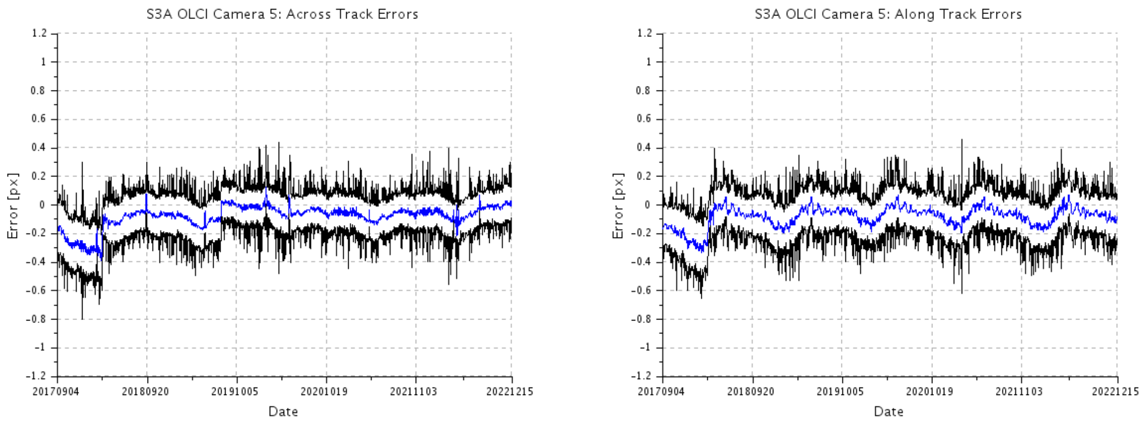

Figure 49: same as Figure 45 for Camera 5.

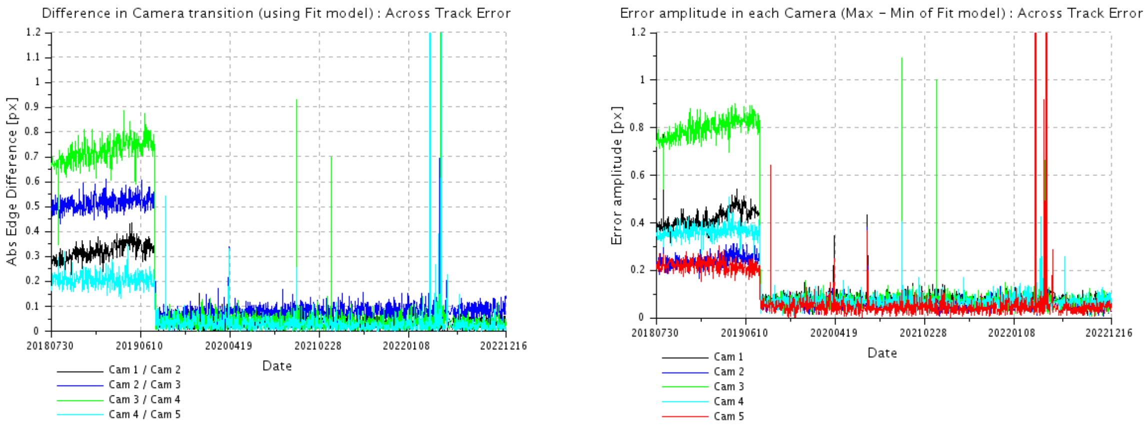

Figure 50: OLCI-A spatial across-track misregistration at each camera transition (left) and maximum amplitude of the across-track error within each camera (left).

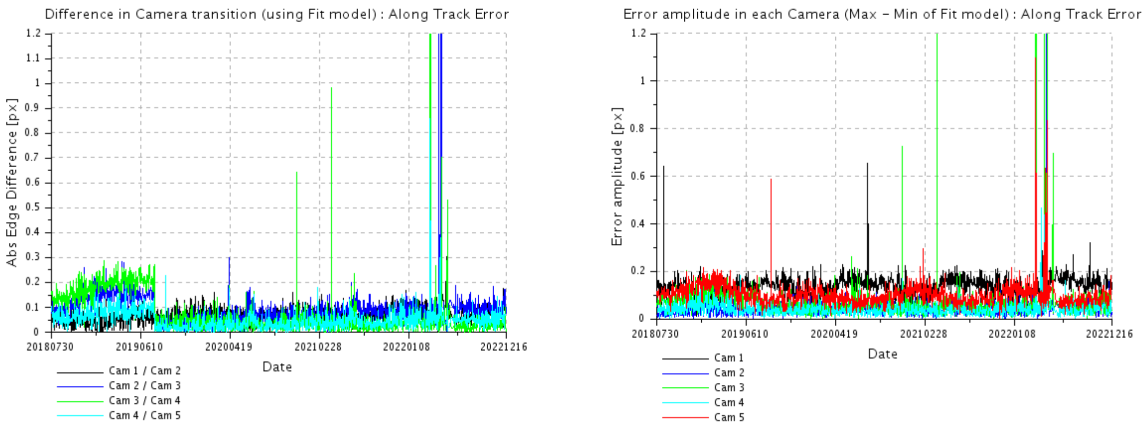

Figure 51: OLCI-A spatial along-track misregistration at each camera transition (left) and maximum amplitude of the along-track error within each camera (left).

2.5.2 OLCI-B

Georeferencing performance of OLCI-B improved significantly with the fourth geometric calibration introduced the 30/07/2019. However, the instrument pointing is still evolving, in particular for camera 2 (Figure 58) and a new geometric calibration has been done and introduced in the processing chain on the 16th of April 2020. Its impact is significant on the along-track biases of all cameras (Figure 53 to Figure 57), but also on the continuity at camera interfaces (Figure 58, left) and on intra-camera homogeneity (Figure 58, right). Since then, further adjustments to the geometric calibration have been introduced, mainly to correct the along-track drifts. The most recent was put in production on 29/07/2021and its effect can be seen e.g. on left graphs of Figure 54, Figure 55 and Figure 57 (across-track biases of cameras 2, 3 & 5).

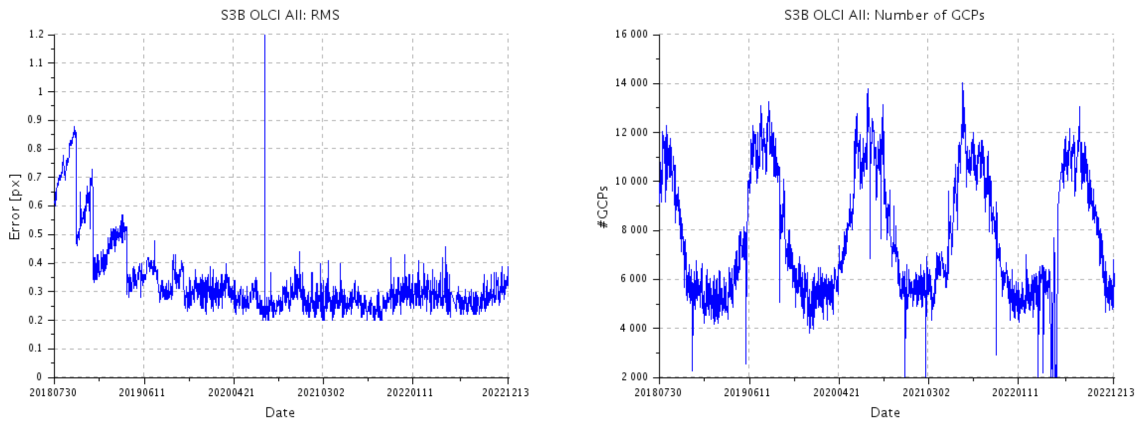

Figure 52: overall OLCI-B georeferencing RMS performance time series over the whole monitoring period (left) and corresponding number of validated control points (right)

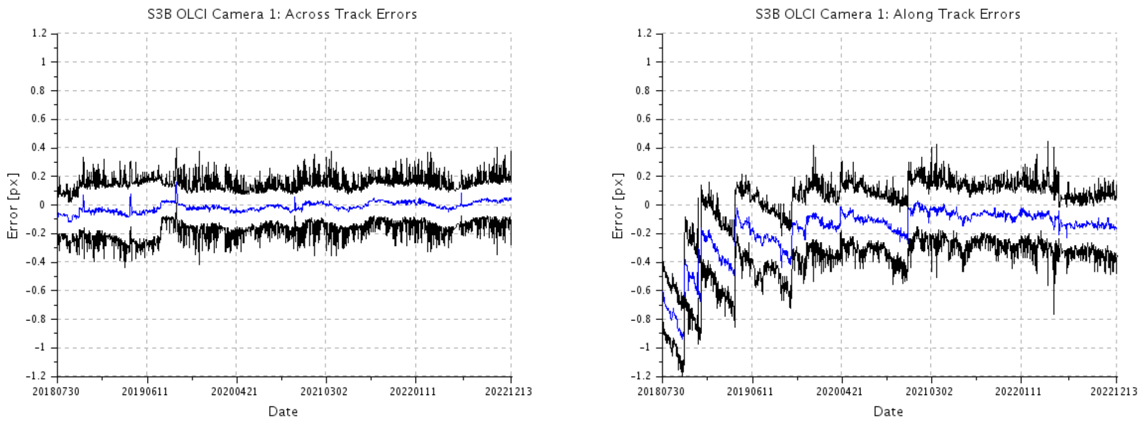

Figure 53: across-track (left) and along-track (right) OLCI-B georeferencing biases time series for Camera 1.

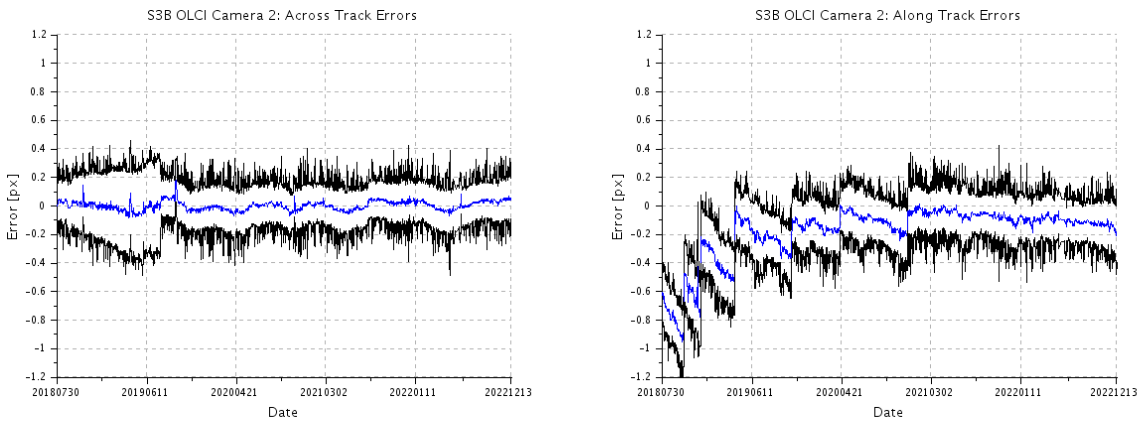

Figure 54: same as Figure 53 for Camera 2.

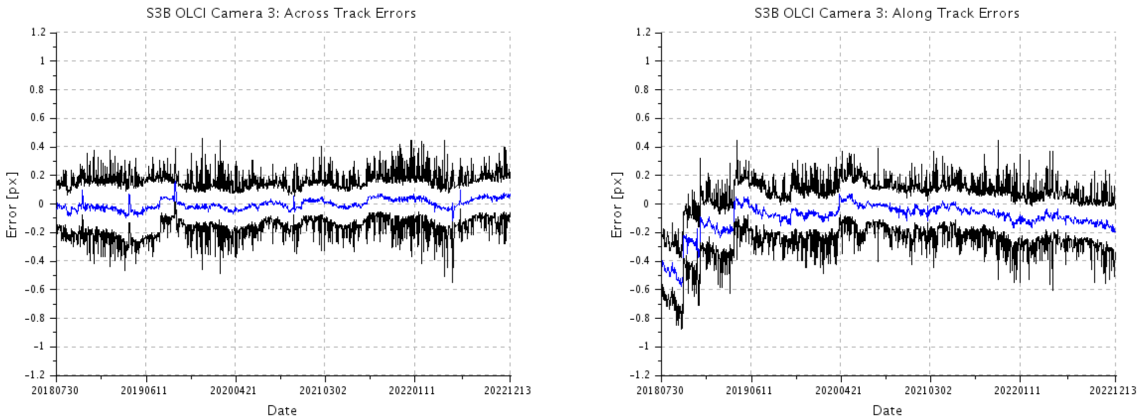

Figure 55: same as Figure 53 for Camera 3.

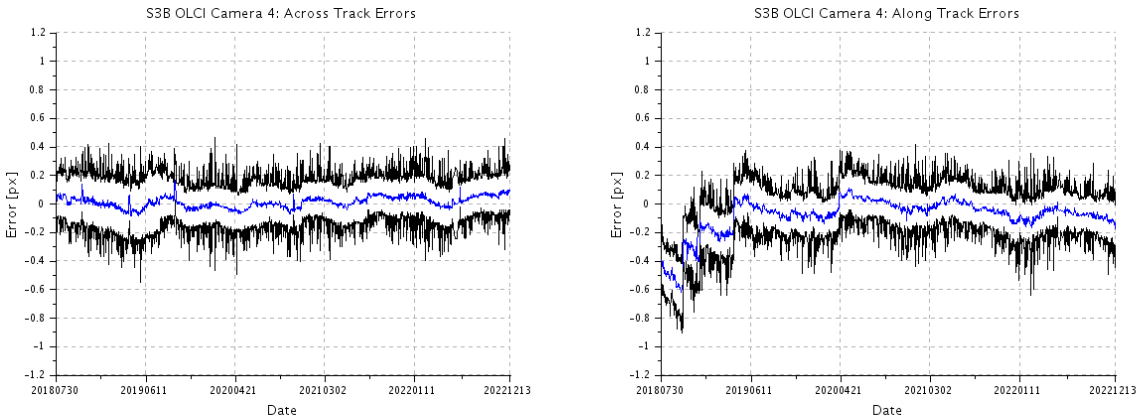

Figure 56: same as Figure 53 for Camera 4.

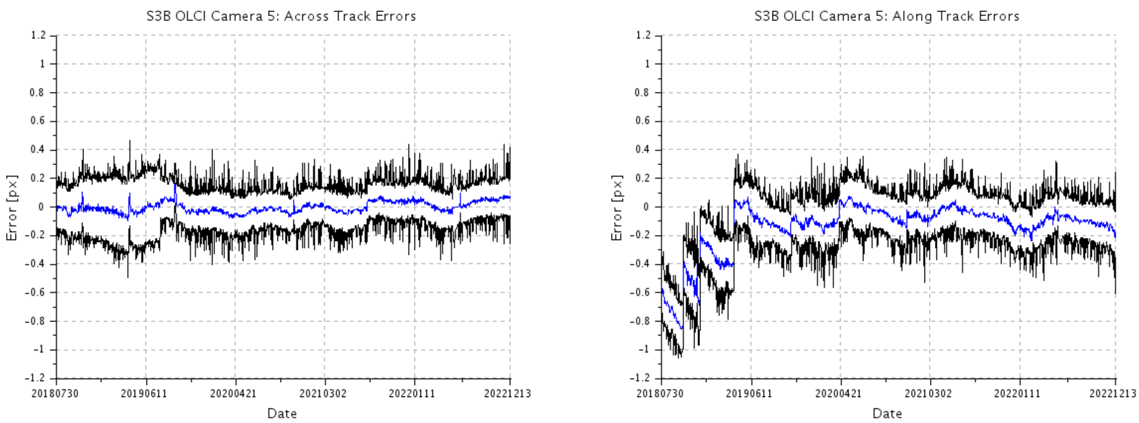

Figure 57: same as Figure 53 for Camera 5.

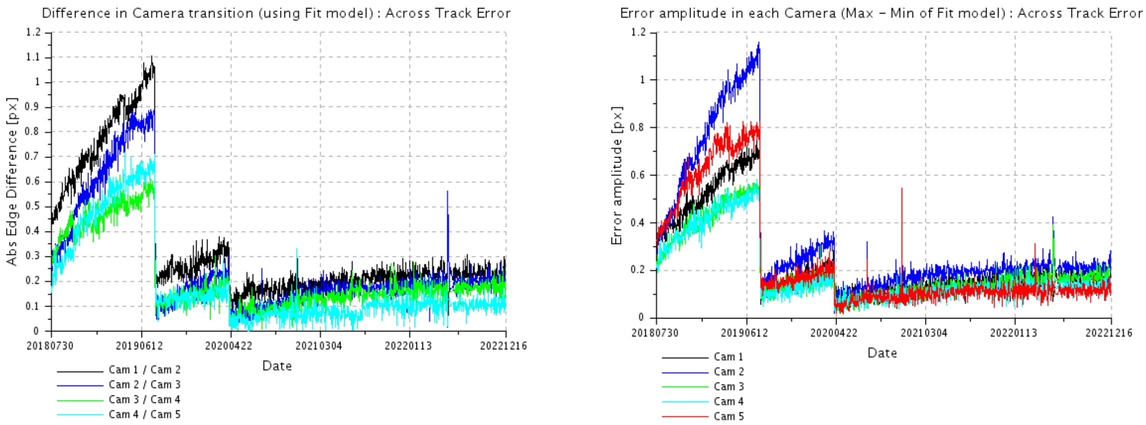

Figure 58: OLCI-B spatial across-track misregistration at each camera transition (left) and maximum amplitude of the across-track error within each camera (left).

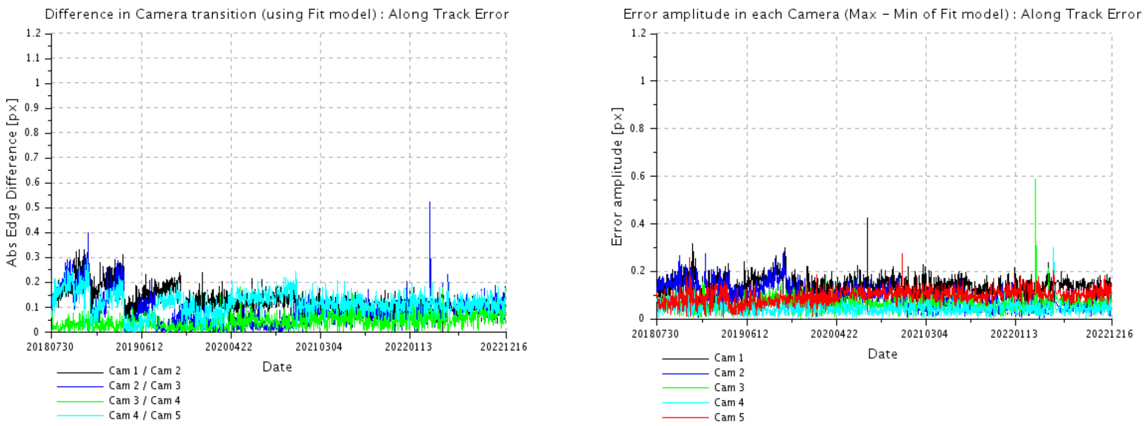

Figure 59: OLCI-B spatial along-track misregistration at each camera transition (left) and maximum amplitude of the along-track error within each camera (left).

3 OLCI Level 1 Product validation

3.1 [OLCI-L1B-CV-300], [OLCI-L1B-CV-310] – Radiometric Validation

3.1.1 S3ETRAC Service

Activities done

The S3ETRAC service extracts OLCI L1 RR and SLSTR L1 RBT data and computes associated statistics over 49 sites corresponding to different surface types (desert, snow, ocean maximizing Rayleigh signal, ocean maximizing sunglint scattering and deep convective clouds). The S3ETRAC products are used for the assessment and monitoring of the L1 radiometry (optical channels) by the ESLs.

All details about the S3ETRAC/OLCI and S3ETRAC/SLSTR statistics are provided on the S3ETRAC website http://s3etrac.acri.fr/index.php?action=generalstatistics.

- Number of OLCI products processed by the S3ETRAC service
- Statistics per type of target (DESERT, SNOW, RAYLEIGH, SUNGLINT and DCC)
- Statistics per sites
- Statistics on the number of records

For illustration, we provide below statistics on the number of S3ETRAC/OLCI records generated per type of targets (DESERT, SNOW, RAYLEIGH, SUNGLINT and DCC) for both OLCI-A (Figure 60) and OLCI-B (Figure 61).

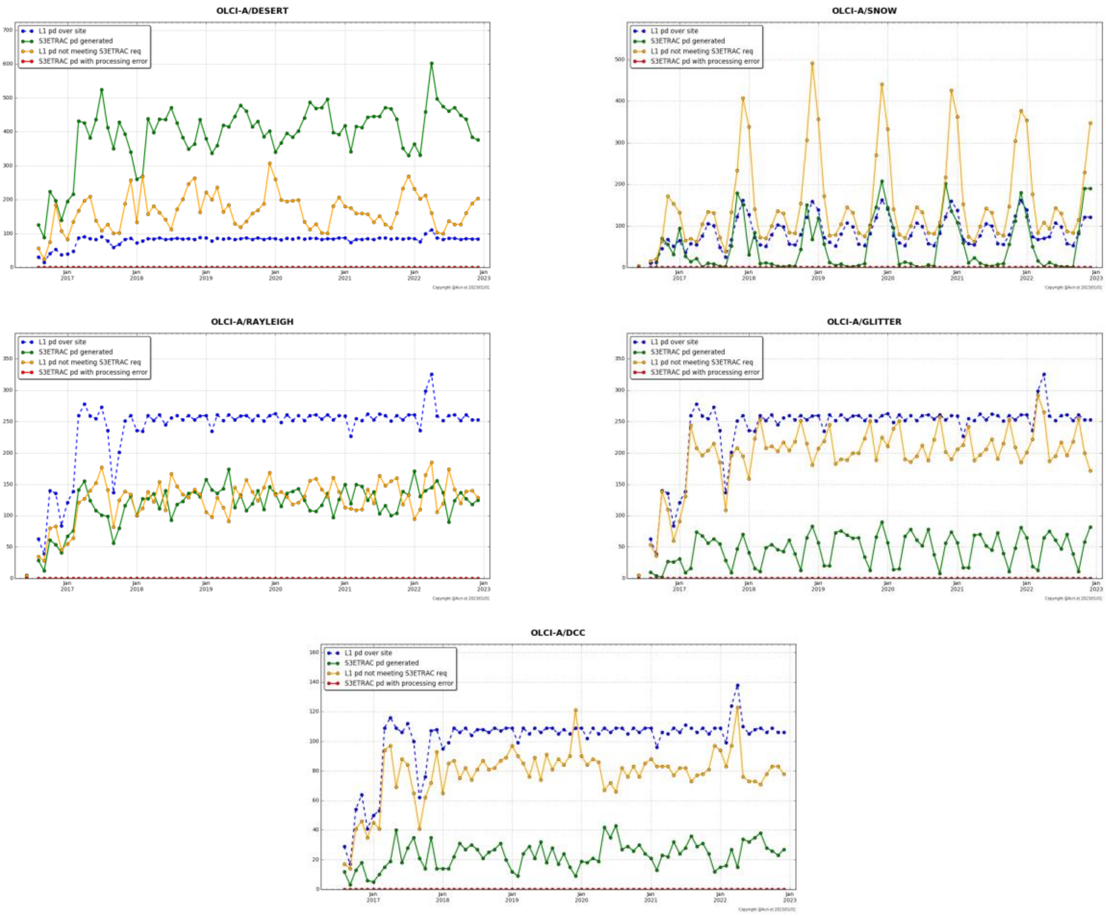

Figure 60: summary of S3ETRAC products generation for OLCI-A (number of OLCI-A L1 products Ingested, blue – number of S3ETRAC extracted products generated, green – number of S3ETRAC runs without generation of output product (data not meeting selection requirements), yellow – number of runs ending in error, red, one plot per site type).

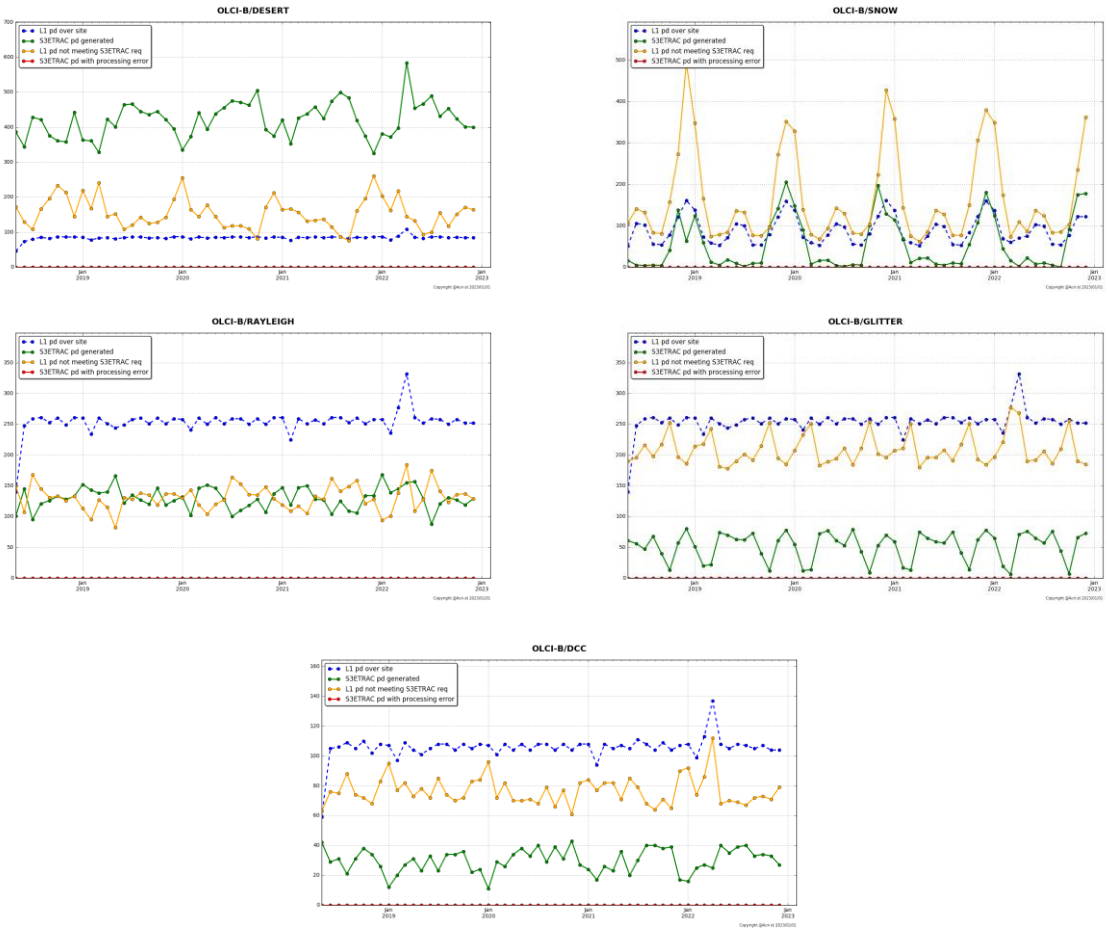

Figure 61: summary of S3ETRAC products generation for OLCI-B (number of OLCI-B L1 products Ingested, yellow – number of S3ETRAC extracted products generated, blue – number of S3ETRAC runs without generation of output product (data not meeting selection requirements), green – number of runs ending in error, red, one plot per site type).

3.1.2 Radiometric validation with DIMITRI

OLCI-A and OLCI-B L1B radiometry verification as follow:

- The verification is performed over Ocean-sites and over Desert-sites **until the 30th December 2022.**
- All results from OLCI-A and OLCI-B over Rayleigh, Glint and PICS are consistent with the previous cycle over the used CalVal sites.
- Good stability of both sensors OLCI-A and OLCI-B could be observed, nevertheless the time-series average shows higher reflectance from OLCI-A.
- Bands with high gaseous absorption are excluded.

Verification and Validation over PICS

1. The ingestion of all the available L1B-LN1-NT products from OLCI-A and OLCI-B over the 6 desert CalVal-sites (Algeria3 & 5, Libya 1 & 4 and Mauritania 1 & 2) has been performed until the **30th December 2022**.
2. The results are consistent over all the six used PICS sites (Figure 62 and Figure 63). Both sensors show a good stability over the analysed period.
3. The temporal average over the period **January 2022 - 27th December 2022** of the elementary ratios (observed reflectance to the simulated one) for **OLCI-A** shows gain values between 2-4% over all the VNIR bands (Figure 64). Unlikely, the temporal average over the same period of the elementary ratios for **OLCI-B** shows gain values within 2% (mission requirements) over the VNIR spectral range (Figure 64). The spectral bands with significant absorption from water vapor and O_2 (Oa11, Oa13, Oa14, Oa15 and Oa20) are excluded.

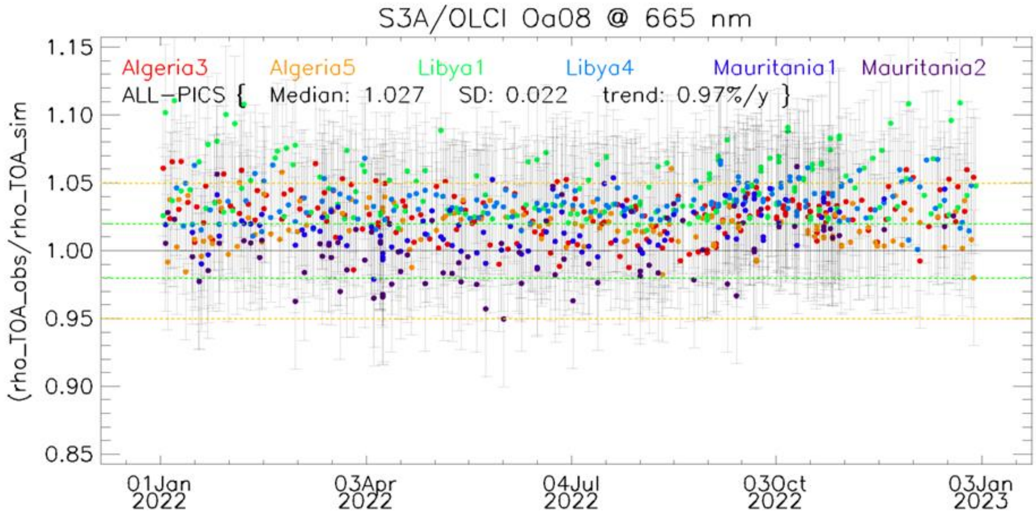

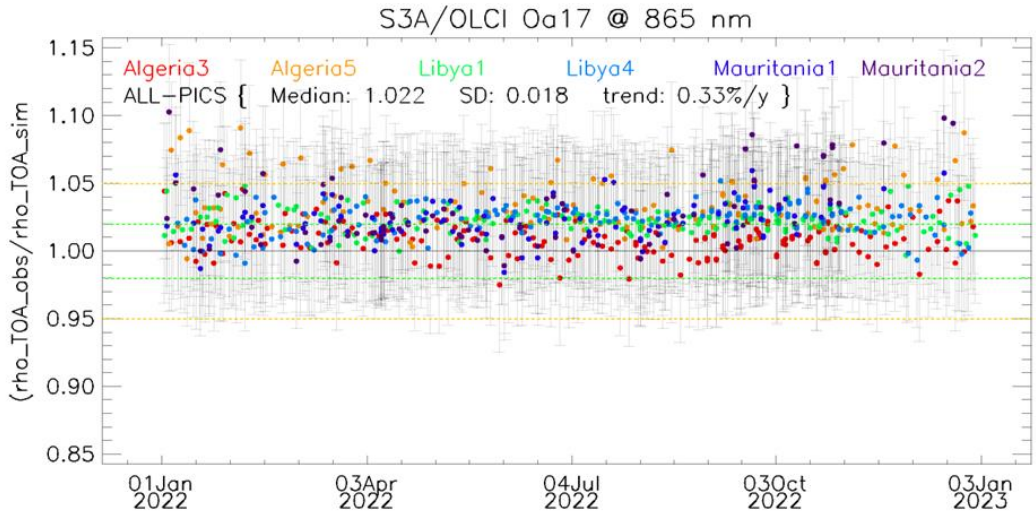

Figure 62: Time-series of the elementary ratios (observed/simulated) signal from OLCI-A for (top to bottom) bands Oa03 and Oa17 respectively over January 2022-End December from the six PICS Cal/Val sites. Dashed-green and orange lines indicate the 2% and 5% respectively. Error bars indicate the desert methodology uncertainty.

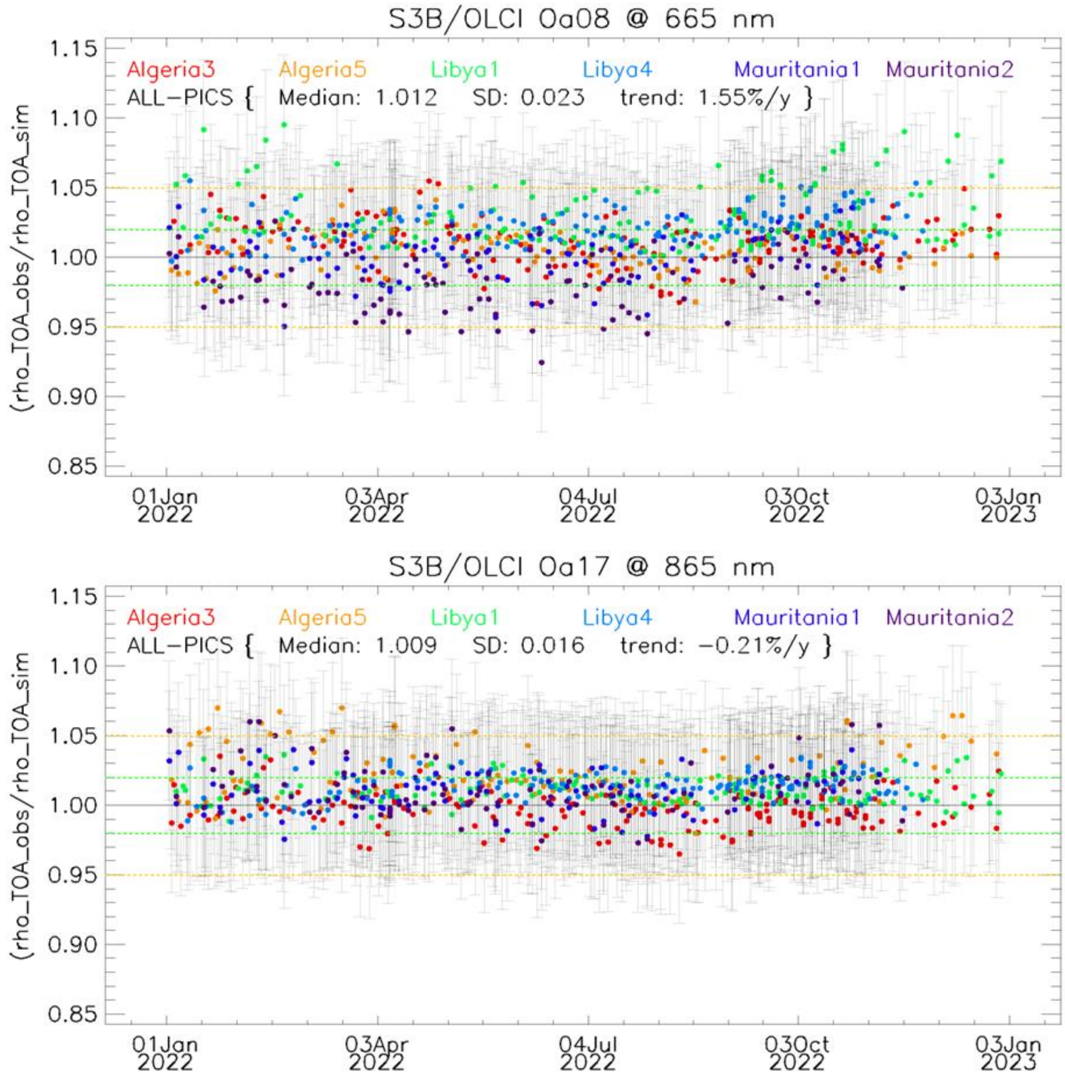

Figure 63: Time-series of the elementary ratios (observed/simulated) signal from OLCI-B for (top to bottom) bands Oa08 and Oa17 respectively over January 2022- End December from the six PICS Cal/Val sites. Dashed-green and orange lines indicate the 2% and 5% respectively. Error bars indicate the desert methodology uncertainty.

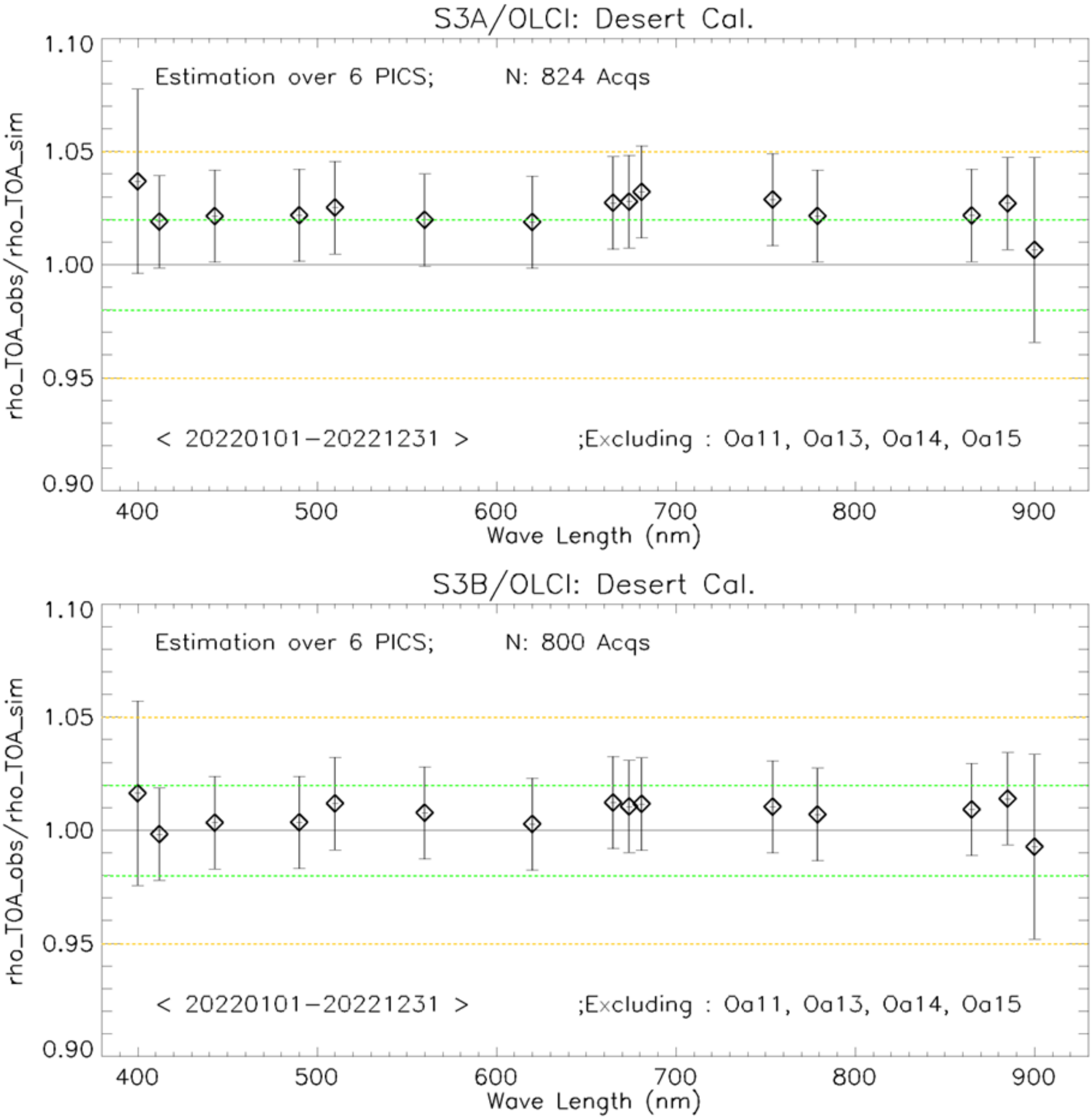

Figure 64: The estimated gain values for OLCI-A and OLCI-B over the 6 PICS sites identified by CEOS over the period January 2022- End December as a function of wavelength. Dashed-green and orange lines indicate the 2% and 5% respectively. Error bars indicate the desert methodology uncertainty.

Validation over Rayleigh

Rayleigh method has been performed from the available mini-files over the period **January 2022- End December 2022** for OLCI-A and OLCI-B. The results were produced with the configuration (ROI-AVERAGE). The gain coefficients of OLCI-A are consistent with the previous results. Bands Oa01-Oa05 display biases values between 3%-5% while bands Oa06-Oa09 exhibit biases between about 2%, just within the mission requirement (Figure 65). The gain coefficients of OLCI-B are lower than OLCI-A ones, where bands Oa01-Oa05 display biases values about 2-5%, when bands Oa6-Oa9 exhibit biases around the 2% mission requirement (Figure 65).

Validation over Glint and synthesis

Glint calibration method with the configuration (ROI-PIXEL) has been performed over the period **January 2022- End December** for OLCI-A and OLCI-B. The outcome of this analysis shows a good consistency with the desert and Rayleigh outputs over the NIR spectral range Oa06-Oa09 for both sensors. Glint results from OLCI-A show that the NIR bands are within the 2% (mission requirements), except Oa21 which shows higher biases more than ~5% for both sensors (see Figure 65). Again, the glint gain from OLCI-B looks slightly lower than OLCI-A one.

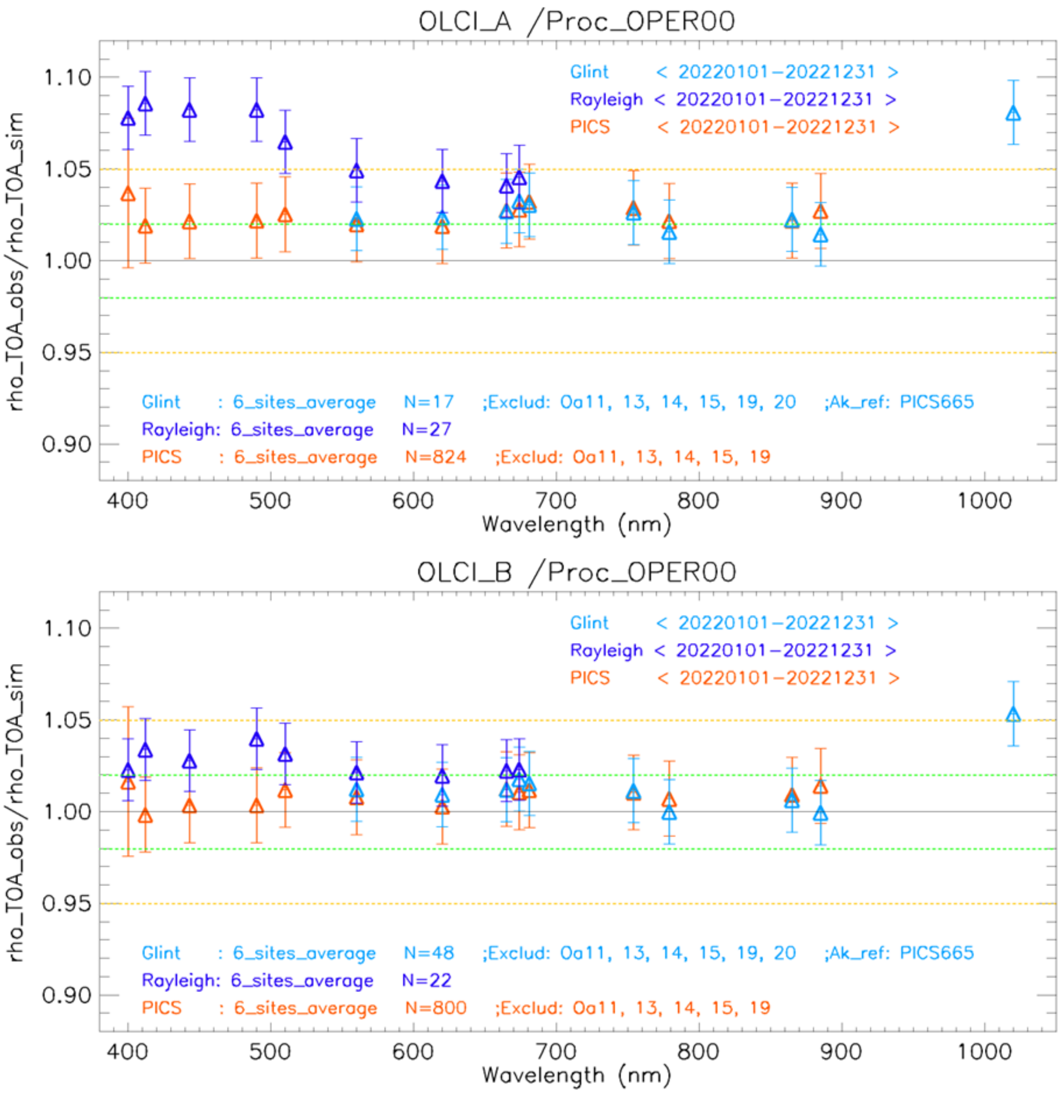

Figure 65: The estimated gain values for OLCI-A and OLCI-B from Glint, Rayleigh and PICS methods over the past twelve months as a function of wavelength. We use the gain value of Oa8 from PICS-Desert method as reference gain for Glint method. Dashed-green and orange lines indicate the 2% and 5% respectively. Error bars indicate the method uncertainties.

Cross-mission Intercomparison over PICS:

X-mission Intercomparison between OLCI-A, OLCI-B, MSI-A, MSI-B, SLSTR-A and SLSTR-B, with MERIS as a reference, has been performed until December 2022 (November for MSI).

Figure 66 shows the estimated gain over different time-series for different sensors over PICS. The spectral bands with significant absorption from water vapor and O2 are excluded. OLCI-A seems to have higher gain wrt the other sensors (except SLSTR-A/B), and of about 1-2% higher gain wrt to OLCI-B over VNIR spectral range.

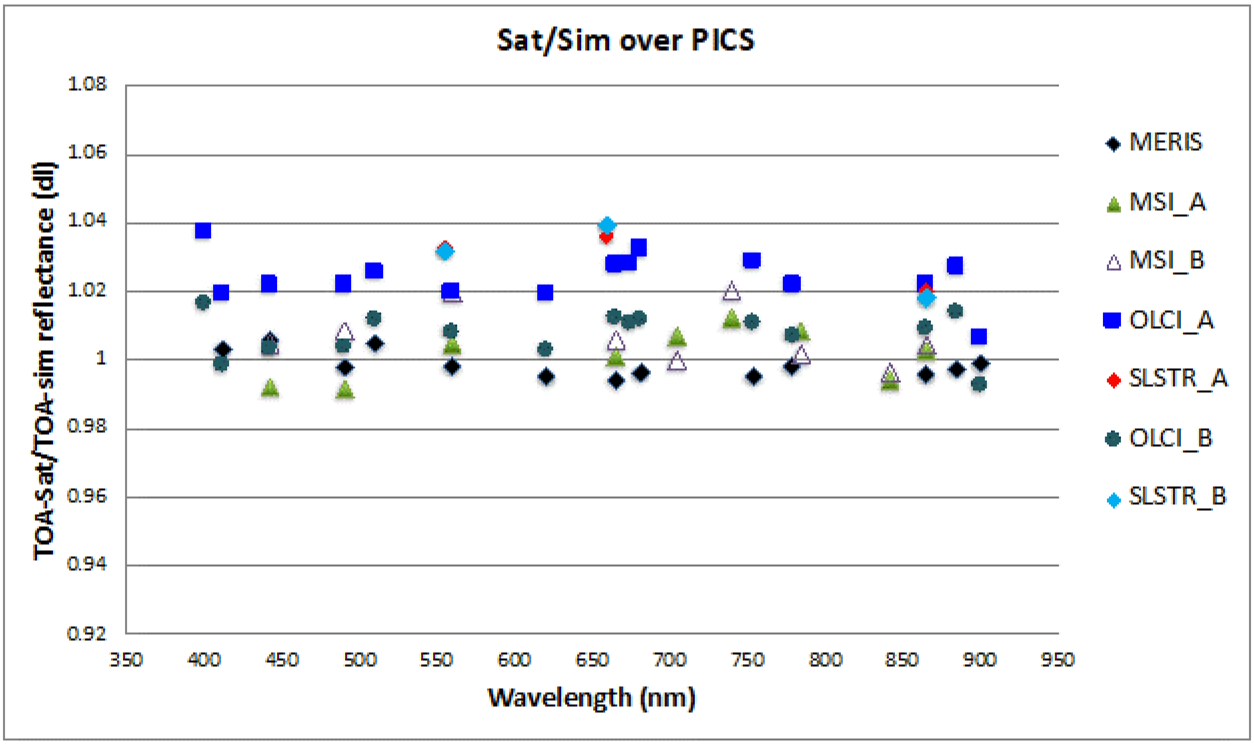

Figure 66: Ratio of observed TOA reflectance to simulated one for (pale-green) S2A/MSI, (white) S2B/MSI, (Orange) Aqua/MODIS, (blue) S3A/OLCI, (green) S3B/OLCI, (red) S3A/SLSTR, and (cyan) S3B/SLSTR averaged over the six PICS test sites as a function of wavelength. S2A/B and S3A/B averaged over 2022 only.

3.1.3 Radiometric validation with OSCAR

OSCAR Rayleigh results

The OSCAR Rayleigh have been applied to the S3A and S3B S3ETRAC data from the 6 oceanic calibration sites (Table 3) using a new chlorophyll climatology which has been derived from the CMEMS OLCI monthly CHL products from considering the years 2017, 2018 and 2019.

Table 3: S3ETRAC Rayleigh Calibration sites

Site Name	Ocean	North Latitude	South Latitude	East Longitude	West Longitude
PacSE	South-East of Pacific	-20.7	-44.9	-89	-130.2
PacNW	North-West of Pacific	22.7	10	165.6	139.5
PacN	North of Pacific	23.5	15	200.6	179.4
AtlN	North of Atlantic	27	17	-44.2	-62.5
AtlS	South of Atlantic	-9.9	-19.9	-11	-32.3
IndS	South of Indian	-21.2	-29.9	100.1	89.5

In Figure 67 the average OSCAR OLCI-A and OLCI-B Rayleigh results are given for December 2022. In Figure 68 and Table 4 the average of all 2022 scenes is given.

In the lower wavelengths, S3A/OLCI remains significantly brighter than S3B/OLCI.

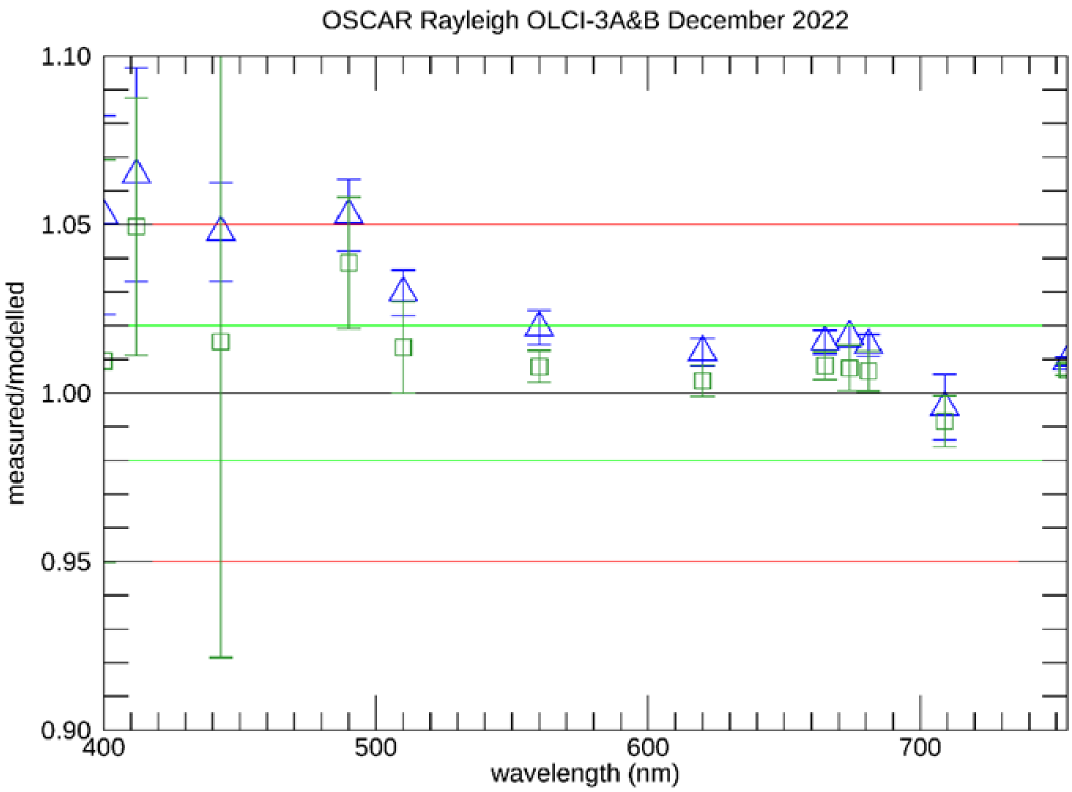

Figure 67: OSCAR Rayleigh S3A and S3B Calibration results as a function of wavelength for December 2022. The results are obtained with a new climatology derived from CMEMS OLCI monthly CHL products.

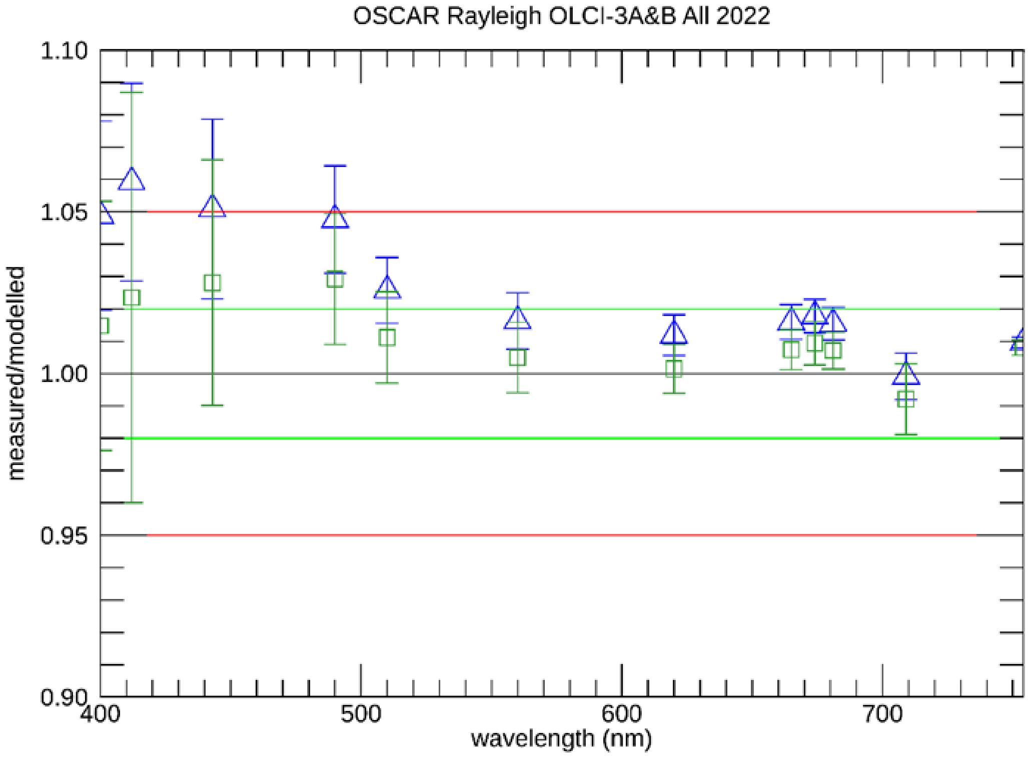

Figure 68. OSCAR Rayleigh S3A and S3B Calibration results as a function of wavelength for Jan – December 2022. Average and standard deviation over all scenes currently (re)processed with the new climatology.

Table 4. OSCAR Rayleigh calibration results for S3A and S3B (average and standard deviation over all 2022 acquisitions) over all scenes currently (re)processed with the new climatology and observed difference (in %) between OLCIA and OLCIB

OLCI band	Wavelength (nm)	Oscar Rayleigh OLCIA avg	Oscar Rayleigh OLCIA stdev	Oscar Rayleigh OLCIB avg	Oscar Rayleigh OLCIB stdev	% difference OLCIA and OLCIB
Oa01	400	1.049	0.029	1.015	0.039	3.25%
Oa02	412	1.059	0.031	1.024	0.063	3.37%
Oa03	443	1.051	0.028	1.028	0.038	2.17%
Oa04	490	1.048	0.017	1.029	0.020	1.75%
Oa05	510	1.026	0.010	1.011	0.014	1.42%
Oa06	560	1.016	0.009	1.005	0.011	1.11%
Oa07	620	1.012	0.006	1.002	0.008	1.02%
Oa08	665	1.016	0.005	1.007	0.006	0.84%
Oa09	674	1.018	0.005	1.009	0.007	0.82%
Oa10	681	1.015	0.005	1.007	0.006	0.82%
Oa11	709	0.999	0.007	0.992	0.011	0.70%
Oa12	754	1.010	0.002	1.008	0.002	0.16%

OSCAR Glitter results

The OSCAR Glitter have been applied to all S3ETRAC glitter data for the year 2022. Both OLCI-A and OLCI-B data was processed and the yearly values for 2022 are plotted. There are no monthly values available, only total yearly plots are produced. The plots in Figure 69 and Figure 70 are the glitter results for OLCI-A and OLCI-B. The values are in absolute terms, since all bands are referenced to the Rayleigh result of band Oa8. The glitter method is a relative inter-band calibration method, since the Oa8 band is used to estimate windspeed. By multiplying all band results with the Rayleigh calibration factor for the same period, the results are referenced to the result this method.

The results are within 2% for all bands, except for bands Oa4 and Oa21 for both OLCI-A and OLCI-B.

The difference between OLCI-A and OLCI-B (Table 5 in %) is not higher 1% for all bands, except for bands Oa04,Oa05 and Oa06. It also indicates a brighter OLCI-A compared to OLCI-B.

For comparison reasons, the results of year 2021 are added to Table 6. As can be observed, values are highly similar, with only minor differences in the results for all bands.

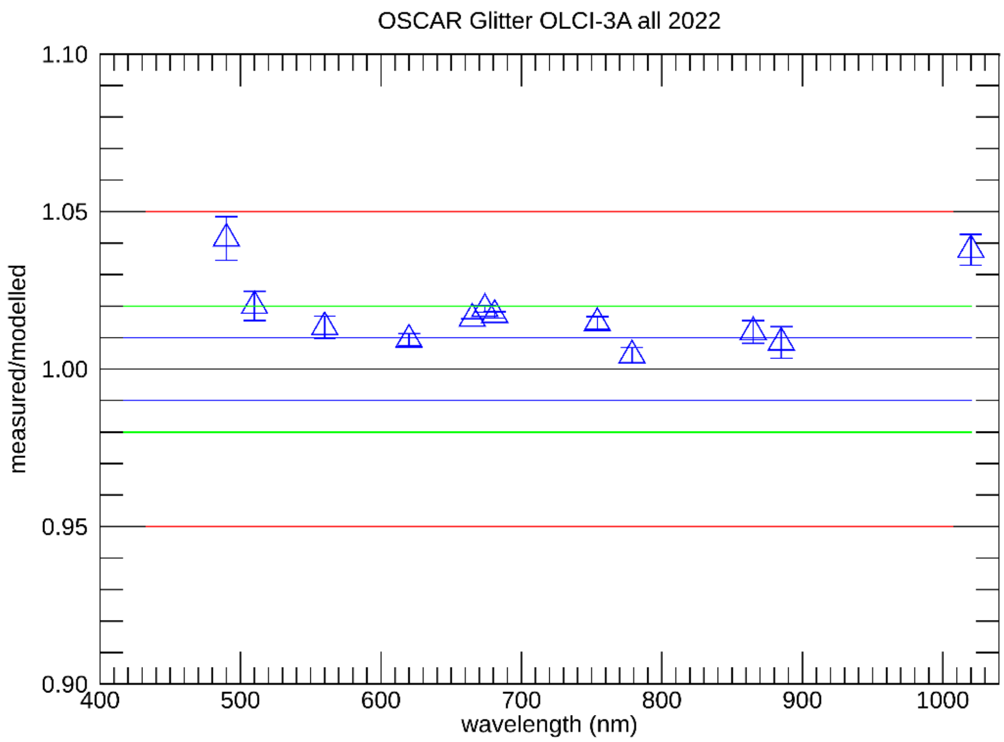

Figure 69: OSCAR Glitter OLCI-A Calibration results as a function of wavelength for all data of 2022. Average and standard deviation over all scenes currently (re)processed with the new climatology.

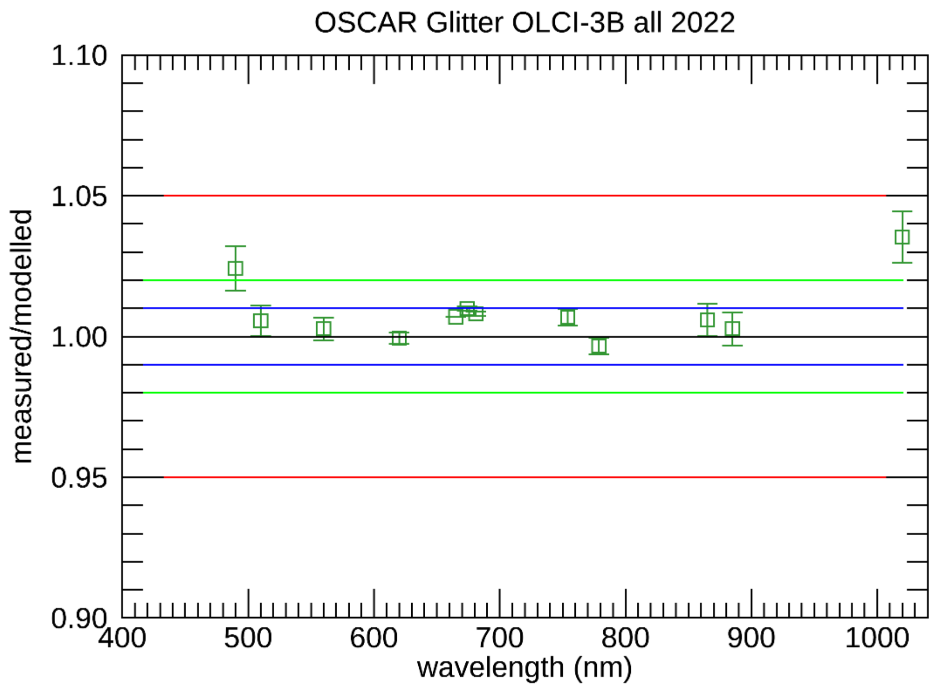

Figure 70: OSCAR Glitter OLCI-B Calibration results as a function of wavelength for all data of 2022. Average and standard deviation over all scenes currently (re)processed with the new climatology.

Table 5: OSCAR Glitter calibration results for OLCI-A and OLCI-B (average and standard deviation over all acquisitions of 2022) currently processed with the new climatology and observed difference (in %)

OLCI band	Wavelength (nm)	Oscar Glitter OLCIA		Oscar Glitter OLCIB		% difference OLCIA and OLCIB
		avg	stdev	avg	stdev	
Oa04	490	1.041	0.007	1.024	0.008	1.66%
Oa05	510	1.020	0.005	1.006	0.005	1.42%
Oa06	560	1.013	0.003	1.003	0.004	1.04%
Oa07	620	1.009	0.002	0.999	0.002	0.99%
Oa08	665	1.016	0.000	1.007	0.000	0.89%
Oa09	673.75	1.019	0.001	1.010	0.001	0.89%
Oa10	681.25	1.017	0.001	1.008	0.001	0.90%
Oa12	753.75	1.015	0.002	1.007	0.003	0.76%
Oa16	778.75	1.004	0.002	0.997	0.003	0.77%
Oa17	865	1.012	0.004	1.006	0.006	0.57%
Oa18	885	1.008	0.005	1.003	0.006	0.56%
Oa21	1020	1.038	0.005	1.035	0.009	0.25%

Table 6: OSCAR Glitter calibration results for OLCI-A and OLCI-B (average and standard deviation over all acquisitions of 2021) currently processed with the new climatology and observed difference (in %)

OLCI band	Wavelength	Oscar Glitter OLCIA		Oscar Glitter OLCIB		% difference OLCIA and OLCIB
	(nm)	avg	stdev	avg	stdev	
Oa04	490	1.038	0.007	1.021	0.005	1.70%
Oa05	510	1.017	0.004	1.003	0.004	1.38%
Oa06	560	1.012	0.003	1.003	0.003	0.92%
Oa07	620	1.009	0.002	1.000	0.002	0.92%
Oa08	665	1.016	0.000	1.007	0.000	0.89%
Oa09	673.75	1.019	0.001	1.010	0.001	0.89%
Oa10	681.25	1.017	0.001	1.008	0.001	0.90%
Oa12	753.75	1.015	0.002	1.008	0.002	0.73%
Oa16	778.75	1.005	0.003	0.997	0.002	0.75%
Oa17	865	1.012	0.004	1.007	0.004	0.46%
Oa18	885	1.008	0.005	1.004	0.005	0.45%
Oa21	1020	1.038	0.005	1.037	0.005	0.11%

3.1.4 Radiometric validation with Moon observations

There has been no new result during the reporting period. Last figures (reported in Data Quality Report for February 2022) are considered valid.

4 Level 2 Land products validation

4.1 [OLCI-L2LRF-CV-300]

4.1.1 Routine extractions

- The focus for this time period has been on the rolling archive Non Time Critical (NT) data until the 31st of July 2022. More data available for statistical analysis as a concatenation procedure for all available data in the MERMAID processing has been implemented.
- Concatenated time series of OLCI Global Vegetation Index and OLCI Terrestrial Chlorophyll Index have been regenerated on the current rolling archive availability including previous extractions since June 2016 and April 2018 for S3A and S3B respectively.

4.1.1.1 OLCI-A

Figure 71 to Figure 80 below present the Core Land Sites OLCI-A time series over the current period.

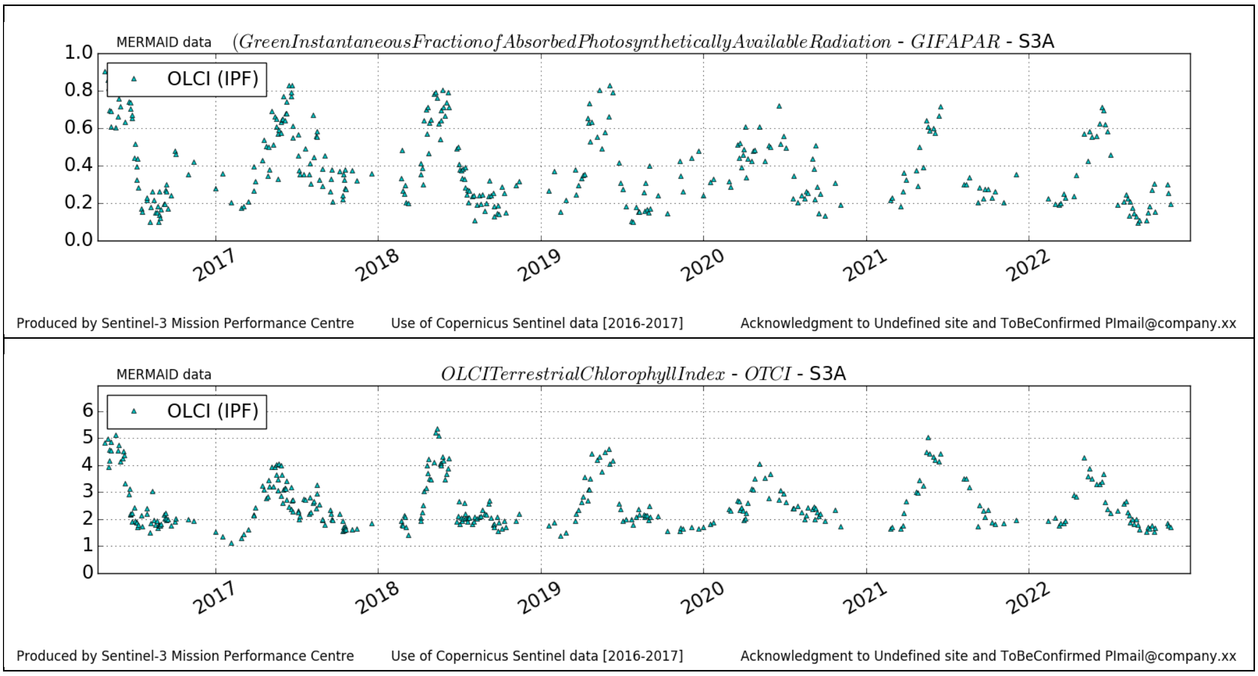

Figure 71: DeGeb time series over current report period

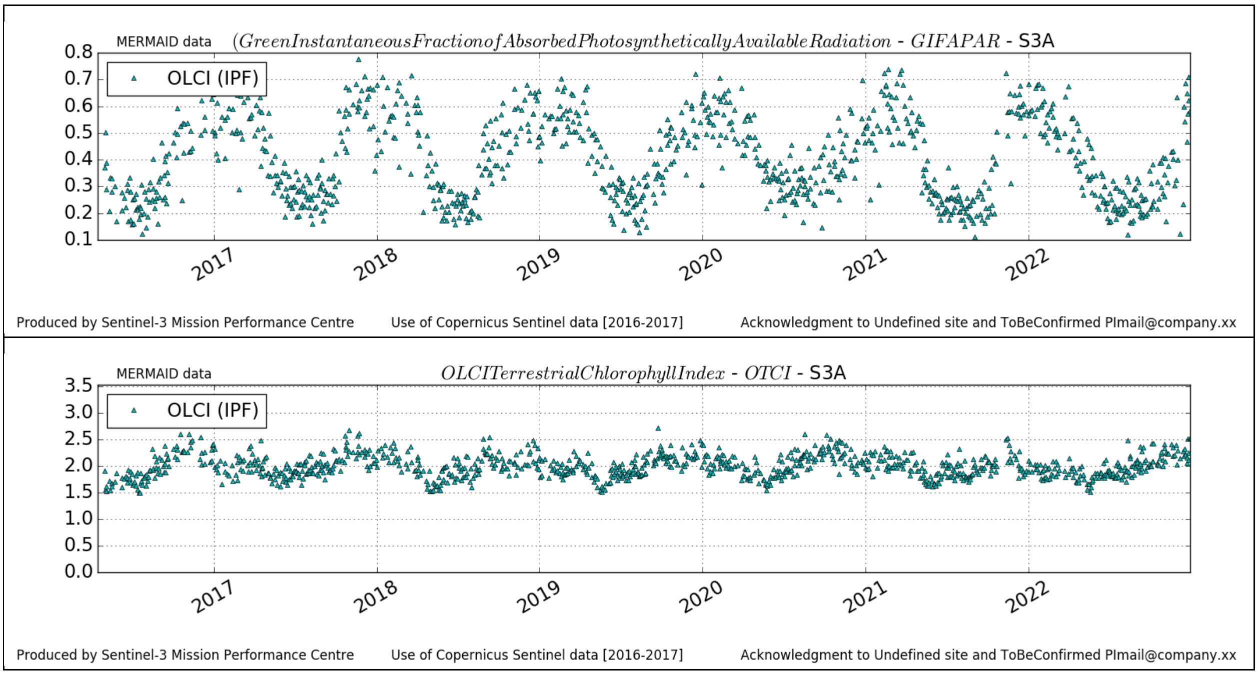

Figure 72: ITCat time series over current report period

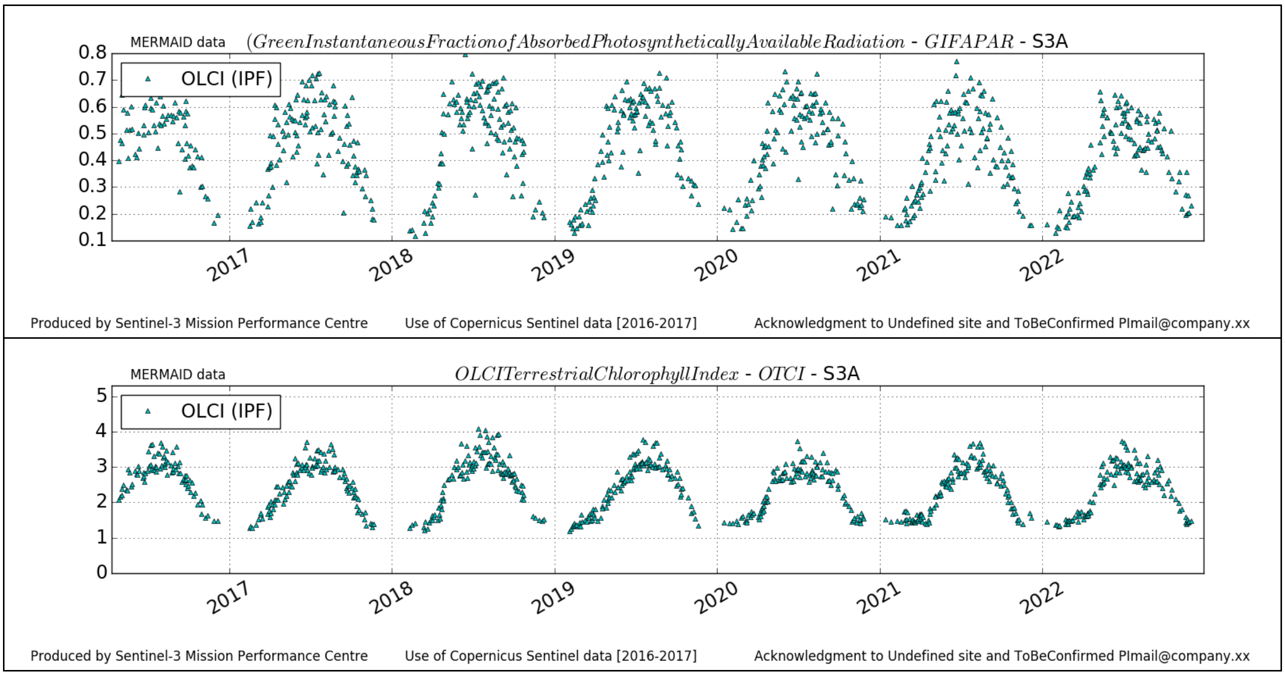

Figure 73: ITIsp time series over current report period

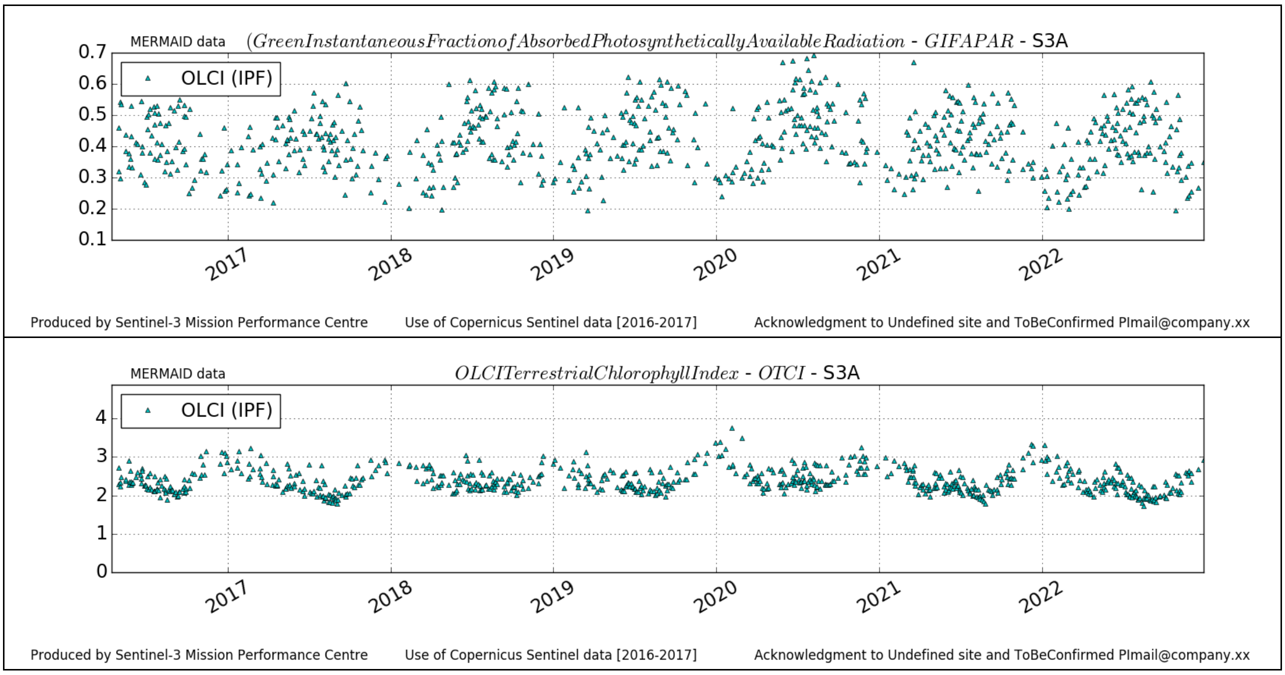

Figure 74: ITSro time series over current report period

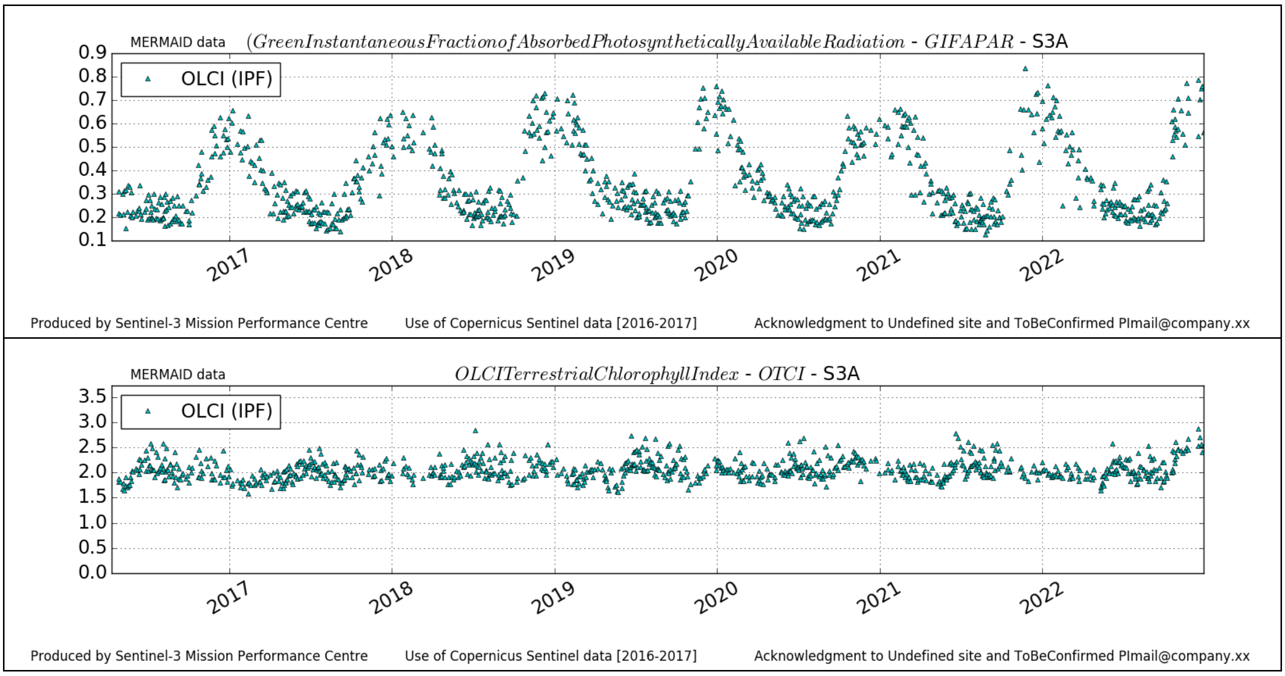

Figure 75: ITTra time series over current report period

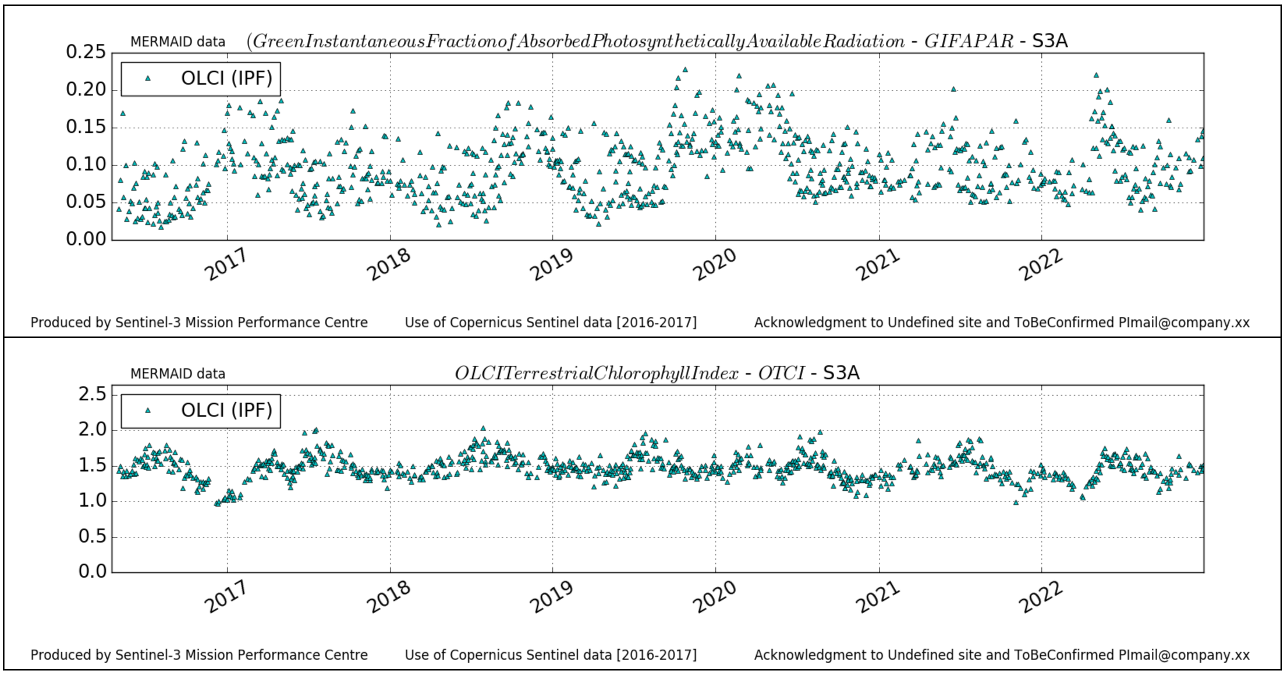

Figure 76: SPAli time series over current report period

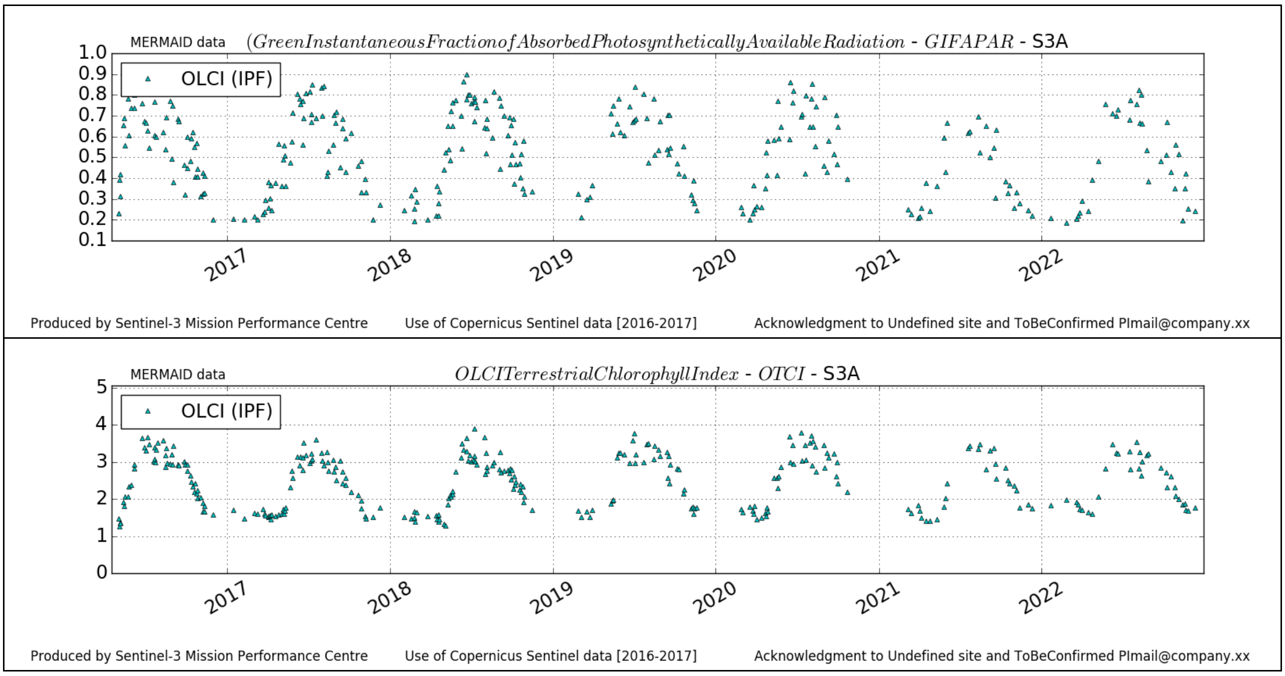

Figure 77: UKNFo time series over current report period

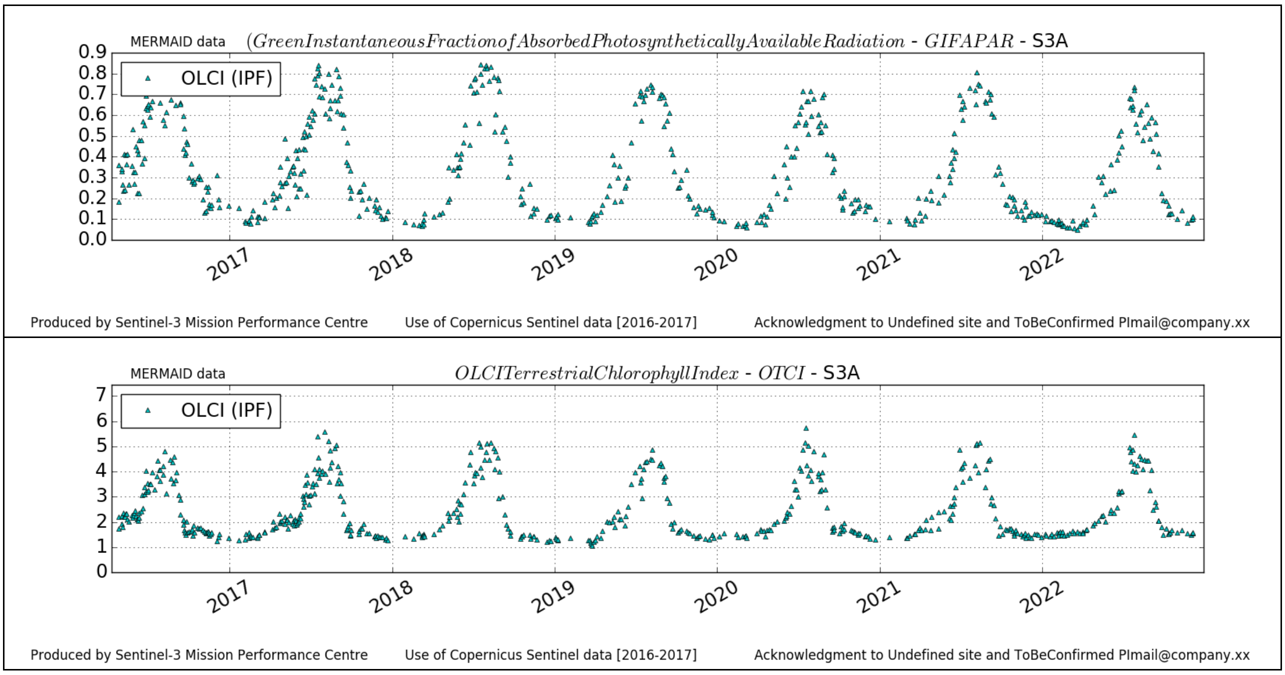

Figure 78: USNe1 time series over current report period

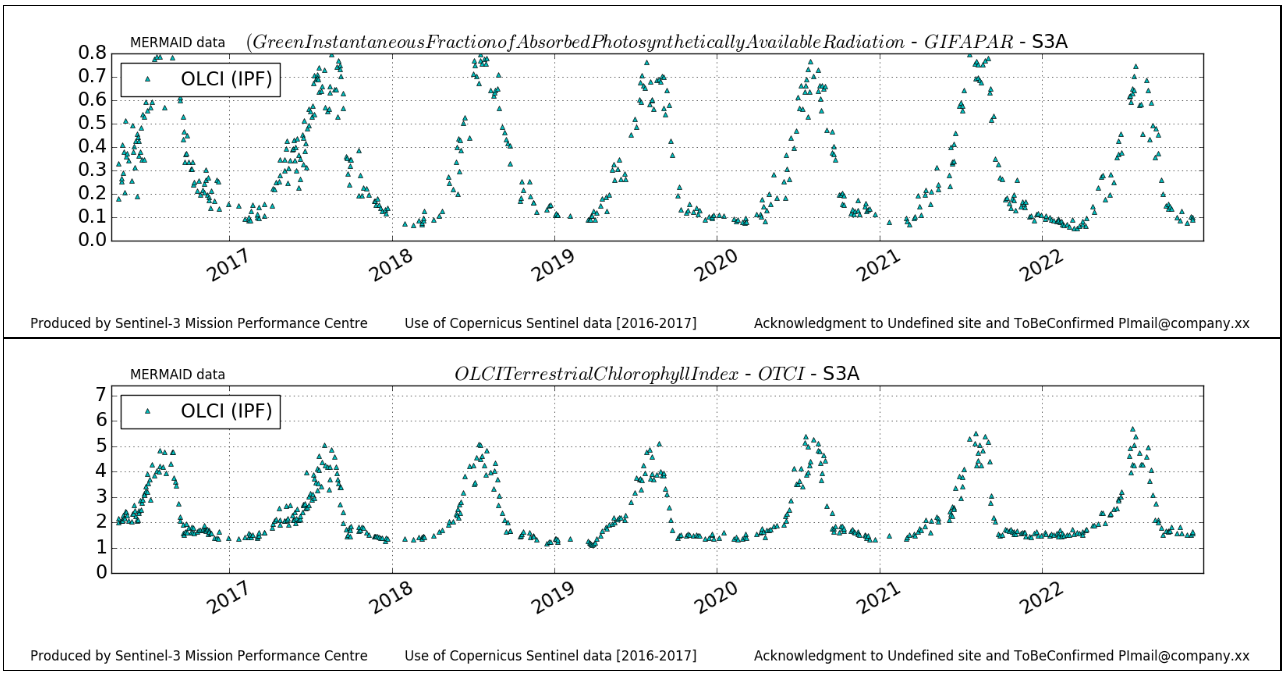

Figure 79: USNe2 time series over current report period

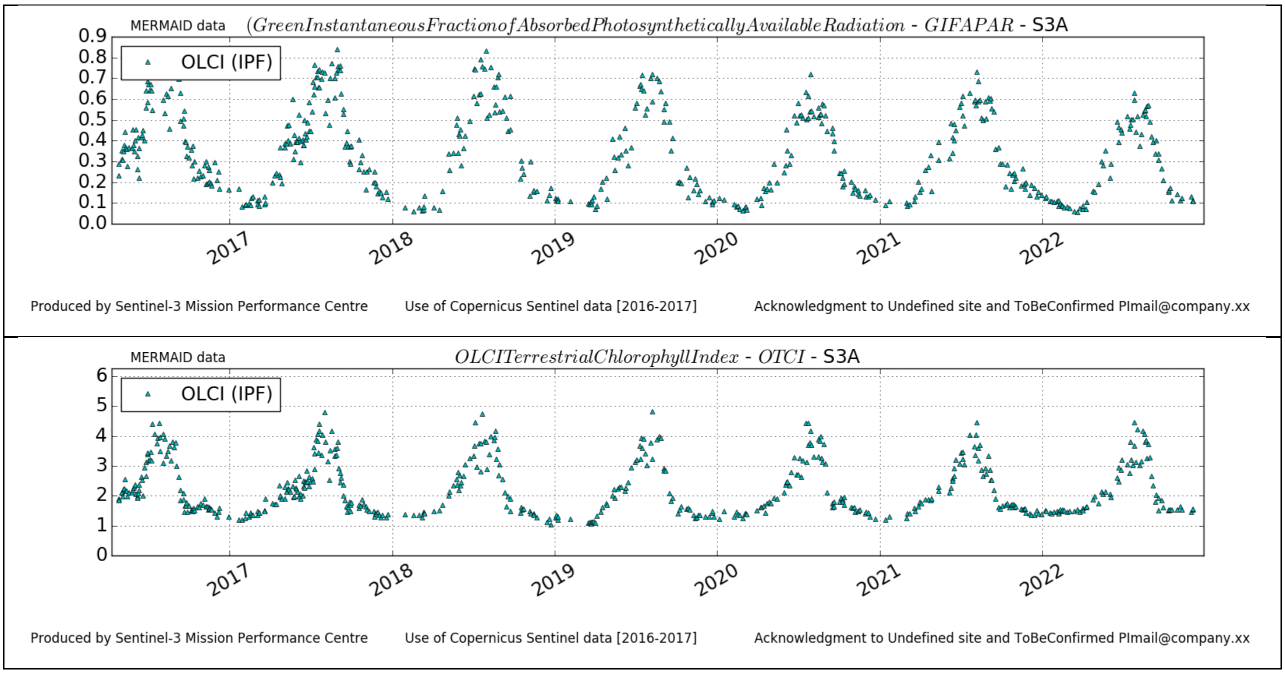

Figure 80: USNe3 time series over current report period

4.1.1.2 OLCI-B

Figure 81 to Figure 90 below present the Core Land Sites OLCI-B time series over the current period.

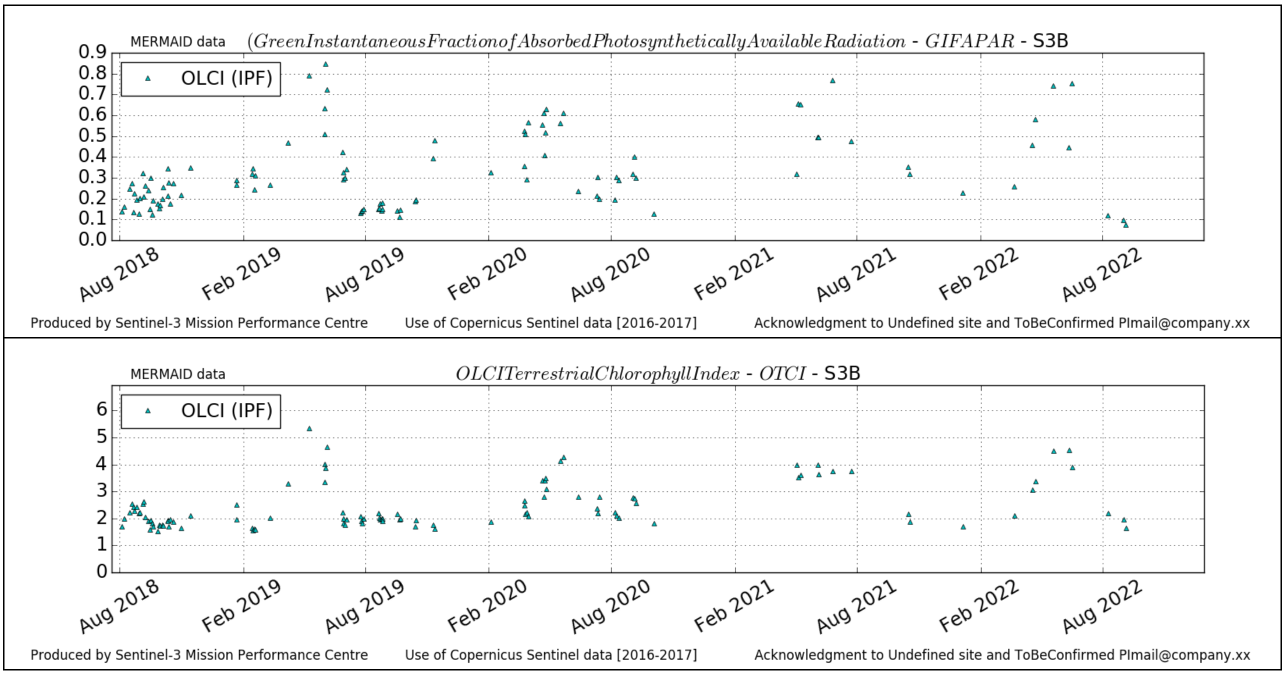

Figure 81: DeGeb time series over current report period

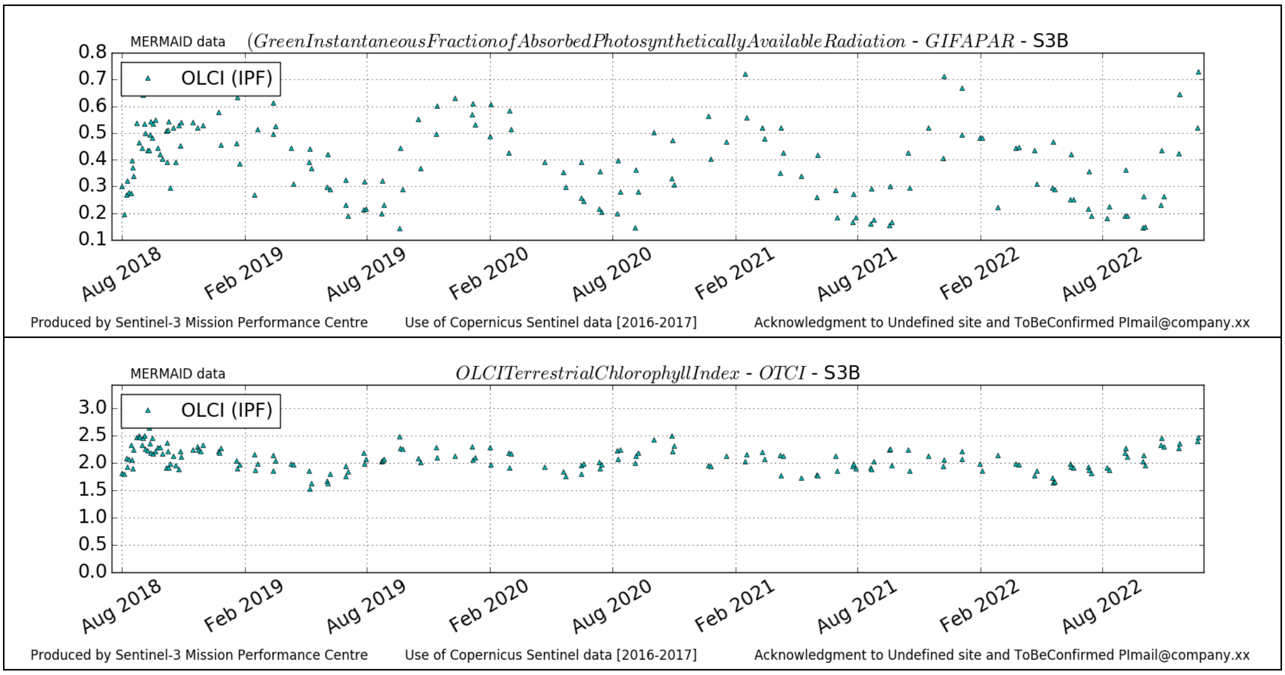

Figure 82: ITCat time series over current report period

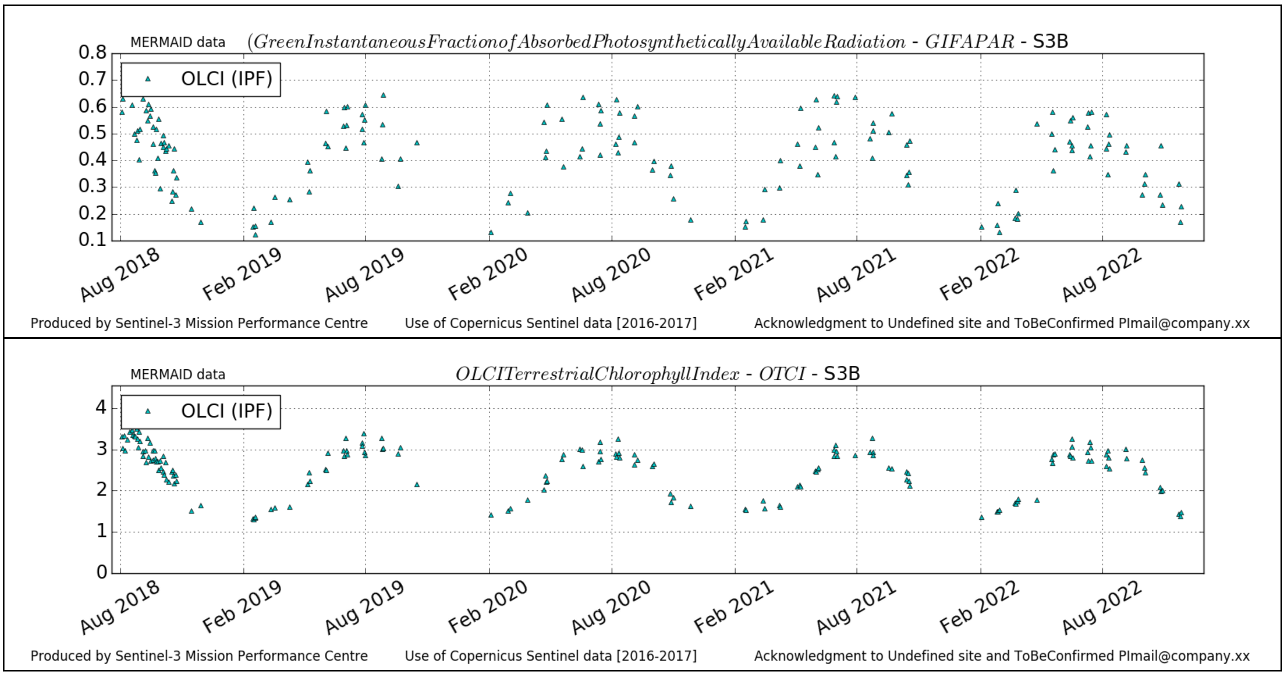

Figure 83: ITIsp time series over current report period

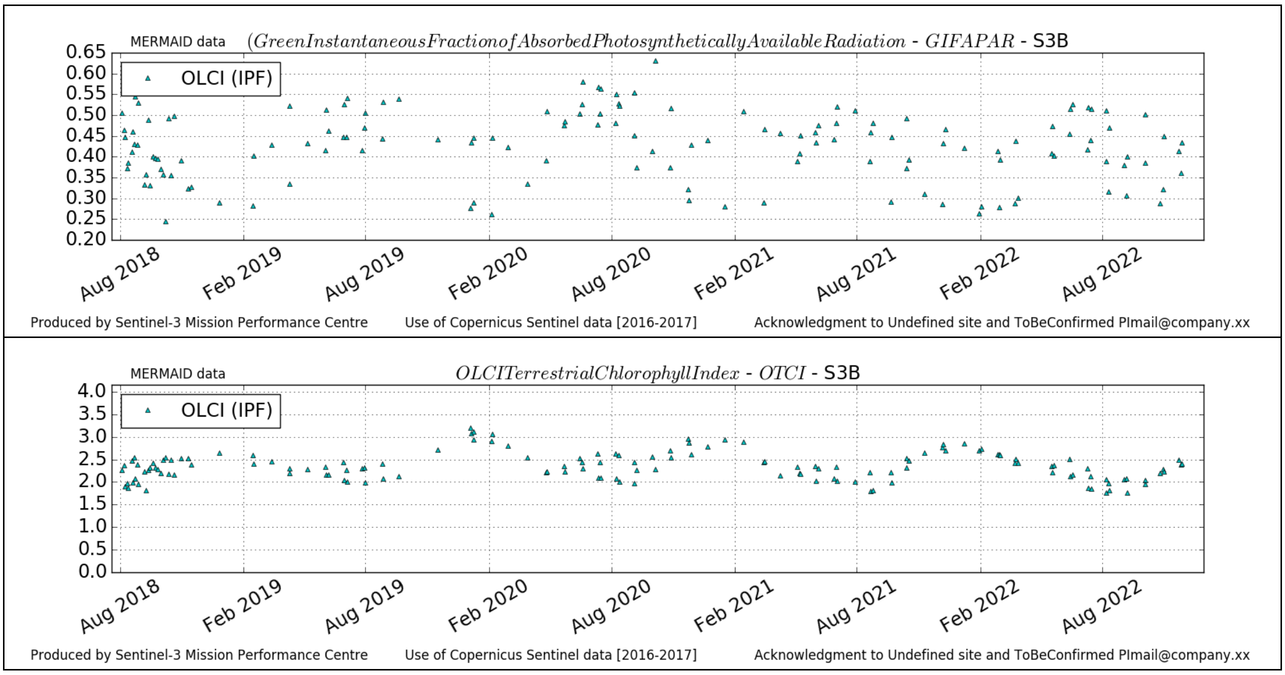

Figure 84: ITSro time series over current report period

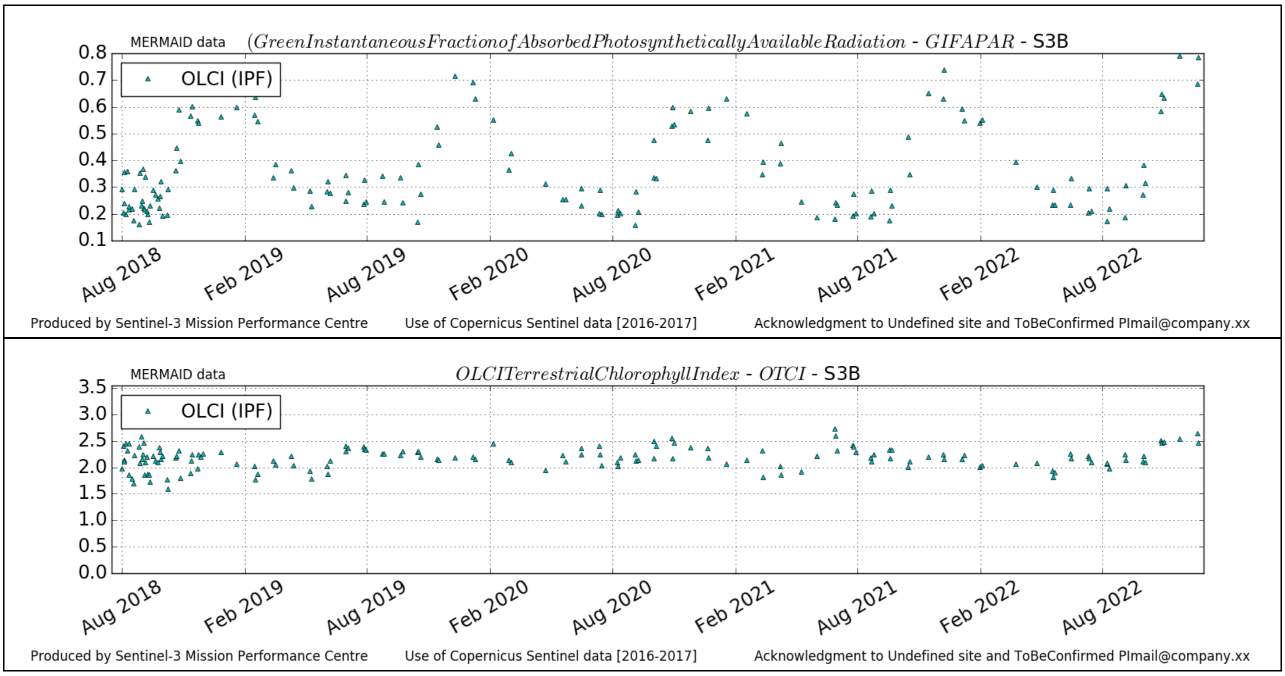

Figure 85: ITTra time series over current report period

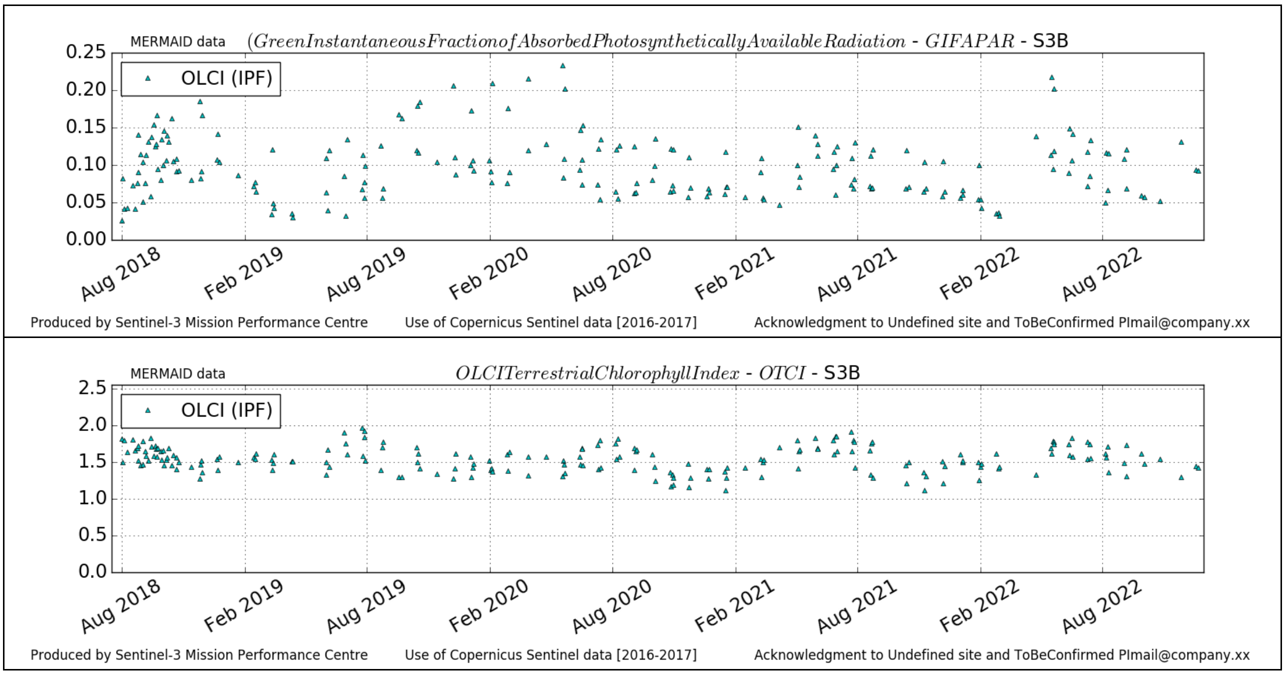

Figure 86: SPAli time series over current report period

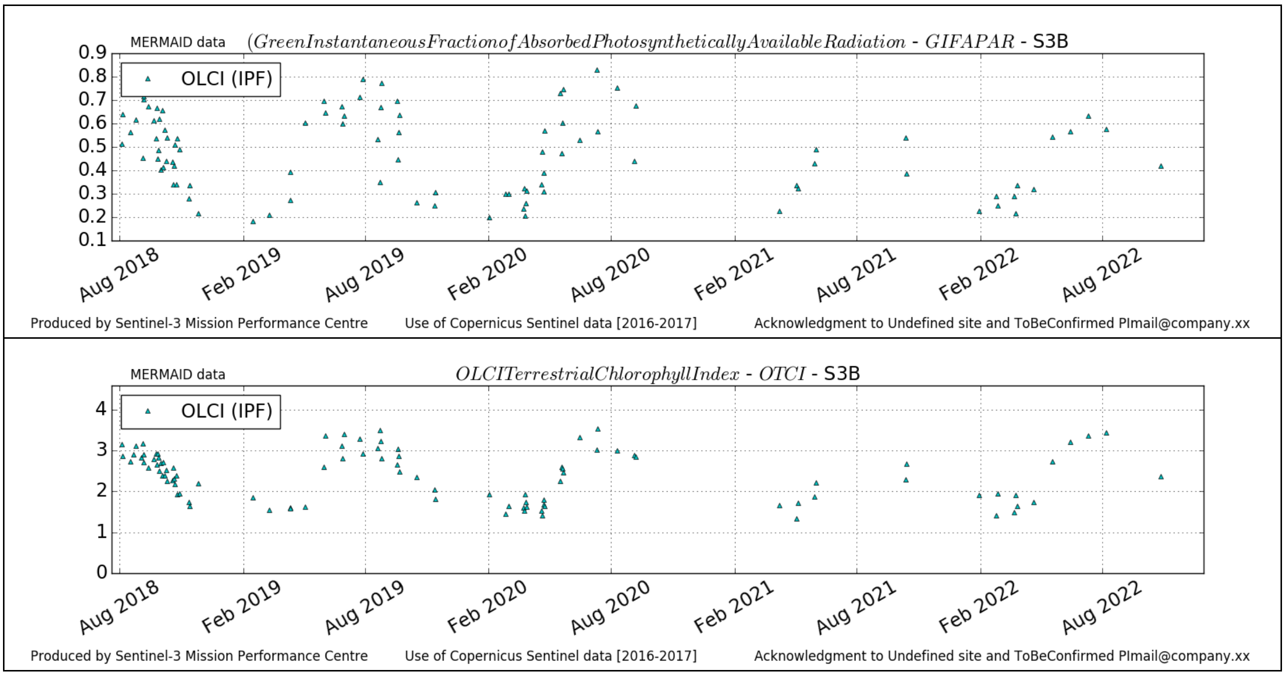

Figure 87: UKNFo time series over current report period

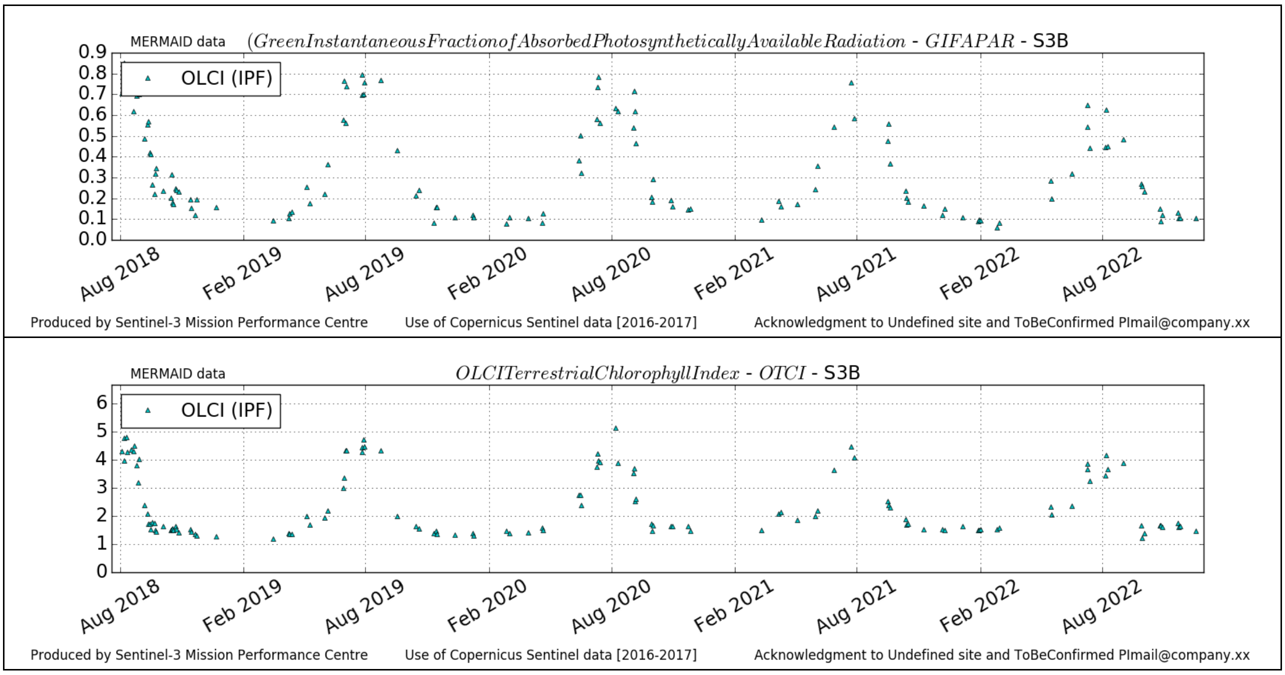

Figure 88: USNe1 time series over current report period

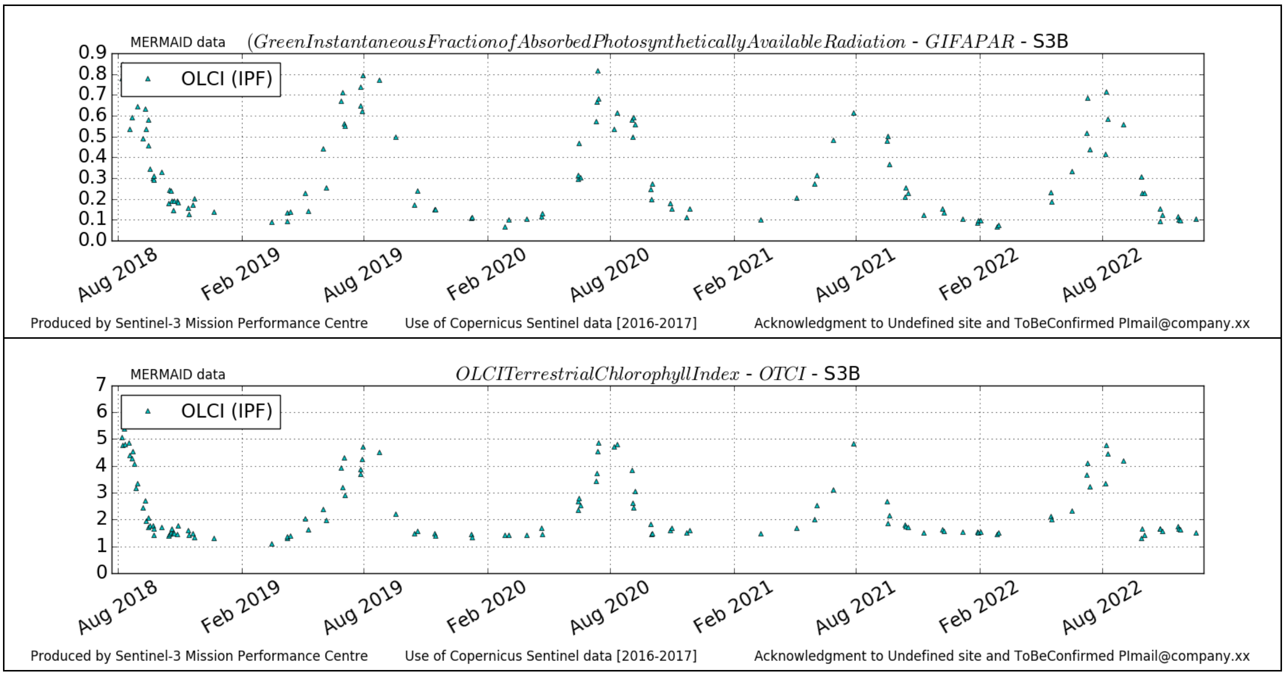

Figure 89: USNe2 time series over current report period

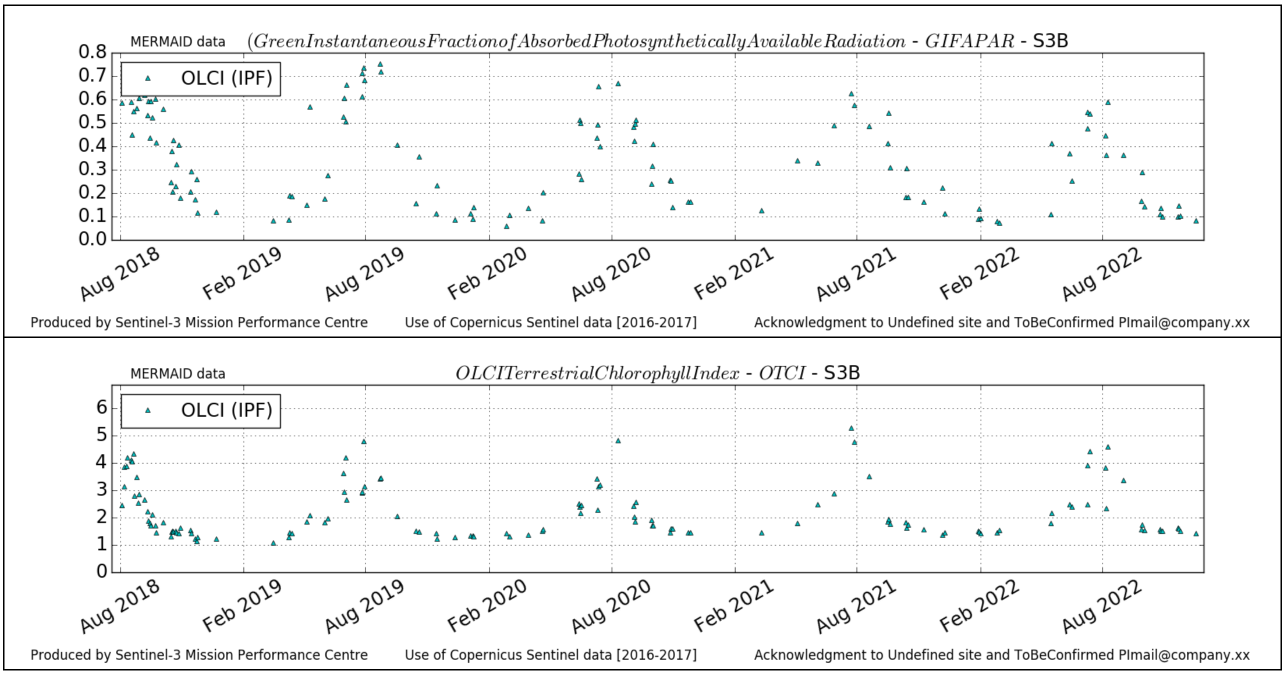

Figure 90: USNe3 time series over current report period

4.1.2 Comparisons with MERIS MGVI and MTCI climatology

There has been no new result during the reporting period. Last figures (reported in OLCI Data Quality Report covering May 2022) are considered valid.

4.1.3 Comparisons with GBOV (Ground-Based Observations for Validation) data v3

This report compares the ground-based measurements from the Copernicus GBOV service and OLCI GIFAPAR until 31ST December 2021. Compared to the previous DQR (November 2022), GBOV 2021 data is included. The validation is conducted using the MERMAID extractions of Sentinel-3 (i.e., 81 for OLCI-A and 25 for OLCI-B) over twelve established validation sites and GBOV fAPAR land product (LP4). The selected sites are distributed across various geographical locations representing different land cover types (Table 7).

Table 7: GBOV validation sites analysed in a monthly report

ID	Name	Country	LAT	LON	IGBP	GBOV Dates	Min DOY MaxDOY
USA_BART	Bartlett Experimental	USA	44.0639	-71.2873	Mixed Forest	20140104 - 20211217	8 - 349
USA_CPER	Central Plains Experimental Range	USA	40.81555	-104.7460	Grasslands	20140116 - 20211229	3 - 362
PRI_GUAN	Guanica Forest	Puerto Rico	17.9695	-66.8687	Evergreen Broadleaf	20150131- 20211228	8 - 349
GER-HAIN	Hainich	Germany	51.0792	10.4522	Mixed Forest	20200102 - 20211221	8-349
USA_HARV	Harvard	USA	42.5378	-72.1715	Mixed Forest	20140104 - 20211228	8 - 349
USA_JORN	Jornada	USA	32.5907	-106.842	Open Shurbland	20160106 - 20211229	3 - 362
AUS_Litchfield	Litchfield	AUS	-13.18	130.79	Woody Savannas	20210308 – 20211215	3 - 362
USA_Moab	Moab	USA	38.2483	-109.388	Open shrubland	20150108 – 20201220	3 - 362
USA_ORNL	Oak Ridge	USA	35.9641	-84.2826	Mixed Forest	20150117 – 20211230	8 - 349
USA_SCBI	Smithsonian Conservation Biology	USA	38.8902	-78.1395	Mixed Forest	20150105 – 20211224	8 – 349
USA_STEI	Steigerwaldt Land Services	USA	45.5089	-89.5864	Deciduous Broadleaf	20160123 – 20211229	8 - 349
USA_TALL	Talladega National Forest	USA	32.9504	-87.3933	Evergreen Needleleaf	20150131 - 202112283	8 - 349

The methodology involves 1) extracting the GBOV values of the Land Product (LP) at 300 m (WGS-84) overlapping the S3 pixels, 2) filtering OLCI-A/OLCI-B and GBOV data, and 3) plotting the temporal profiles. Sentinel data are filtered following the quality flags (i.e., GIFAPAR_FAIL, CLOUD, GIFAPAR_CLASS_BAD, GIFAPAR_CLASS_WS, GIFAPAR_CLASS_CSI, GIFAPAR_CLASS_BRIGHT, COSMETIC, SUSPECT, no valid values - 255). GBOV data are filtered according to the recommendations (https://gbov.acri.fr/userSupport/). Hence the values removed include 1) values with input or output out of range, 2) values outside the season used to establish the calibration function (Min DOY and Max DOY Table) and 3) threshold <50% on the percentage of valid native spatial resolution pixels.

To check the consistency and seasonality of OLCI GIFAPAR, the scatter plots between OLCI-A and OLCI-B for equal dates have been performed by site (left) and by land cover type (right). A high correlation (>0.9) is found.

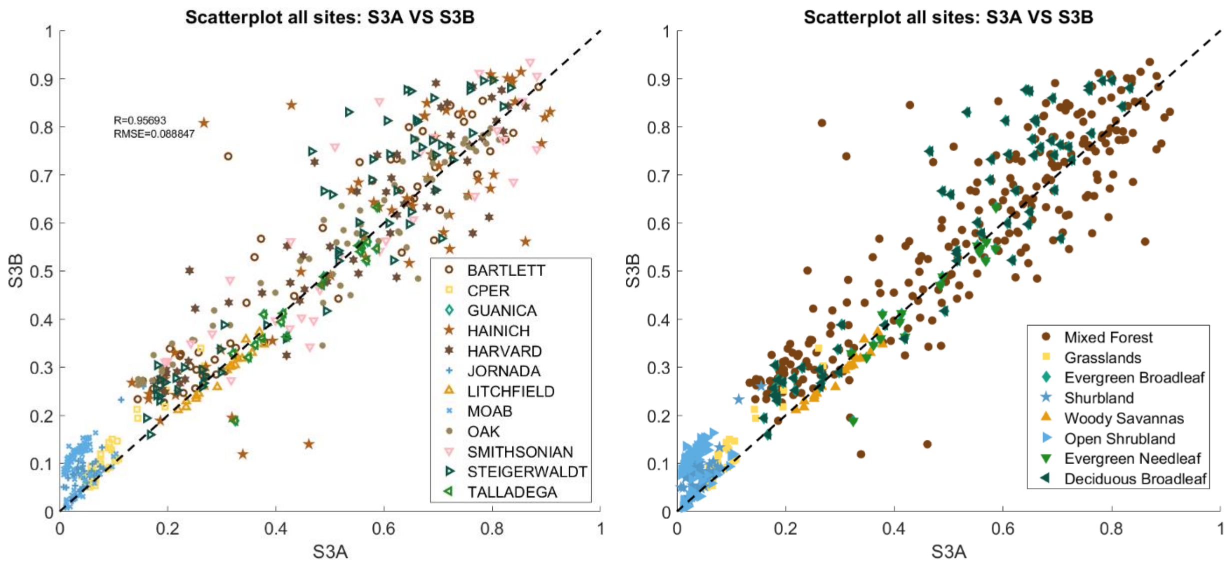

Figure 91: Scatter plots between OLCI-A and OLCI-B of equal dates for left) sites and right) Land Cover Types.

4.1.3.1 OLCI-A

Figure 92 to Figure 97 show the variability of both in situ values from GBOV and their corresponding OLCI-A matchups in time. OLCI-A reproduces the temporal variations of GBOV values for almost all sites satisfactorily. However, GBOV products provide systematically higher values than satellite products in forest classes. On the contrary, for shrubland and grasslands, satellite products tend to present higher values than GBOV. Results for 2021 are similar to previous years.

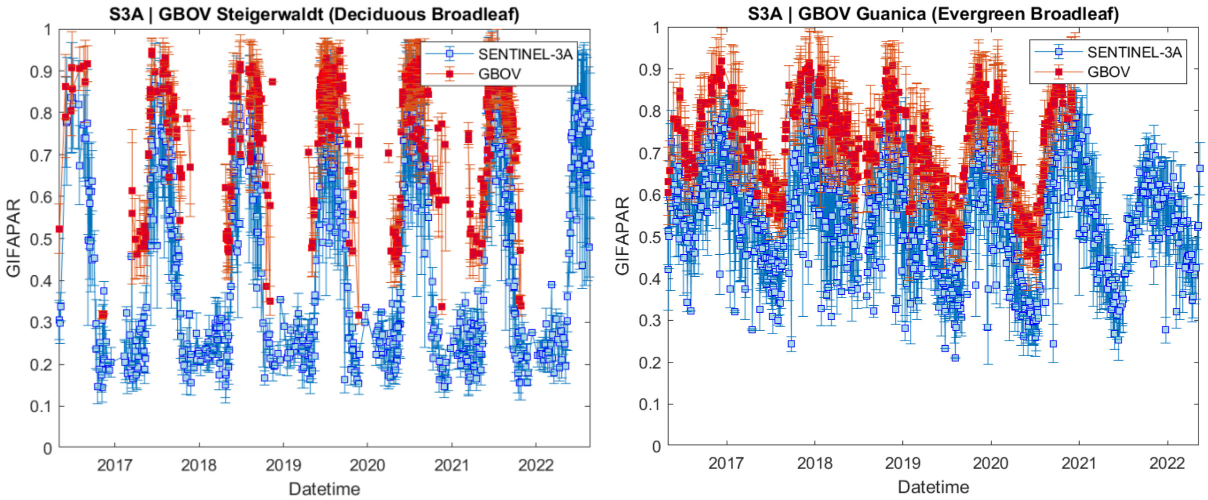

Figure 92: Time series of GBOV FIPAR LP4 (red) and OLCI-A GIFPAR (blue) for sites Steigerwaldt (left) and Guanica (right)

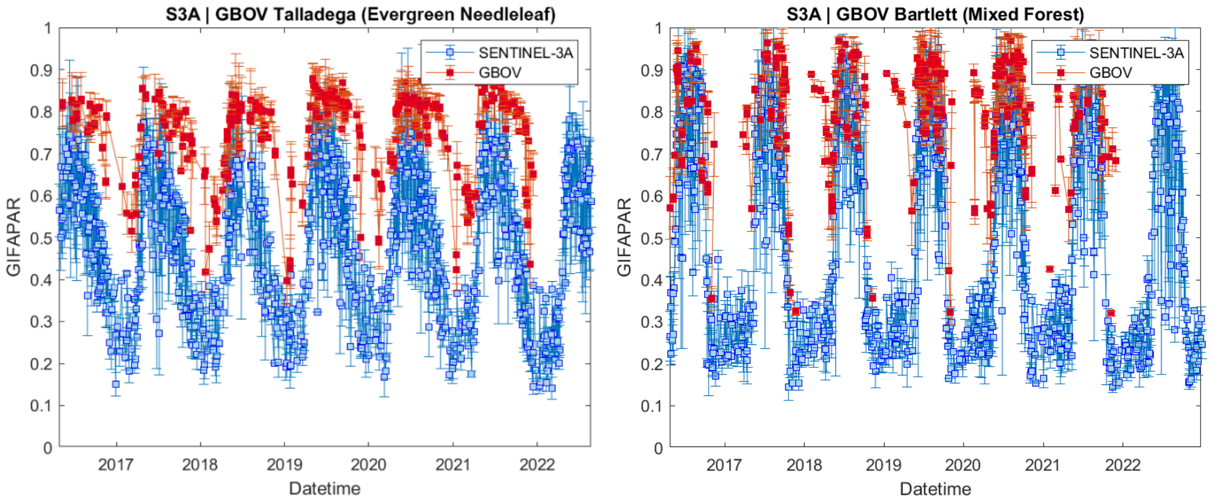

Figure 93: same as Figure 92 for sites Talladega (Left) and Bartlett (right)

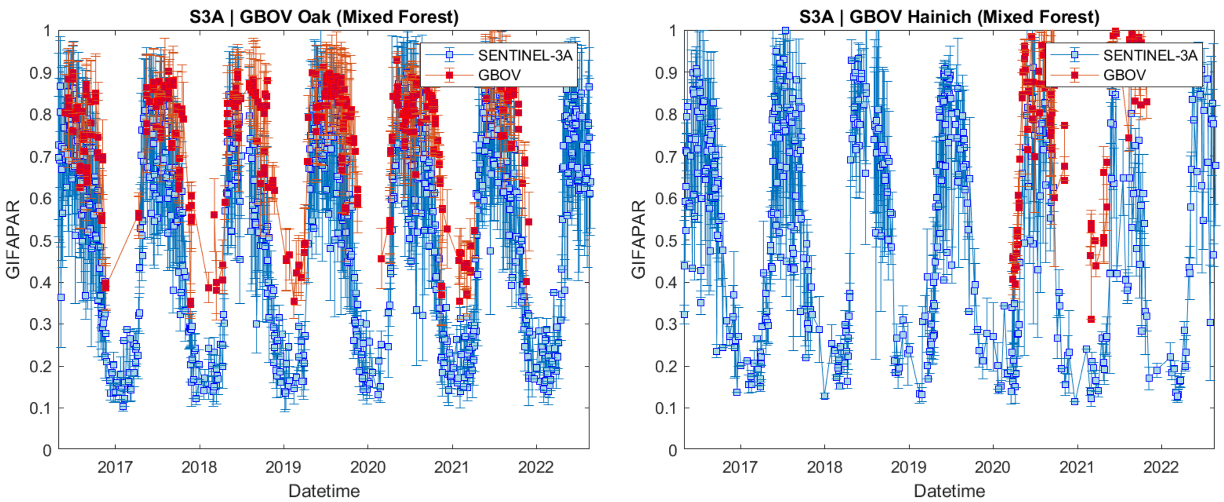

Figure 94: same as Figure 92 for sites Oak (Left) and Hainich (right)

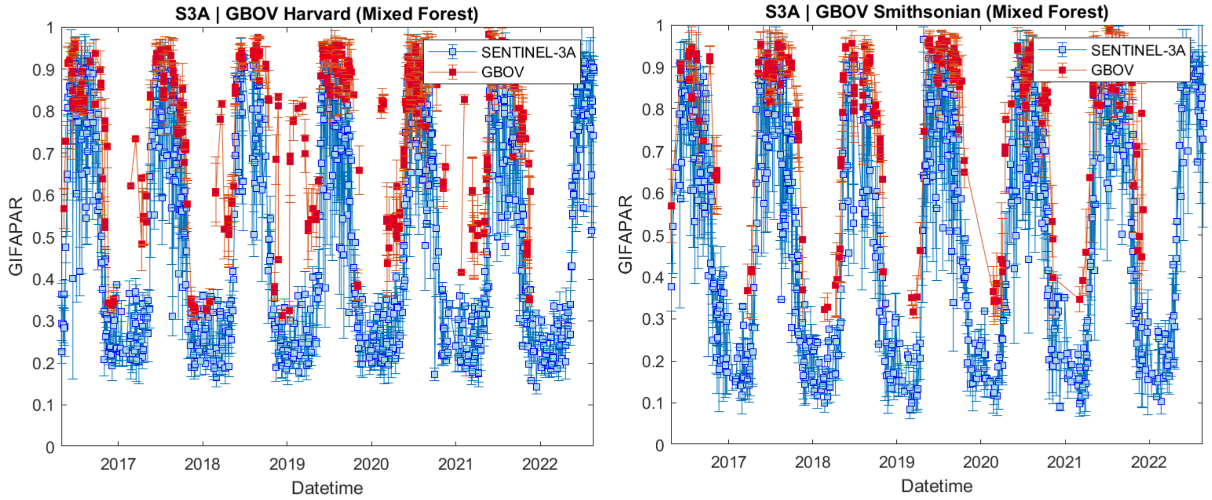

Figure 95: same as Figure 92 for sites Harvard (Left) and Smithsonian (right)

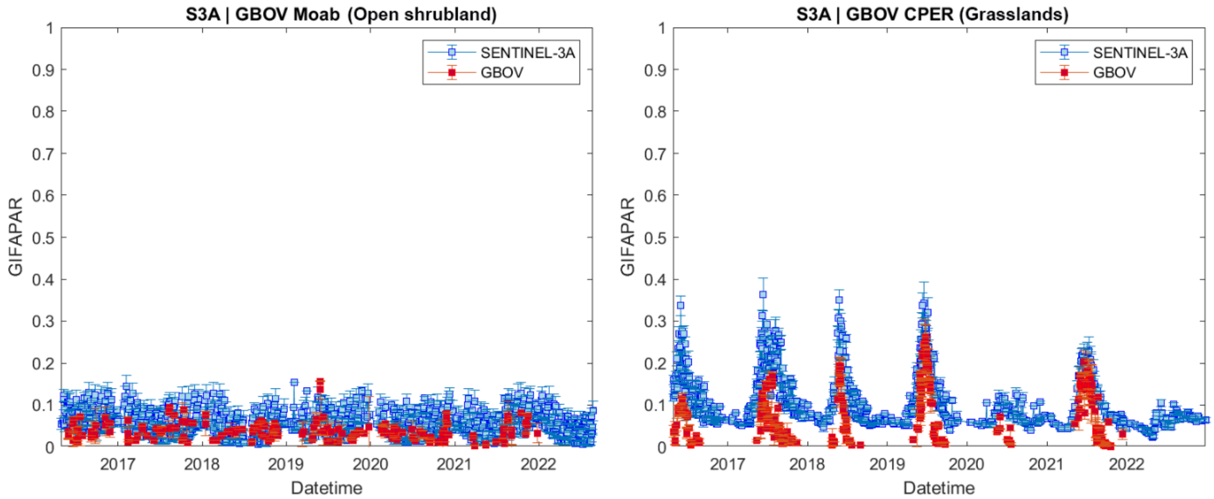

Figure 96: same as Figure 92 for sites Moab (Left) and CPER (right)

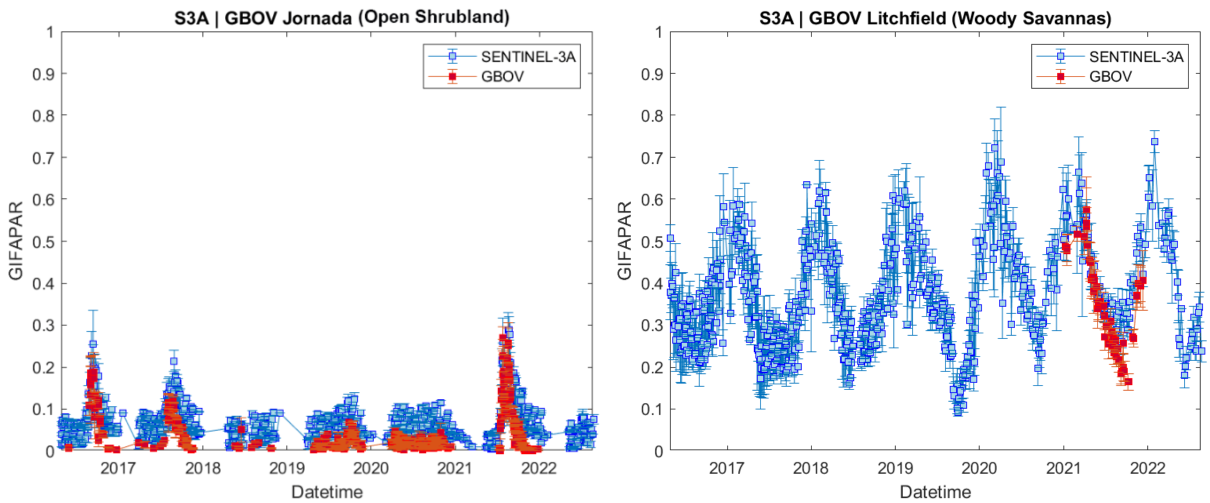

Figure 97: same as Figure 92 for sites Jornada (Left) and Litchfield (right)

4.1.2.1 OLCI-B

Figure 98 to Figure 103 show the temporal profiles of GBOV LP4 against OLCI-B GIFAPAR. Overall, there are similar seasonal trajectories between OLCI-B and GBOV. The pattern is similar to OLCI-A, with higher values of GBOV than in OLCI-B for forest classes. Similarly, grassland and shrubland classes show lower values than OLCI-B. Furthermore, the number of GBOV values after filtering needs to be increased to perform the validation, mainly in grasslands and shrublands sites (i.e., Moab, Central Plains).

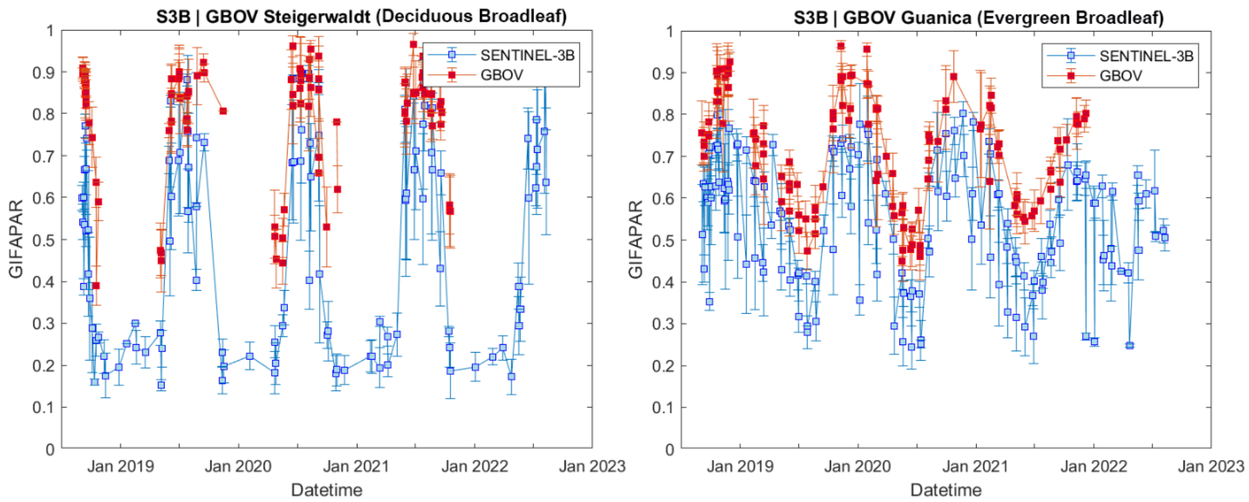

Figure 98: Time series of GBOV FIPAR LP4 (red) and OLCI-B GIFPAR (blue) for sites Steigerwaldt (left) and Guanica (right).

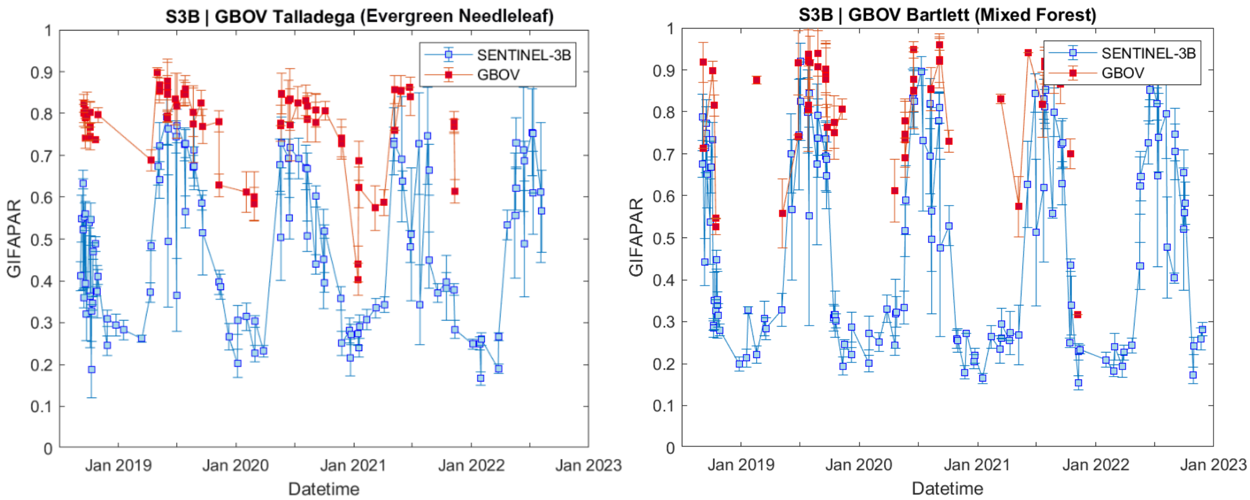

Figure 99: same as Figure 98 for sites Talladega (Left) and Bartlett (right)

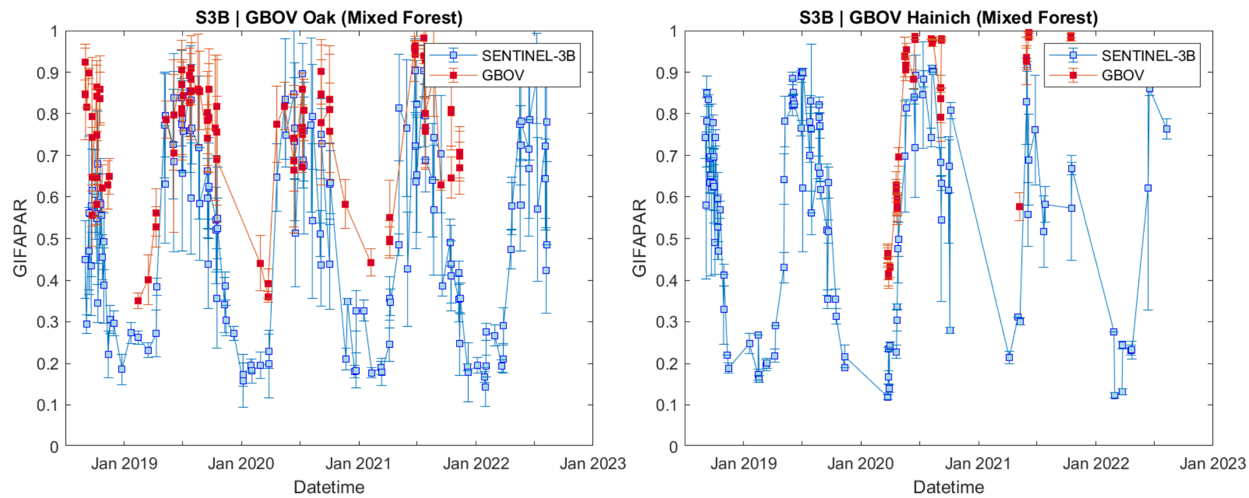

Figure 100: same as Figure 98 for sites Oak (Left) and Hainich (right)

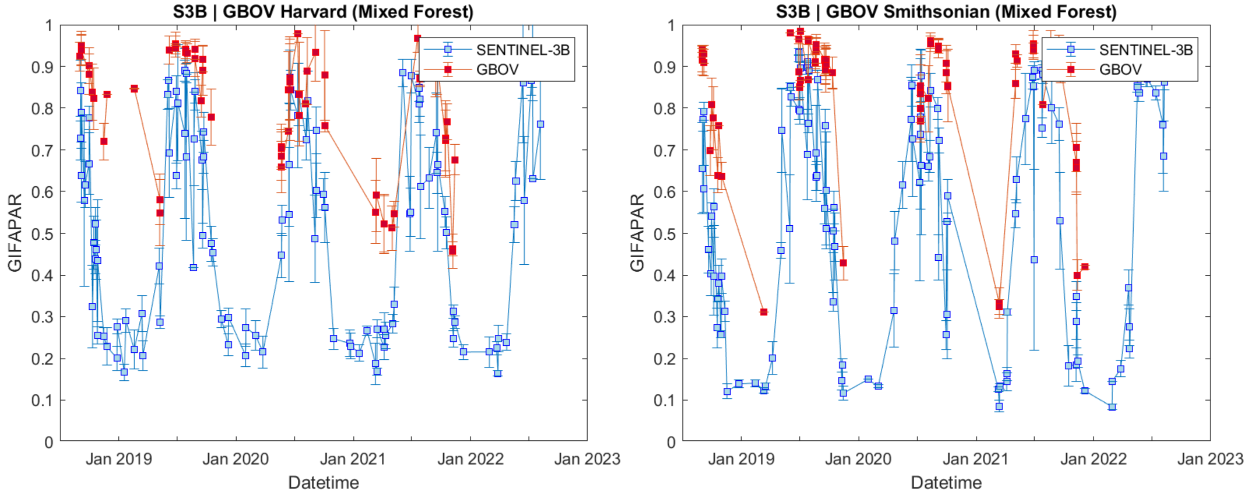

Figure 101: same as Figure 98 for sites Harvard (Left) and Smithsonian (right)

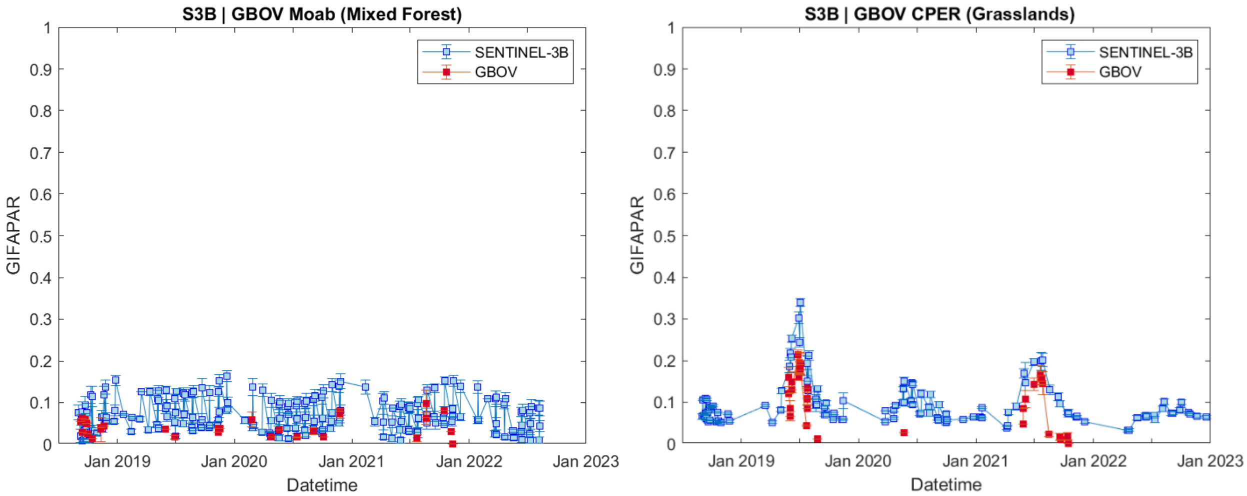

Figure 102: same as Figure 98 for sites Moab (Left) and CPER (right).

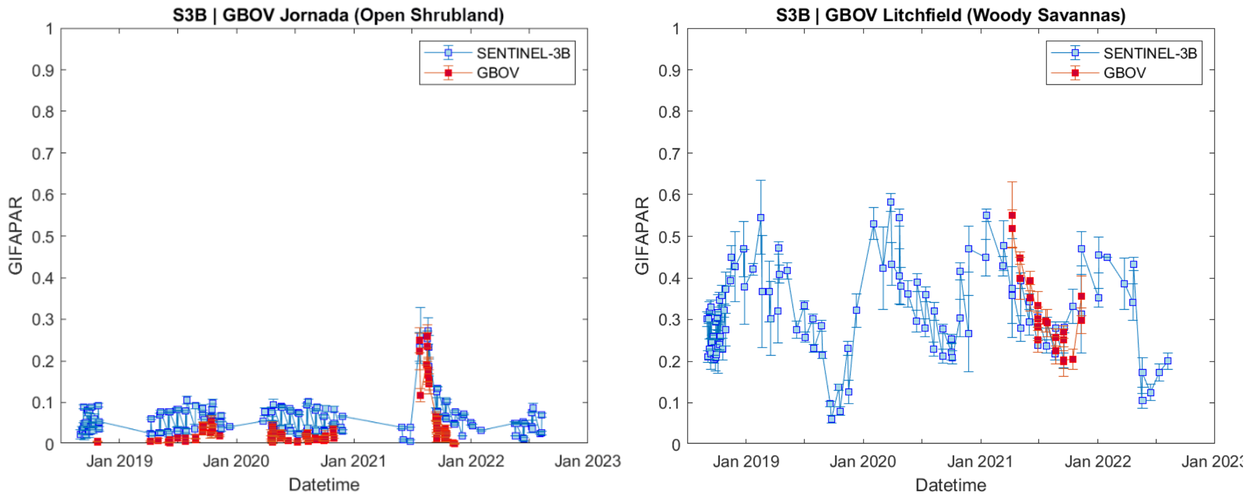

Figure 103: same as Figure 98 for sites Jornada (Left) and Litchfield (right).

4.2 [OLCI-L2LRF-CV-410 & OLCI-L2LRF-CV-420] – Cloud Masking & Surface Classification for Land Products

4.2.1 Sky Camera based validation – prototype results for December 2022

According to the methodology presented in DQR of July 2022, the cloud masking validation results based on Sky Cameras is presented for December observations hereafter.

Figure 108 and Figure 109show the prototype validation results for December 2022. The weather in December around Rome got again a bit more humid with most days being clouded (see Figure 104). The average rainfall for December is between 3 to 8 days, with 5 days between 1st and 31st of December 2022 (see Figure 105).

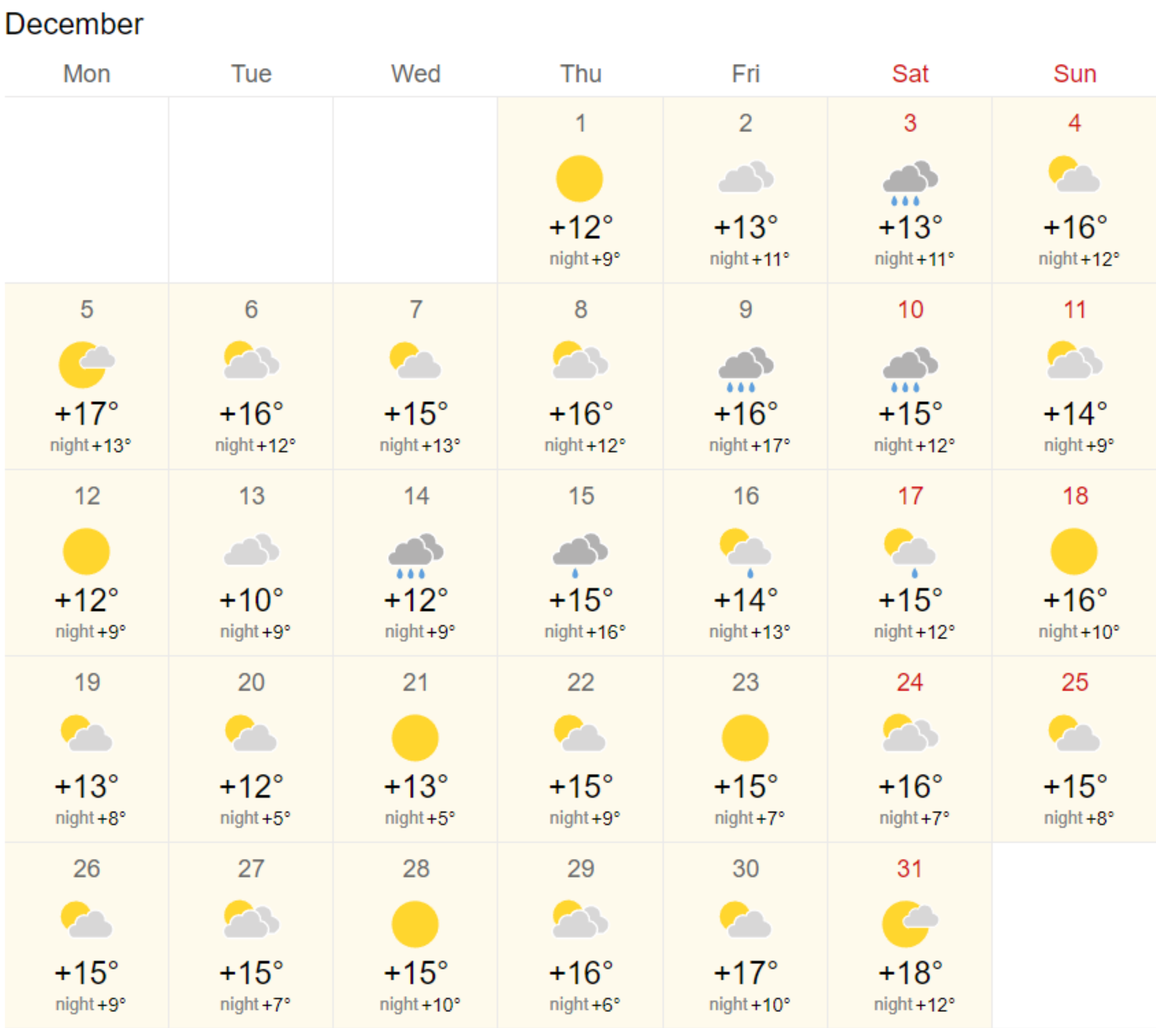

Figure 104: Temperature and cloud cover Rome, December 2022 (source: https://world-weather.info/forecast/italy/rome/december-2022/)

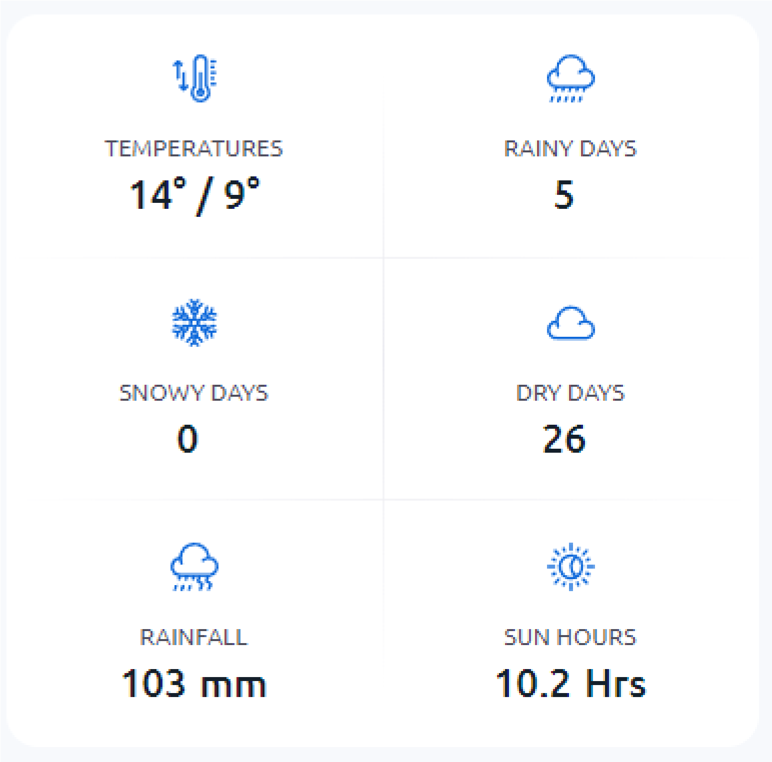

Figure 105: Average temperature, rainy days, and rainfall over Rome, December 2022 (source: https://www.weather25.com/europe/italy/lazio/rome?page=month&month=December)

More than half of the SC observation show a good amount of cloud cover (see Figure 106). Some SC classifications, like on 17th December or 27th December show a bit of underestimation of cloud coverage from the SC classification. Making the December reference a bit clear sky biased.

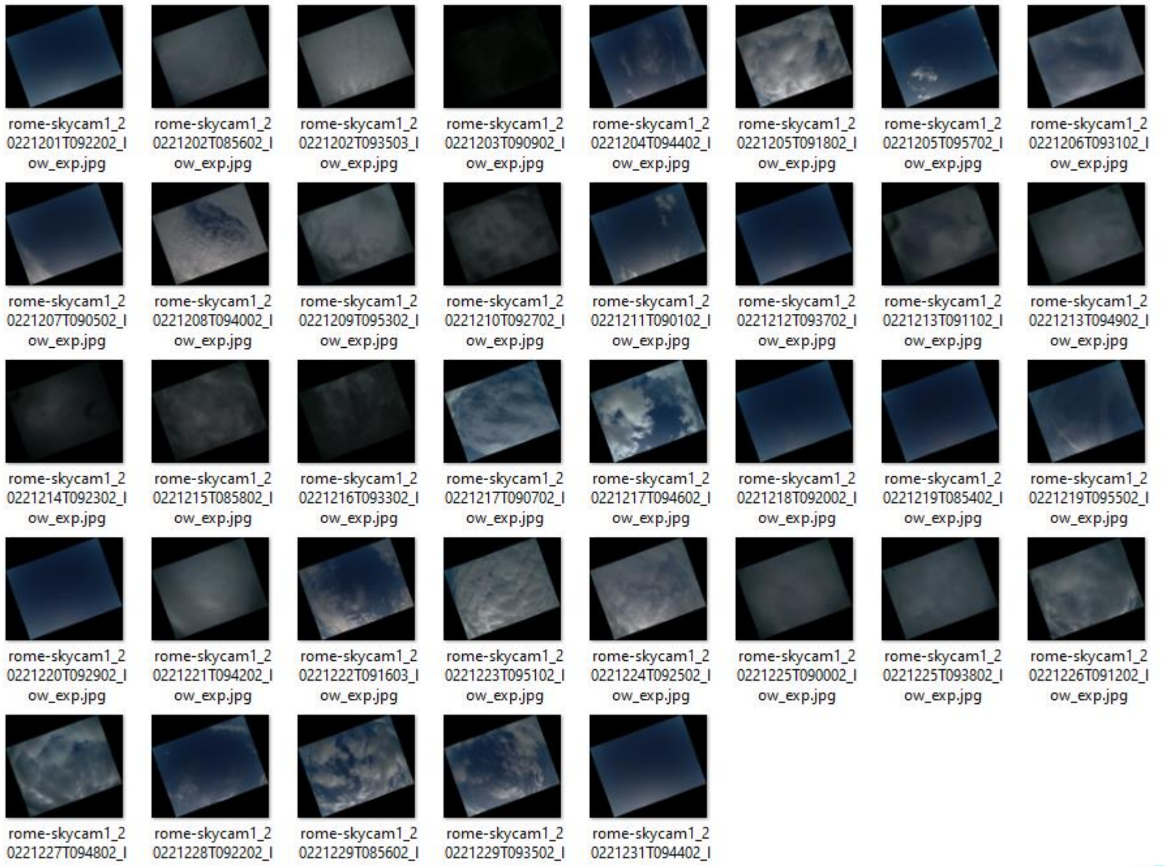

Figure 106: Sky camera acquisitions over Rome during Sentinel-3 OLCI overpass

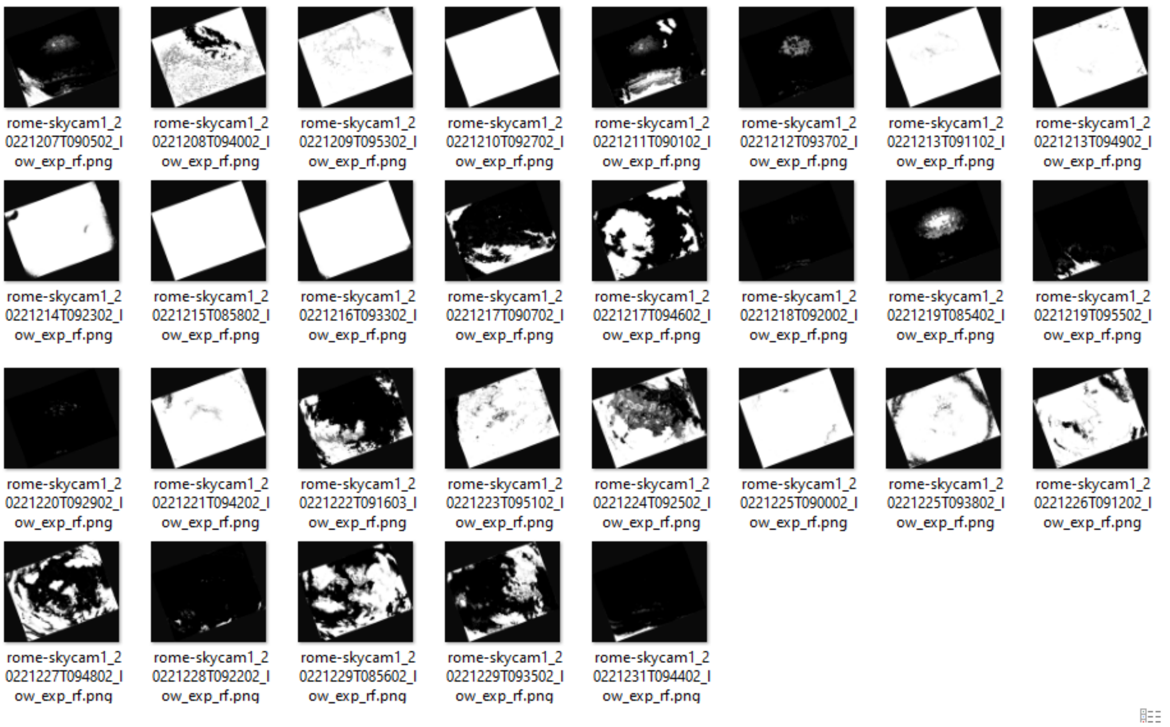

Figure 107: Classified sky camera acquisitions over Rome during Sentinel-3 OLCI overpass

The distribution between clear and cloud observations is quite even during December. But as described above, the SC classification seems to have a small clear bias.

Figure 108 shows the validation results for the OLCI cloud flags including the margin. The clear bias of the reference data causes a drop in producer accuracy for cloud and thus a decrease in the overall accuracy. This decrease can be neglected, since the cause of the decrease is known.

When neglecting the margin (see Figure 109) the performance is a bit better.

In December multiple acquisitions at the same day were made by OLCI A and OLCI B. Therefore, we expect some low acquisition angles that can also cause issues from the parallax effect. We will investigate this in the next reporting period and try to limit OLCI acquisitions to those closest to nadir.

SC 1 autom. classif. vs. OLCI L2 LFR Cloud & Ambiguous & Margin - Dec 2022

Sky Camera 1

OLCI L2 LFR

Class	Clear	Cloud	Sum	U A	E
CLEAR	10	1	11	90.9	9.1
CLOUD	8	16	24	66.7	33.3
Sum	18	17	35		
P A	55.6	94.1		OA:	74.29
E	44.4	5.9		BOA:	74.85

Scotts Pi: 0.47
Krippendorfs alpha: 0.477
Cohens kappa: 0.491

Figure 108: Confusion matrix showing validation results for OLCI L2 cloud screening including margin against SC1 automated classification

SC 1 autom. classif. vs. OLCI L2 LFR Cloud & Ambiguous - Dec 2022

Sky Camera 1

OLCI L2 LFR

Class	Clear	Cloud	Sum	U A	E
CLEAR	11	1	12	91.7	8.3
CLOUD	7	16	23	69.6	30.4
Sum	18	17	35		
P A	61.1	94.1		OA:	77.14
E	38.9	5.9		BOA:	77.6

Scotts Pi: 0.533
Krippendorfs alpha: 0.54
Cohens kappa: 0.546

Figure 109: Confusion matrix showing validation results for OLCI L2 cloud screening excluding margin against SC1 automated classification

5 Validation of Integrated Water Vapour over Land & Water

For the current reporting period we investigated the temporal evolution of quality measures of integrated water vapour, when comparing SUOMI NET (Ware et al. 2000) with reduced resolution data of OLCI L2 non-time-critical. In the last reporting period the data acquisition changed from EUMETSAT CODA to EUMETSATS datastore (collection id: EO:EUM:DAT:0410). All data from Apr 2022 on belongs to that source. The datastore has proven to be reliable, no missing orbits or segments have been detected.

693000 (OLCI-A) and 381000 (OLCI-B) potential matchups within the period of June 2016 (OLCI-A) January 2019 (OLCI-B) to begin of January 2023 have been analysed yet. The global service of SUOMI-NET has been reduced at the end of 2018, thus OLCI-B colocations are less frequent outside North America.

For the cloud detection, the standard L2 cloud-mask has been applied (including the cloud ambiguous and cloud margin flags). The comparison of OLCI and GNSS shows a very high agreement (Figure 110). The correlation between both quantities is 0.97-0.98. The root-mean-squared-difference is 1.9 -2.1 kg/m^2. The systematic overestimation by OLCI is 11%-12%. The bias corrected *rmsd* is around 1.3 kg/m^2.

The temporal evolution of several quality measures (Figure 111), indicates small seasonal variations, which are certainly related to retrieval assumptions. Apart from these features, neither systematic temporal changes nor differences between OLCI A and B have been observed. In April 2022, one can see a small anomaly in OLCI B. It arose from the incorrect choice of relative satellite orbits by CODA during this period. In the end, only few coincidentally valid matchups were possible at very high latitudes where RR files overlap. This resulted in a sampling bias towards very dry conditions, which in turn led to a smaller systematic deviation but also a lower *explained variance* r^2.

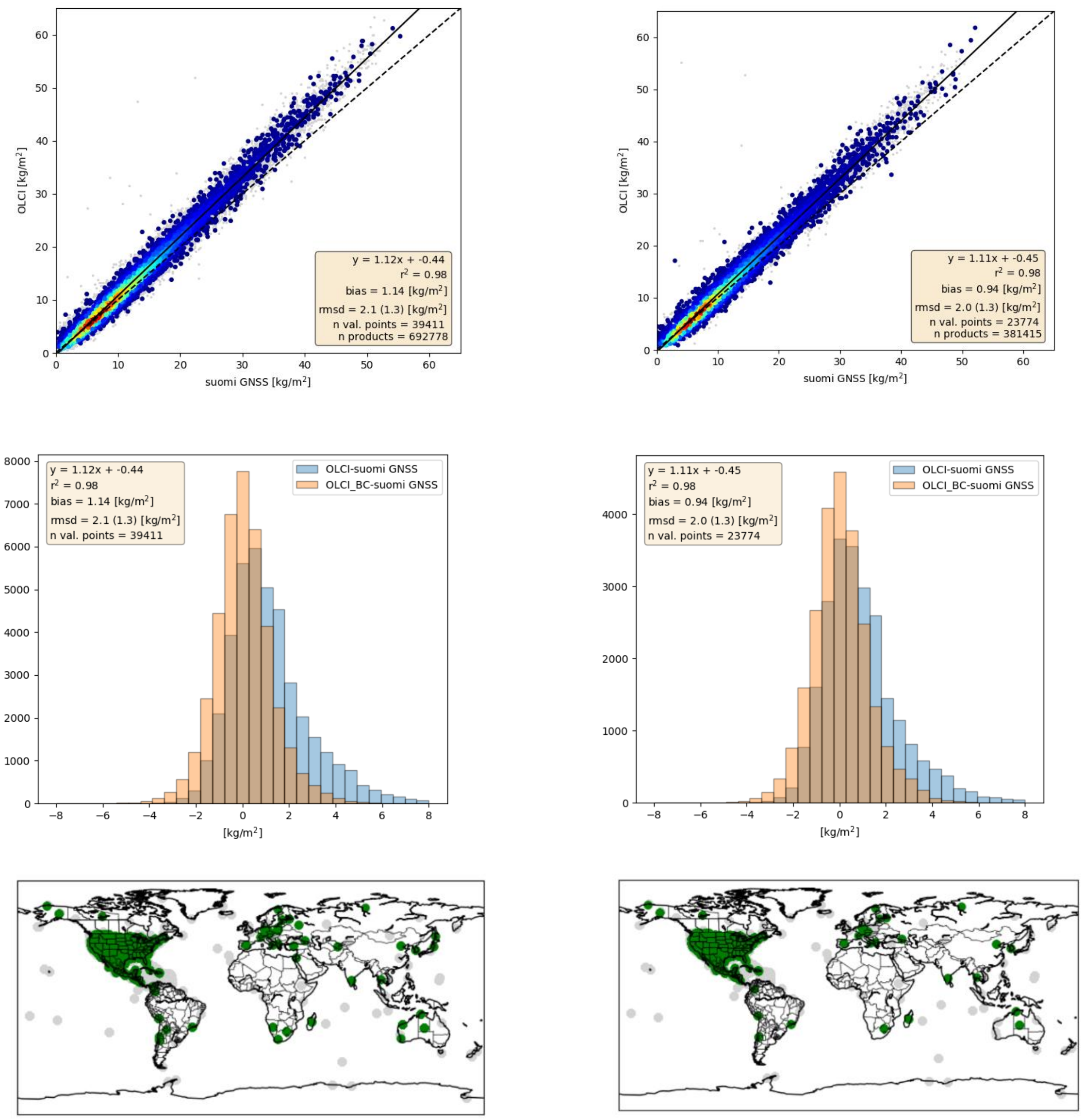

Figure 110: Upper: Scatter plot of the IWV products, derived from OLCI (A left, B right) above land and from SUOMI NET GNSS measurements. Middle: Histogram of the difference between OLCI (A: left, B: right) and GNSS (blue: original OLCI, orange: bias corrected OLCI). Lower: Positions of the GNSS (A: left, B: right).

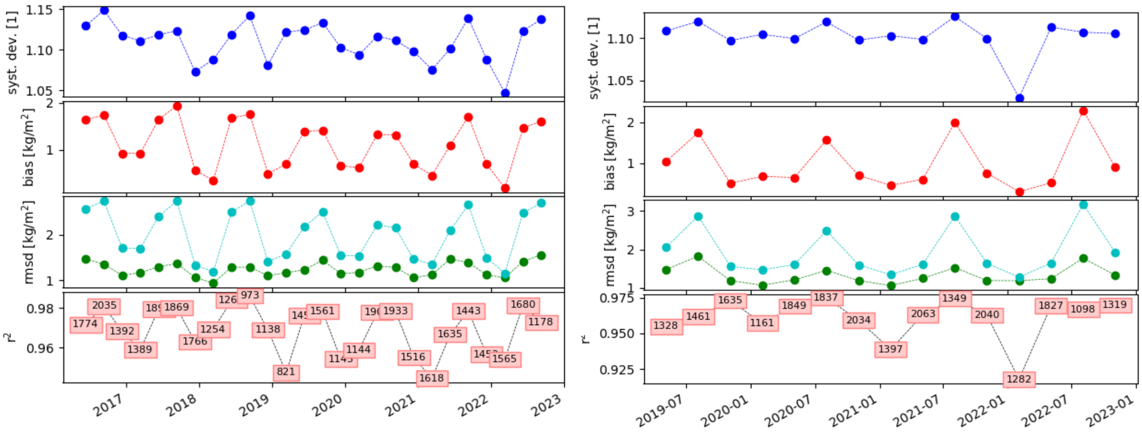

Figure 111: Temporal evolution of different quality measures for OLCI A (left) and OLCI B (right) with respect to SUOMI Net. From top to bottom: systematic deviation factor, bias, root mean squared difference (with and without bias correction), explained variance (number in boxes are the numbers of matchups)

6 Level 2 SYN products validation

6.1 SYN L2 SDR products

There has been no new result during the reporting period. Most recent performance figures can be found in the S3MPC OPT Annual Performance Report - Year 2021 (S3MPC.ACR.APR.009, issue 1.0, 08/12/2021), available on-line at:

https://sentinels.copernicus.eu/web/sentinel/user-guides/sentinel-3-olci/document-library.

6.2 SY_2_VGP, SY_2_VG1 and SY_2_V10 products

The similarity of SYN VGT like products with the PROBA-V archive is evaluated through intercomparison of 10-daily composites extractions over LANDVAL [1] sites. Since there is no overlap with the PROBA-V nominal operational phase and no PROBA-V Collection 2 climatology is available yet, direct comparison is done by comparing the SY_2_V10 NTC products starting January/2021 with those of PROBA-V S10-TOC since January/2018.

The temporal evolution of statistics results below is based on intercomparison over the entire periods up to December/2022. The scatterplots are based on intercomparison between SY_2_V10 products of December/2022 with PROBA-V Collection 2 S10-TOC products of December/2019.

Products availability

Availability of SY_2_VG1 and SY_2_V10 products is checked through an automated query and download via the Copernicus Collaborative Node and the Copernicus Open Access Hub feeding the products database Belgian Collaborative Ground Segment (Terrascope, www.terrascope.be). For the month December/2022, there are no data quality issues with a deviating amount of missing data or empty tiles.

Statistical consistency

The scatter density plots with geometric mean regression equation, coefficient of determination (R^2) and APU statistics based on intercomparison between SY_2_V10 products of December/2022 with PROBA-V Collection 2 products of December/2019 are shown in Figure 112. The APU statistics are defined as: Accuracy (A) or average bias, Precision (P) or the standard deviation of the bias, and Uncertainty (U) or the Root Mean Squared Distance. Accuracy is best for BLUE (< 1%), less good for RED and NIR (~2%) and worse for SWIR (~-8%). The relatively large values for Precision (large scatter, low R^2) are caused by the fact that products of two different years are compared. The disagreement for the SWIR band is related to the SLSTR calibration offset (in bands S5 and S6).

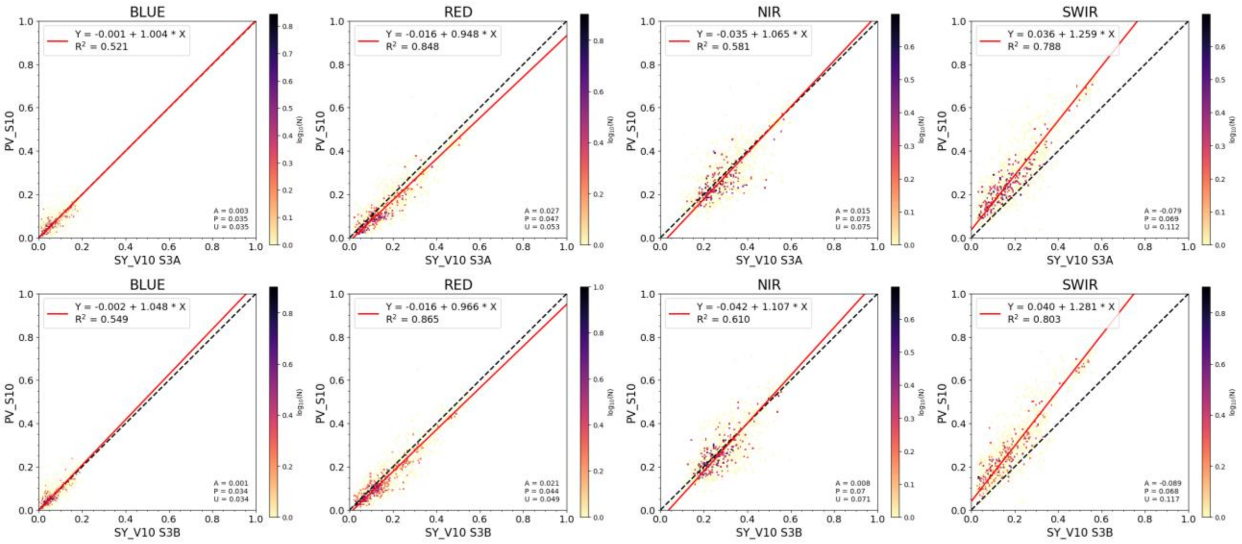

Figure 112: Scatter density plots between SY_V10 S3A (top) or S3B (bottom) and PROBA-V C2 S10-TOC for BLUE, RED, NIR and SWIR bands (left to right), December/2022 vs. December/2019

Temporal consistency

The temporal evolution of APU statistics derived from intercomparison of SY_2_V10 NTC products January/2021 – December/2022 with those of PROBA-V S10-TOC January/2018 – December/2019 (Figure 113). The APU statistics show stable evolution over time, although some seasonal pattern is observed for the mainly the SWIR channel, and to a lesser extent the RED and NIR channel. The temporal behaviour is stable.

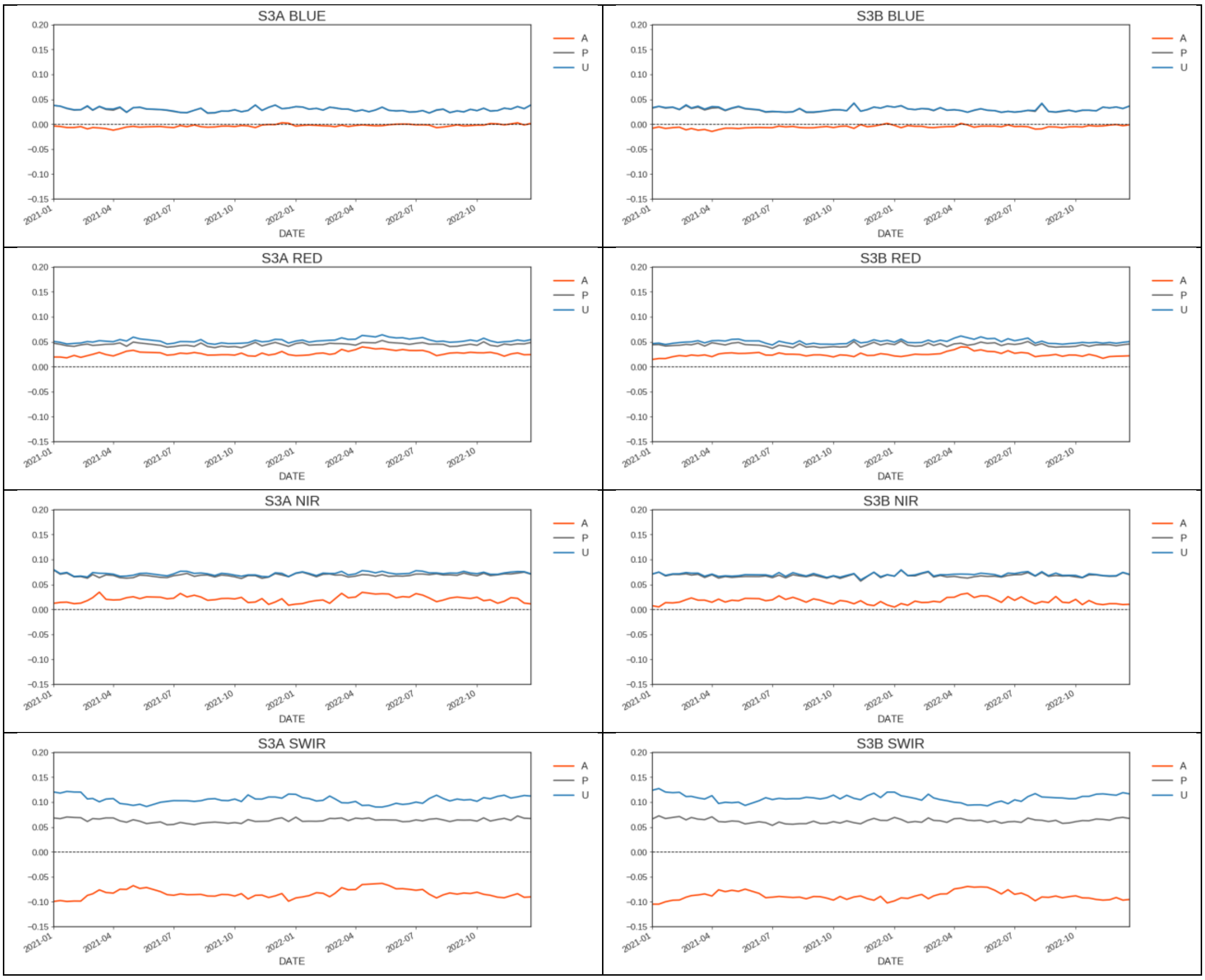

Figure 113: Temporal evolution of APU statistics between SY_2_V10 S3A (left) or S3B (right) and PROBA-V S10-TOC for BLUE, RED, NIR and SWIR bands (top to bottom), January/2021 - December/2022 vs. January/2018 - December/2019

References

[1] B. Fuster *et al.*, “Quality Assessment of PROBA-V LAI, fAPAR and fCOVER Collection 300 m Products of Copernicus Global Land Service,” *Remote Sens.*, vol. 12, no. 6, p. 1017, Mar. 2020, doi: 10.3390/rs12061017.

6.3 SYN L2 AOD NTC products

In month 12, the following activity has been performed:

- S3A validation period was extended by two months (incl. September 2022). Matchups for October have gups and will be re-calculated by ACRI
- S3B validation period in LAW project (2020-2021) has been extended by nine months (incl. September 2022)
- S3A and S3B validation results were inter-compared

For the period 14.01.2020-30.09.2022, scatter density plots for S3A and S3B AOD_{550} matchups between AERONET and Sy_2 for different groups of products: all matchups, pixels retrieved with dual, single applied to nadir (singleN) and single applied to oblique (singleO) approaches are shown globally (Figure 114) and separately for the NH (Figure 115) and the SH (Figure 116).

Two months extension of the validation period have not changed much validation statistics for S3A. As revealed early,

- Positive bias is observed for low AOD for all groups of matchups
- High (>0.75) AOD is strongly underestimated for pixels retrieved with dual approach
- AOD in all ranges is (strongly) overestimated for pixels retrieved with single approach applied to the nadir view (singleN)

As in the LAW project, validation statistics for S3B Sy_2 AOD product are slightly better for dual and singleN (thus, for group “all”) approaches. For singleO, fraction of matchups in MODIS error envelope (EE) and fraction of matchups which satisfy GCOS requirements are slightly higher for S3A.

Similar conclusions can be attributed to the NH validation results, where most of AERONET stations are located. In the SH, the number of SY_2 AOD outliers (as well as the total number of matchups) is considerably lower, which results in better validation statistics.

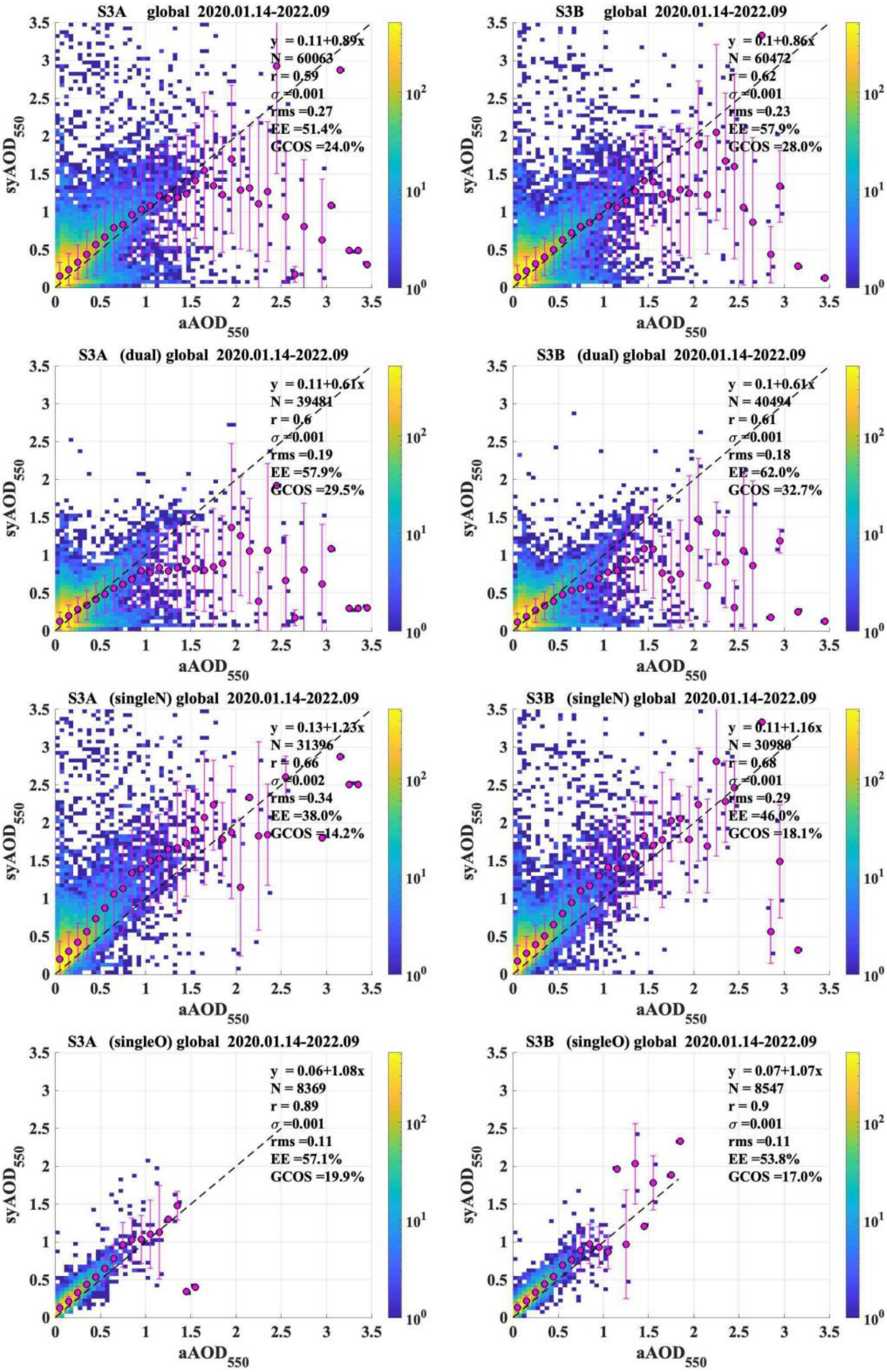

Figure 114: Globally, for S3A (left) and S3B (right), scatter density plots for AOD_{550} matchups between Sy_2 and AERONET for different groups of products: all matchups, pixels retrieved with dual, single applied to nadir (singleN) and single applied to oblique (singleO) approaches (top down). For the period 14.01.2020-30.09.2022.

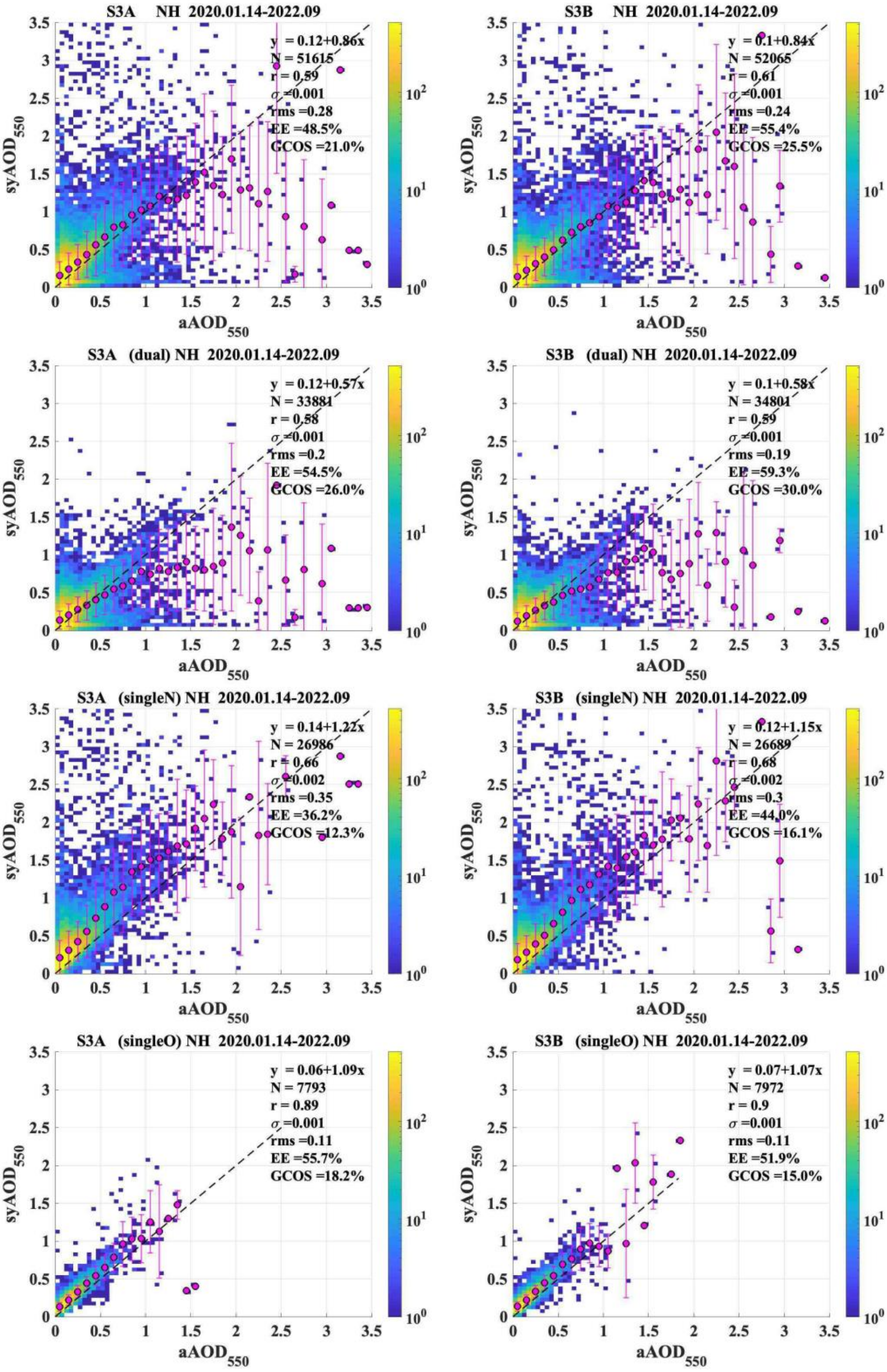

Figure 115: As Figure 114 , for the NH

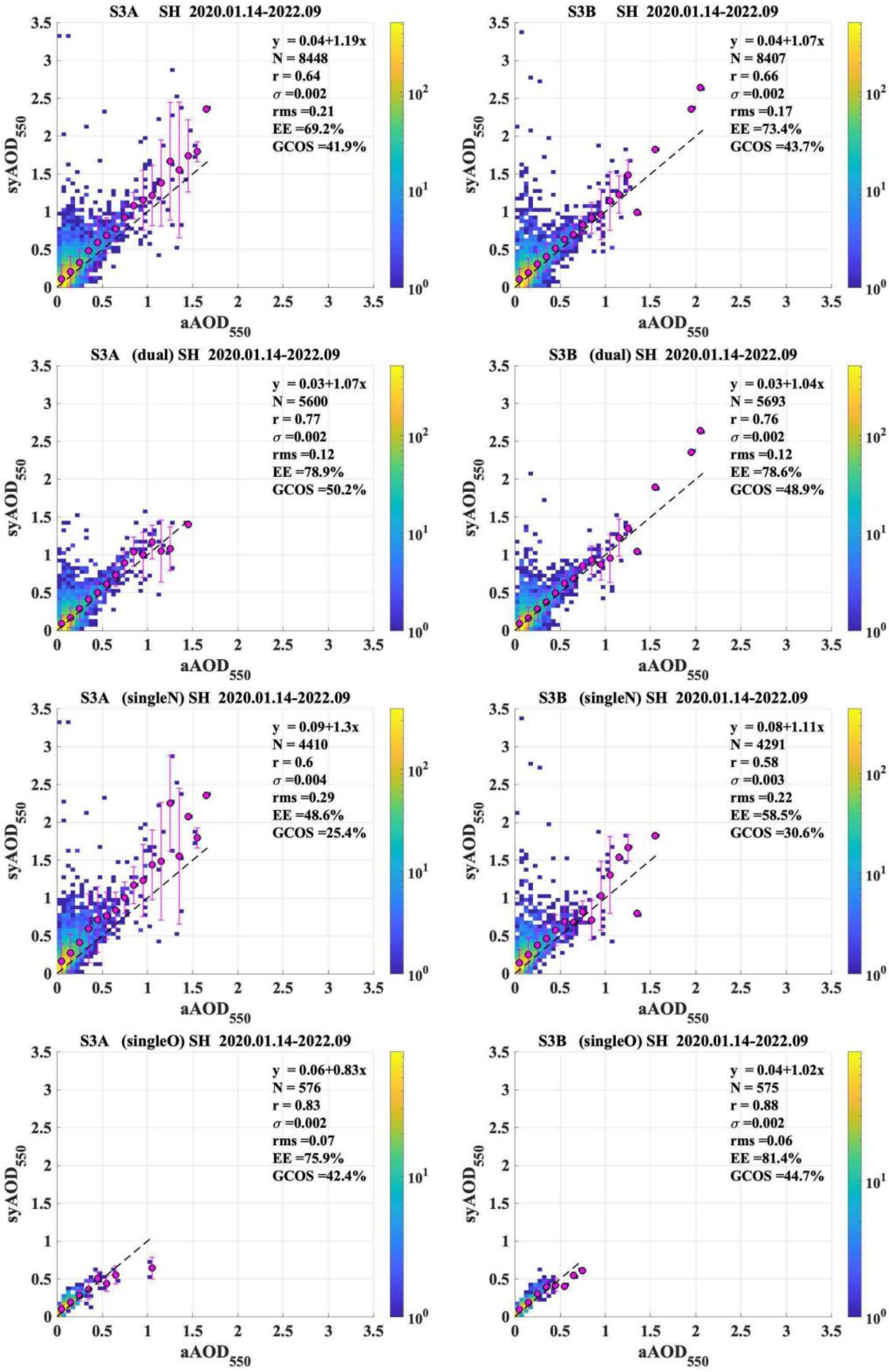

Figure 116: As Figure 114, for the SH.

Binned (by 0.1, based on AERONET AOD) Sy_2 AOD offsets (magenta dots in Figure 114 - Figure 116) for different groups of matchups were collected in one plot (Figure 117) for S3A (left panel) and S3B (right panel). The binned offsets for all matchups show positive bias of about 0.1 (for AOD<1). For AOD<0.3, this bias is a result of positive offset contribution from both singleN and dual groups of matchups. For AOD>0.4, offsets for dual group turns to negative and increases steadily.

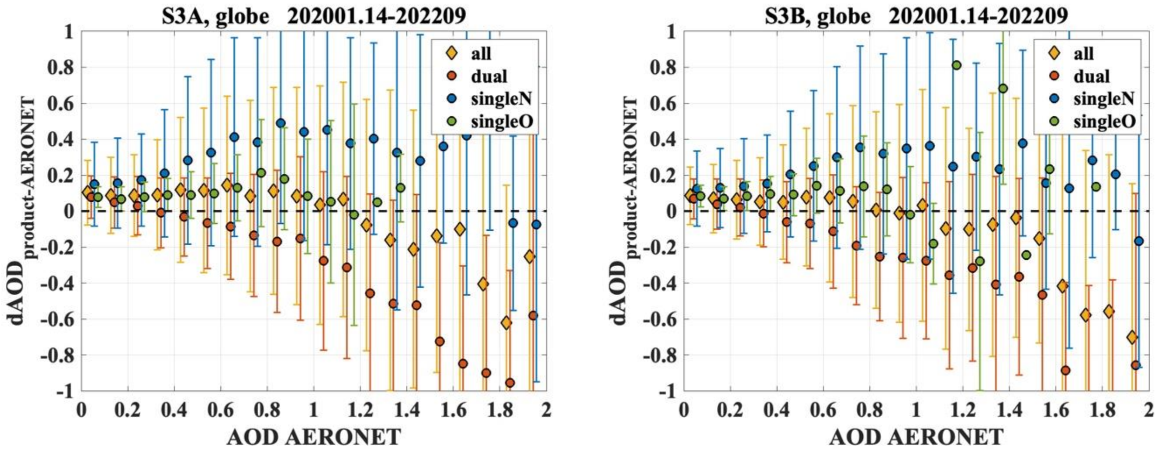

Figure 117: For S3A (left) and S3B (right), binned (based on AERONET AOD) Sy_2 AOD offsets (magenta dots in Figure 114 - Figure 116) for different groups of matchups: all, dual, singleN and singleO.

To better see the difference between S3A and S3B offsets to AERONET, we show S3A and S3B offsets on one plot (Figure 118); offsets for different groups are shown separately (panels top down). S3B offsets are lower for all four groups in almost all AOD ranges, which supports better overall validation statistics for S3B.

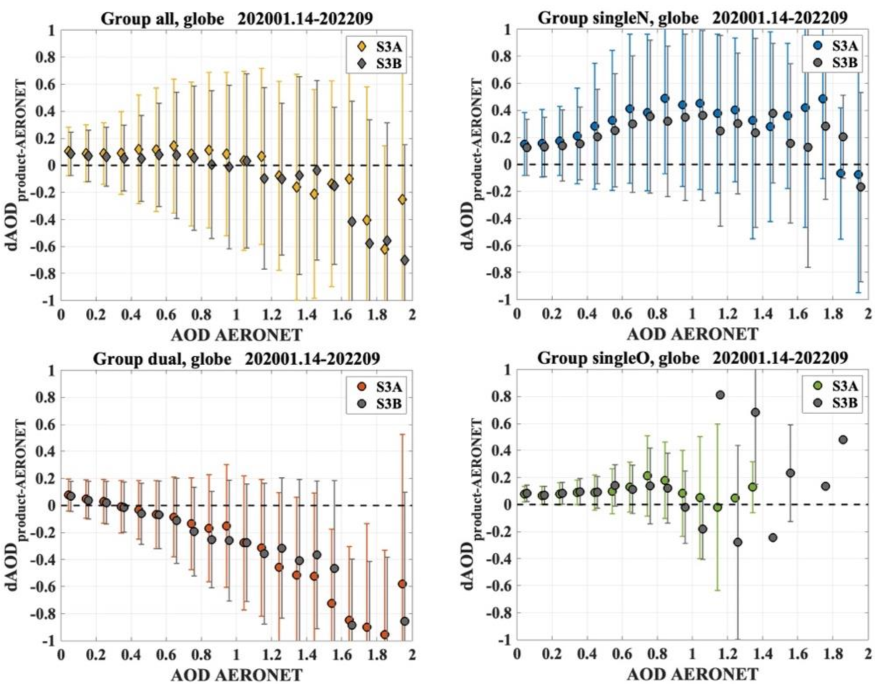

Figure 118: For different groups of matchups – all, dual, singleN, singleO (top to bottom, then left to right) – binned offset of S3A and S3B Sy_2 AOD to AERONET. Colors for S3A are as in Figure 117; S3B results are shown in grey.

An extended analysis of the offsets will be performed when matchups are available for the whole 2022.

7 Events

For OLCI-A, two Radiometric Calibration sequences have been acquired during the reported period:

- S01 sequence (diffuser 1) on 11/12/2022 02:57 to 02:59 (absolute orbit 35496)
- S01 sequence (diffuser 1) on 26/12/2022 08:12 to 08:14 (absolute orbit 35713)

For OLCI-B, two Radiometric Calibration sequences have been acquired during the reported period:

- S01 sequence (diffuser 1) on 12/12/2022 13:39 to 13:41 (absolute orbit 24123)
- S01 sequence (diffuser 1) on 27/12/2022 10:28 to 10:30 (absolute orbit 24335)

8 Appendix A

Other reports related to the Optical mission are:

- S2 L1C MSI Data Quality Report, November 2022 (ref. OMPC.CS.DQR.01.12-2022 – i82r0)
- S2 L2A MSI Data Quality Report, November 2022 (ref. OMPC.CS.DQR.02.12-2022 – i55r0)
- S3 SLSTR Data Quality Report, November 2022, (ref. OMPC.RAL.DQR.04.12-2022)

All Data Quality Reports, as well as past years Data Quality Reports and Annual Performance Reports, are available on dedicated pages in Sentinel Online website, at:

- https://sentinel.esa.int/web/sentinel/technical-guides/sentinel-3-olci/data-quality-reports
- https://sentinels.copernicus.eu/web/sentinel/technical-guides/sentinel-3-slstr/data-quality-reports
- OPT Annual Performance Report Year 2021 (PDF document)

End of document